EXPERIMENTAL MEASUREMENT OF MULTIPHASE FLOW AND CFD EROSION MODELING IN ELECTRICAL SUBMERSIBLE PUMPS

A Dissertation

by

SAHAND PIROUZPANAH

Submitted to the Office of Graduate and Professional Studies of
Texas A&M University
in partial fulfillment of the requirements for the degree of

DOCTOR OF PHILOSOPHY

Chair of Committee,	Gerald L. Morrison
Committee Members,	Debjyoti Banerjee
	Devesh Ranjan
	Yassin A. Hassan
Head of Department,	Andreas A. Polycarpou

December 2014

Major Subject: Mechanical Engineering

ABSTRACT

Electrical Submersible Pumps (ESPs) are widely being used in upstream oil production. To better understand the ESP pump's behavior, two different ESPs, MVP-G470 and ESP-WJE1000, manufactured by Baker Hughes company have been studied experimentally and numerically to determine the pump and flow behavior in different operating conditions and for different working fluids.

The MVP-G470 is a multi-vane electrical submersible pump which has been designed to increase the gas handling capacity of typical multiphase ESPs up to 70% gas volume fraction. Homogenized flow and finer bubbles produced by MVP pumps help the ESPs to delay the surging and gas lock condition to higher gas volume fractions and operate effectively. In this work, an experimental study on the performance of a 3-stage MVP along with detail study on the performance of two stages of the pump are performed.

Overall pump performance for different operating conditions such as different inlet pressure, inlet gas volume fraction, water flow rate and speeds are performed for a mixture of water and air. Detail study of a stage performance is done on the first and second stage of the pump using conductivity and pressure measurements accompanied by high speed visualization. The data obtained from these measurements is employed to relate stage head degradation to effective parameters on the pump performance.

The ESP-WJE1000 is a typical mixed flow ESP pump with a single vane rather than split-vane design used in MVPs. Numerical study on the erosion phenomena in this pump has been performed. The influence of key parameters on erosion in ESPs has been identified and a new model to predict the erosion rate at different pump locations has been introduced.

DEDICATION

To my loving mother and father, kind siblings and my lovely wife

ACKNOWLEDGMENTS

I would like to express my special appreciation and thanks to my committee chair and advisor, Dr. Gerald Morrison for all his help, support, understanding and guidance throughout my study. You have been a tremendous mentor for me. I would like to thank you for encouraging my research and for allowing me to grow as a research engineer. Your advice on both research as well as on my career have been priceless.

I would also like to thank my committee members, Dr. Banerjee, Dr. Ranjan, and Dr. Hassan, for their guidance and support throughout the course of this research.
Thanks also to my friends and colleagues and staff in the Turbmachinery lab for being there to support when I needed.

Thanks to Sujan Reddy, Emanuel Marsis, Klayton Kirkland, Abhay Patil, Scott Chien, Joey Marchetti and Daniel Zheng for their helps and support during the past four years.

Thanks to Shell Oil Company for funding this project, and providing me with all the knowledge and information I needed throughout my research.

Finally, thanks to my kind mother, father, brother and sister for their encouragement, without their support I could not accomplish this. Words cannot express how grateful I am to my mother and father for all of the sacrifices that you've made on my behalf.

NOMENCLATURE

ESP	Electrical Submersible Pump
MVP	Multi Vane Pump
VFD	Variable Frequency Drive
λ	Clearance ratio
GVF	Gas Volume Fraction
PWR	Pressurized Water Reactors
ψ	Head coefficient
a_i	Two phase property formation at location i
ϕ_{tpi}	Two-phase flow coefficient
BEP	Best Efficiency Point
s	Slip velocity ratio at location i
ΔH_{otpth}	Total head, theoretical value for two-phase conditions
ΔH_{otp}	Total head, actual two-phase conditions
ΔH_{ospth}	Total head, theoretical value for one-phase conditions
ΔH_{osp}	Total head, actual one-phase conditions
ϵ	Q_{bep}/Q_{tp}
k	Pump-dependent constant
C_D	Drag Coefficient
r_b	Bubble radius
J	Current density
σ	Electrical conductivity
φ	Electrical potential
k_g	Geometry factor
κ	Fluid electrical conductivity
ε_r	Relative permittivity
ε_0	Vacuum permittivity

C	Area fraction of the dispersed phase (gas) in each pixel
σ_{L}	Conductivity of the continuous phase (liquid)
σ_{mc}	Measured conductivity
$\mathrm{A_G}$	Area occupied by gas in electrode location
$\mathrm{A_L}$	Area occupied by liquid in electrode location
U_P	Mean velocity of the fluid at the near wall node P
k_P	Turbulence kinetic energy at the near wall node P
y_P	Distance from point P to the wall
Q_L	Liquid volumetric flow rate
Q_G	Gas volumetric flow rate
p_{out}	Pump outlet Pressure
p_{in}	Pump inlet pressure
$P_{h,2ph}$	Two phase hydraulic power
P_{in}	Input power to the pump
N	Rotating Speed
D	Pump Diameter
f_D	Drag force per unit volume
V_L	Velocity of liquid phase
V_G	Velocity of gas phase
α	Volumetric void fraction
λ_{g_s}	No-slip gas volume fraction at the stage inlet
ρ_{g_s}	Gas density at the stage inlet
ρ_{g_c}	Gas density at the impeller outlet
$Q_{bep,s}$	Liquid volumetric flow rate at the best efficiency point
ρ_p	Density of rigid particles
ρ_f	Density of the fluid
υ_f	Kinematic viscosity of fluid
ω	Oscillation frequency

k	Turbulent kinetic energy, m^2/s^2
$\overline{k_{w_0}}$	Reference turbulent kinetic energy, $1 m^2/s^2$
α_s	Sand volume fraction, -
V_s	Near wall sand velocity, m/s
$\overline{V_{s_0}}$	Reference sand velocity, $1\ m/s$
EF	Erosion factor, -
ER	Erosion rate, $\mu m/hr$

TABLE OF CONTENTS

Page

LIST OF FIGURES

Page

Page

Page

Page

Page

Page

Page

LIST OF TABLES

Page

1. INTRODUCTION

Artificial lift is used to allow low pressure, non-producing wells to become productive. There are three major ways to create artificial lift in oil wells which are gas lift, jet pumping and pumping. Gas lift uses a gas to aerate the fluid in downhole to modify the mixture properties and consequently reducing the friction losses in the flow path while it increases the pressure in the bottom hole. Jet pumping utilizes an accelerated flow to create suction required to take the well fluid into the injected fluid stream. This down-hole equipment creates enough lift to direct the flow to the surface without using moving parts. The latter is pumps which are categorized as rod pump and rodless pumps. In rod pumping, a rod is used to transfer energy to the down-hole pump but in rodless pumping electrical or hydraulic power in down-hole is being utilized to provide the required power to the pump. A variety of pump types are used in rodless pumping method which are centrifugal, positive displacement, or hydraulic pumps. Electric submersible pumping (ESP) uses a submerged electrical motor coupled to a multistage centrifugal pump. They are mainly being used to produce large volumes of fluid.

The first ESP pump was invented by a Russian named Armais Arutunoff in 1910s. The first ESP pump started operation in 1926 in Kansas. Since then, the process of development and improvement for ESPs has resulted in approximately 10% of the oil production throughout the world. The production rate of typical ESPs ranges from 20,000 to 35,000 bpd up to a depth of about 10,000ft.

ESPs are centrifugal pumps which are typically mixed flow type of pumps. The fluid is accelerated by the impeller and its pressure rises in both the impeller and diffuser. A typical mixed flow centrifugal pump is shown in Figure 1-1.

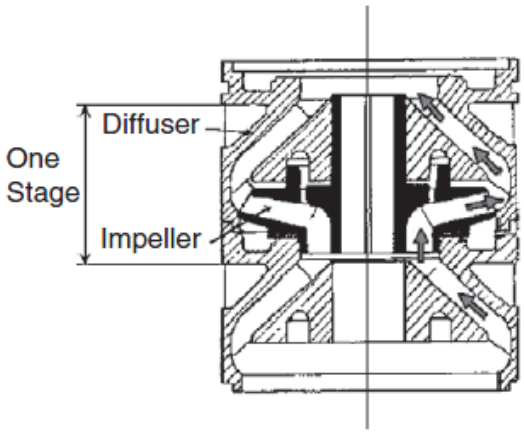

Figure 1-1: Section view of a single stage centrifugal pump

The ESPs underwent some improvement such as adding a VFD to control the speed of the motor. Another improvement utilizes gas separators in wells where free gas beside the liquids is present in well. ESP pumps are severely degraded by the presence of free gas in their inlet. The resulting degradation can vary from a slight deterioration in the pump performance to the surging and even to the gas locking caused by entrained gas in the flow path (Zhou (2010)).

One way of overcoming the aforementioned problem is to use gas handling pumps such as an ESP-MVP Baker Hughes Pump. It is an ESP pump with a split-vane design on the impeller and modified size balance holes. Modifications have been done on the impeller

blade and balance holes to give the capability to pump a liquid with high gas content up to 70%. These pumps can be used as standalone or be employed in series with another ESP pump for boosting. MVPs in addition to boosting the fluid are capable of homogenizing the flow efficiently.

The split-vane design eliminates the generation and accumulation of gas pockets near the vane while the larger balance holes can break up the gas pockets and help in homogenizing the flow. A schematic view of the MVP pump with the blade configuration and oversized balance holes has been shown in Figure 1-2.

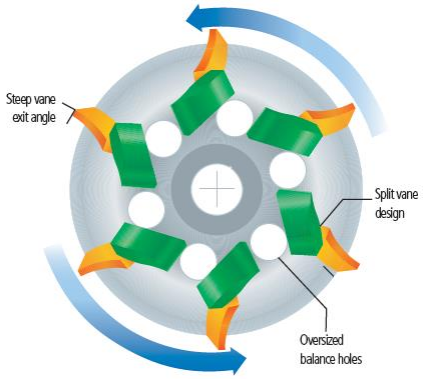

Figure 1-2: Schematic view of the MVP pump with the blade configuration and oversized balance holes

In Figure 1-3, a section view of a 3-stage and multiple-stage MVP-ESP pump is shown. Each stage is composed of split-vane design impellers and a diffuser to redirect the flow to the next stage. In a multiple-stage MVP pump, the first stage causes the flow to be

homogenized; therefore the pressure rise across the first stage is lower than the following stages in the flow path. MVPs are mainly being used to homogenize the flow while they provide some boosting which is lower than typical ESPs. In industry, MVPs are located at the inlet of the ESPs to provide a homogenized flow with smaller bubbles and lower GVF (because of pressure rise across the MVP). With the inlet condition which has been almost idealized for ESP with MVP pump, ESP would provide the main necessary pressure rise required for artificial lifting in gassy oil wells.

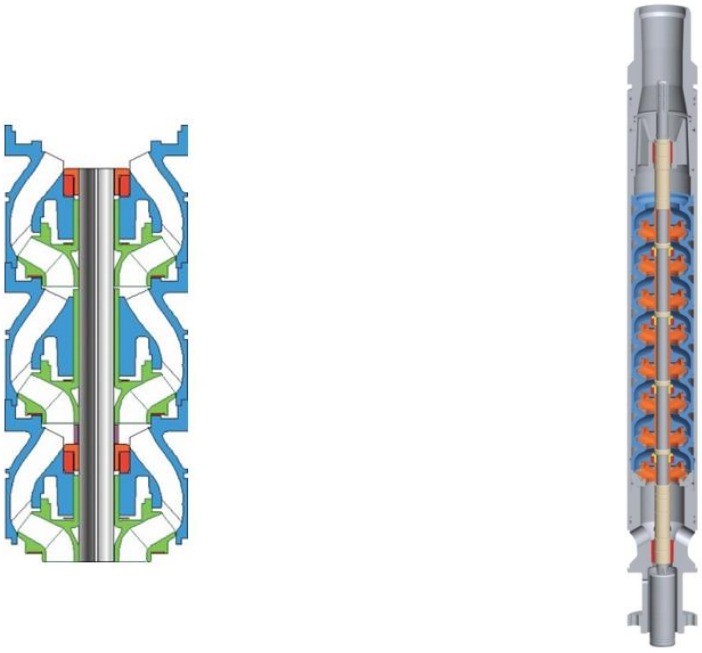

(a) (b)

Figure 1-3: Section view of (a) 3-stage MVP-ESP pump, (b) multiple-stage MVP-ESP pump with inlet and outlet

Typical ESP pumps have a continuous blade rather than a split-blade. Therefore, they are not able to handle as high of gas volume fraction as MVP pumps. Erosion is one of the

parameters that influences the lifetime of the ESPs. So, the key parameters that are causing the erosion process in pumps need to be identified. Consequently, according to these parameters, design consideration required to be carried out to reduce the erosion influence on the pump performance and prevent the possible failures caused by erosion.

In Figure 1-4, an ESP pump which is a mixed flow pump is shown.

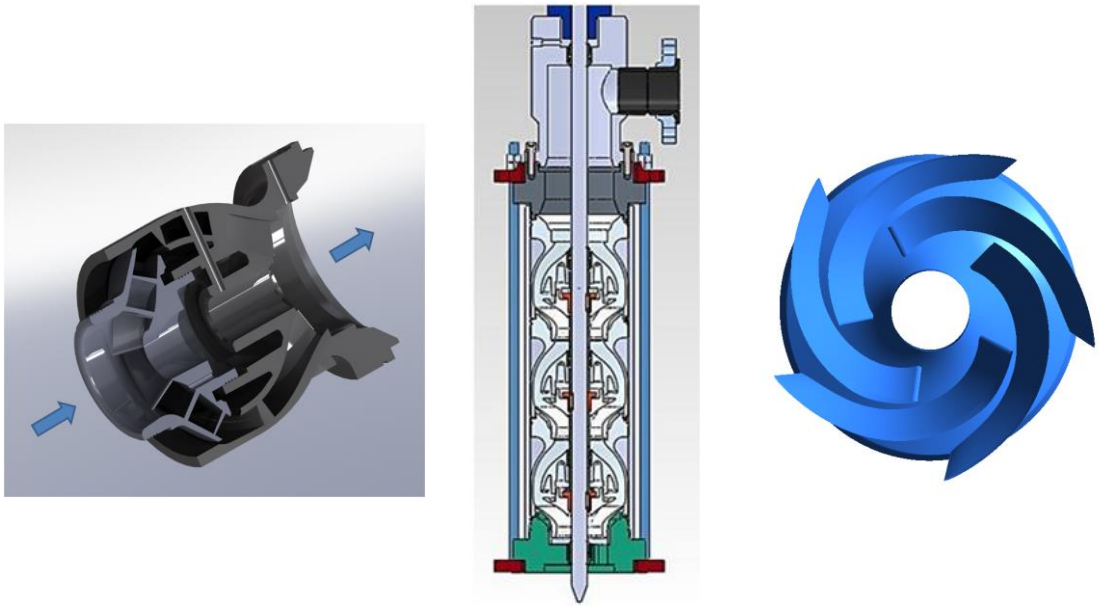

(a) (b) (c)

Figure 1-4: (a) Cross section of a single stage ESP with impeller and diffuser (b)Three-stage ESP pump (c) ESP impeller

1.1. Experimental Studies on the Fluid Flow in Centrifugal Pumps

To study the performance of ESPs in two-phase conditions considerable effort has been made. However, due to the complexity of fluid flow in these pumps, it is still a challenging

problem and researches are going on to predict the performance of the pump for different operating conditions.

Most of the research that has been done on centrifugal pumps focus on the nuclear industry used in the primary coolant circuits of the majority of pressurized water reactors (PWRs). In comparison with ESPs, they have single stage rather than multiple stages with much higher inlet pressure. Centrifugal pumps used in nuclear industry have volute type design compared to diffuser type design in ESPs and larger in diameter with an open-type impeller.

Mitsukiyo and Kiyoshi (1974a) are the first group who did a comprehensive study on the performance of centrifugal pumps. Mitsukiyo and Kiyoshi related the head degradation of a two phase pump to the amount of entrained gas in an open-type impeller with volute-type diffuser pump. They observed that rate of head degradation changes for different flow rates and gas volume fractions due to the change of gas-liquid flow patterns in the impeller. Utilizing a high speed camera, they visualized the flow pattern for different operating conditions of the pump. Authors were able to identify four flow regimes: isolated bubble, bubbly flow, slug flow and segregated gas. As the gas content in the flow increases the amount of bubbles and air pockets at the inlet region of the pump tends to increase. In slug flow, air pockets form and move out of the region and generate oscillations in the flow. Once the air pockets stay in the inlet region, segregated gas flow regime occurs which reduces the cross section of the flow. When this stationary gas pockets enlarges at the inlet

of the impeller region, they take over the entire region resulting in almost zero head and flow. This phenomenon is called gas lock.

In another work, Mitsukiyo and Kiyoshi (1974b) studied the effects of number of blades on the performance of the pump. The authors found that the behavior of the pump with lower number of blades is different than higher number of blades. When the number of blades is low, a slight increase in head has been observed for low gas content. According to the authors, low amount of air bubbles shift the mean flow to the suction side of the impeller and consequently changes the peripheral component of the absolute velocity which results in a rise in pressure head. According to the authors study, the bubble size reduces as the impeller speed or the number of blade increases.

Runstadler (1976) conducted a study to monitor the performance of a two-phase pump in different operating conditions used in nuclear industries. To be able to facilitate the creation of a model to study the performance in two-phase conditions, the authors emphasized understanding the flow physics within the pump. As it has been shown by subsequent investigators, flow separation and flow pattern in the impeller play an important role on the performance of the pump. Investigators after this report tried to include the flow dynamics to enhance their models.

Mitsukiyo and Kiyoshi (1976) studied the influence of clearance between impeller blades and casing in air admitting condition for both open-type impellers and close-type impellers (clearance in close-type impellers is distance between shroud and casing). The authors found that the ratio between the clearance and channel depth(λ) is more important than amount of clearance. For water-only condition, in open-type impellers reducing λ to 0.006 causes an increase in the pump performance in comparison with normal clearance of 0.061. For water-only condition, in close-type impeller λ causes a slight change in the performance of the pump.

In two-phase condition, on the open-type impeller, increase in λ results in head degradation in the pump performance. Change of inlet gas volume fraction causes surging within the pump. This phenomenon gets worse in lower clearance ratios. By increasing clearance ratio the effects of surging diminishes. A close impeller type of pump is quantitatively similar to open-impeller. The clearance ratio of $0.044 < \lambda < 0.1$has been recommended.

The obtained results for two-phase condition were conducted for gas volume fractions lower than 10%. Since results are pump specific, they cannot be necessarily applicable for other pumps but this report is the only study that deals with clearance of the pump in two-phase conditions.

Winks (1977) conducted an experimental study on a 10-inch air-water mixed flow type of one-third scaled pump. For the inlet pressure varying from 20-120psi the authors conducted experiments for different inlet gas volume fractions and observed oscillation in flow in GVFs in the range between 10-25%. Maximum oscillations occurred at around 20% inlet gas volume fraction. By increasing inlet gas volume fraction, the amount of head degradation increased.

Zegley (1977) performed experimental, theoretical and flow visualization on a centrifugal pump with a simple volute. He observed that head degradation is a function of void fraction, flow coefficient and two-phase flow pattern. In agreement with the results that were obtained by Murakami, he confirmed that the transition from one flow regime to another flow regime between inlet and outlet of the impeller plays an important role in the performance of the pump.

Patel and Runstadler (1978) studied the performance of a 1/20- scale model centrifugal pump operating in two-phase condition without the shroud to be able to visualize the flow in the impellers.

Since flow dynamics in two-phase conditions are very different scaling would not be applicable. Therefore, the authors decided to study and model the flow dynamics and

interaction of different phases in a rotating channel to investigate the feasibility of modeling a two-phase pump.

They found two flow regimes occurring in the pump. In low gas volume fractions a bubbly flow with a low amount of head degradation was observed. By increasing the amount of gas content, a void started to enlarge and separate the regions of bubbly flow from each other. By further increase of GVF, a steady growth of head degradation occurred. Since this pump was an open-shrouded pump its results cannot be applied to ESP pumps.

Mikielewicz (1978) tried to quantify how the head degradation occurs in a single stage two-phase pump. The authors obtained the following Eulerian equation for two-phase flow in a centrifugal pump:

$$\psi = 1 - \frac{\phi_{tp2}}{tan\beta_2}\frac{(1+a_2)(1+a_2 s_2^2)}{(1+a_2 s_2^2)} - \left(\frac{d_1}{d_1}\right)^2 \phi_{tp1} tan\gamma_1 \frac{(1+a_1)(1+a_1 s_1^2)}{(1+a_1 s_1^2)} \tag{1.1}$$

ψ: Head coefficient, (apparent pump head under two-phase condition)/$\frac{U_2^2}{g}$,

a_i: Two phase property formation at inlet (a_1) and outlet (a_2)

$= \left[\frac{\alpha\rho_g}{(1-\alpha)\rho_L}\right]$,

ϕ_{tpi}: Two-phase flow coeficient

$=(\dot{M}_g + \dot{M}_L)/\left[(1-\alpha)\rho_L + \alpha\rho_g\right]/A_i/U_i,$

s :slip velocity ratio= $\frac{V_g}{V_L}$

The main disadvantage of this equation is the lack of information about slip ratio and its variation mechanism across the impeller.

A dimensionless head loss ratio is defined according to friction losses and two-phase flow separation losses as:

$$H^* = \frac{\Delta H_{\text{otpth}} - \Delta H_{\text{otp}}}{\Delta H_{\text{ospth}} - \Delta H_{\text{osp}}} = \frac{(\frac{1+a}{1+sa})^2 + k\left[\frac{(1-\alpha)}{(1-\alpha+\alpha s)} - \epsilon\right]^2}{(1-\alpha)(1+a)(1+k(1-\epsilon)^2)} \quad (1.2)$$

ΔH_{otpth} = total head, theoretical value for two-phase conditions,

ΔH_{otp} = total head, actual two-phase conditions,

ΔH_{ospth} = total head, theoretical value for one-phase conditions,

ΔH_{osp} = total head, actual one-phase conditions,

ϵ $=Q_{bep}/Q_{tp},$

k =pump-dependent constant

This method is a pump dependent method and can give good results only for the cases where ratio between head degradation with respect to inlet pressure is small. Also the effect of flow pattern in impeller has been overlooked and the influence of high liquid velocity with respect to gas velocity within impeller section on fluid flow has not been considered.

Runstadler Jr and Dolan (1978) conducted a qualitative study based on the data collected from a two-phase pump used in nuclear industry. They observed that there are three parameters affecting a two-phase pump performance, inlet gas volume fraction, pump flow coefficient and inlet flow regime. As it has been show by subsequent investigators, the flow regime within the impeller has a more important role on the performance of the pump and can be quite different than flow regime at the inlet.

Also, they found that surging can be eliminated by increasing the superficial velocity of the liquid phase to more than 50% of the corresponding velocity at the best efficiency point.

Based on the authors' results, almost 80-100% of head degradation across the pump occurs in the impeller. Meanwhile, they verified that the affinity laws applicable for single phase cannot be applied for two phase flow pumps.

Zakem (1980) obtained a simple model for a one-dimensional flow through a straight channel. He did not consider gas and liquid separation and bubble dimension change throughout the pump. He included the effects of flow pattern in the impeller into his model formulation. The set of equations obtained from continuity and momentum for both phases was integrated along a streamline parallel to the blades.

Lea (1982) conducted the first study on a two phase ESP pump available in the petroleum industry. They studied the performance of the Centerilift's pump with air-water and Diesel-CO_2. Air-water test was conducted on a 5-stage I-42 pump covered by a 7-inch ID Plexiglass. The intake pressure was held below 30 psig. The inlet water and air flow rates were measured by orifice flow meters. The schematic of the test facility is shown in Figure1-5.

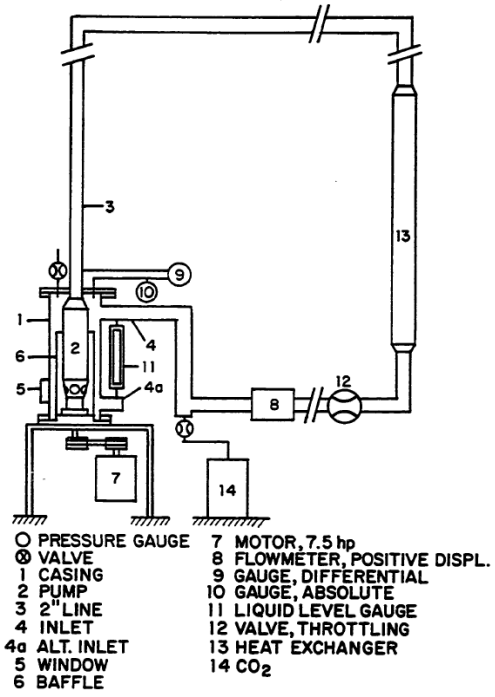

Figure 1-5: Air-Water test facility in Lea-Bearden report

Diesel-CO_2 tests (Figure 1-6) were conducted on two radial pumps, I-42B and C-72 and on one mixed flow pump K-70 (Figure 1-7). The last two pumps have been chosen in such a way that the optimum flow rate among them is almost the same. The test facility is designed to operate up to 400 psig with the maximum inlet gas volume fraction of 50%. The casing used for these set of experiments was 8-inch with two embedded windows.

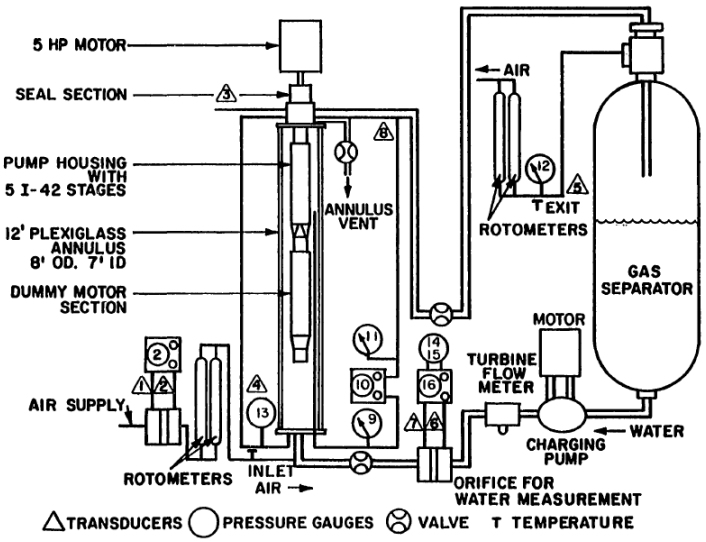

Figure 1-6: Diesel-CO2 Test Facility used in Lea (1982) work

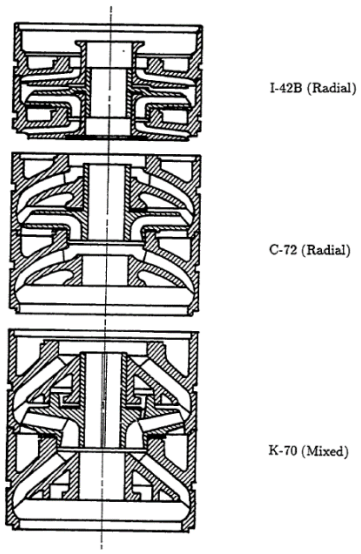

Figure 1-7: ESP pump stages used in Lea (1982) Report

According to their obtained results from the test fluid of Air-Water and Diesel-CO_2, the pump performance was seen to be dependent on inlet pressure, type of fluid, gas volume fraction and pump type. By increasing gas volume fraction, the amount of head degradation increases and the operating range of the pump decreases. The gas lock in the pump for air-water was reported to occur around 14% GVF. The authors observed that severe pressure surges happened in lower liquid flow rates located toward the left end of head flow rate curve.

Comprehensive data captured from Diesel-CO_2 conducted on three different pump shows that mixed flow type of pump represent more resistant to head degradation by admitting air into the system. Decreasing the air content and increasing the inlet pressure enhances the performance of the pumps. Meanwhile, increasing inlet pressure increases the operating range of the pumps.

Kim (1983) has done an overview on the two-phase models that have been developed for centrifugal pumps in the nuclear industry. The author proposed a better study on the following parameters.

1. Inlet Gas Volume fraction: The amount of air is of great importance. It can lead to either bubbly flow or separated flow along the pump. According to pump geometry, the air bubbles at the inlet can coalesce and result in head degradation.

2. Flow regime: Flow regime at the inlet has been mentioned by the author to be an important factor. But, as it has been shown by the other investigators, the piercing effect of impellers can change the flow pattern completely in the impeller section and a bubbly flow or separated flow can be the result of it.

3. Pump Head: There are different definitions for pump head. Some people define it based on the density of the mixture at the inlet whereas others define it based on the average density. In multistage pumps, this problem would be further complicated.

4. Inlet pressure effect: The authors determined that by increasing the pressure at the inlet it is possible to enhance the pump head.

Sekoguchi (1984) studied the variation of void fraction within a transparent impeller using electric resistivity probe. The single stage pump had a maximum flow rate of $0.33m^3/s$ with the corresponding head of $11m$ working at speed of$1250RPM$. Considering this operating point as the full load capacity, measurements were performed for 30%, 40% and 50% of full load capacity. The eight resistivity probe used it this study embedded individually in the following places.

1. Shroud side
2. Center of the impeller

3. Hub side

The maximum error in the measurement of gas volume fraction using resistivity probes was 5%.

For low inlet gas volume fractions bubble flow was observed. When the gas volume fraction at the inlet is less than 2%, bubble movement from the suction side of the impeller blade to the pressure side of the impeller blade occurs. By increasing the flow rate of the pump, the onset of formation of air slugs within the impeller increases. When the formed air slugs start to leave the impeller, the pump surge happens. Since air slugs occupy a substantial portion of the cross section of the impeller, it results in a significant increase in the velocity of the liquid phase. These slippages between the phases are an important factor pertaining to head degradation.

Poullikkas (2003) conducted an experiment to visualize the bubble motion within the impeller of nuclear reactor cooling pumps. The author observed that at low gas content, gas bubbles tend to concentrate at the impeller eye on the suction side of impeller. At medium gas volume fractions, gas pockets advances toward the passage length. Around 9% gas volume fraction, gas-lock occurred in the pump.

Fujie (1985) studied the amount of torque required for a single stage pump to run. The uncoupled momentum equations of gas and liquid phase were used. The force interaction

between phases was considered by assuming an arbitrary friction coefficient to be obtained from correlated data.

Tarpley (1984) used a simplified model to predict the performance of an ESP pump by just considering gas compression as the only source of degradation. The data obtained by Lea Burden was used to develop the model. Since, no other source of head degradation had been used and the effect of gas compression in comparison with other source of head degradation was not possible. The model obtained good results for gas volume fractions which are less than 2%.

Furuya (1985) developed a model to analyze the flow behavior in a centrifugal pump for water-steam as the test fluid. Employing the Drift Flux model, mass, momentum and energy equations were derived. The slippage and its effect were studied by analyzing the momentum of the gas bubbles flowing in the impeller according to the work done by Hench (1972). Furuya estimated the amount drag force exerted on the bubble according to the work done by Hench and Johnston which was originally done for flow in pipes in two phase conditions. The drag coefficient was assumed to be $C_D = 0.54$ for the values of α less than 30% in a bubbly flow regime. When the value of gas volume fraction was between 30-40% a linear change in drag coefficient was considered in the model. For values greater than 40%, where churn-turbulent flow was assumed to exist within the impeller, Eq. (1.3) was used to calculate the void fraction.

$$\frac{C_D}{r_b} = 2.79(1-\alpha)^3 \tag{1.3}$$

Sachdeva (1988) proposed a model for single and two-phase ESP pump to study head degradation within the pump. He utilized different friction factors to include the friction losses that occur due to curvature, rotation and rectangular-cross section. In his model, different parameters such as pump geometry, inlet pressure, inlet gas volume fraction, fluid properties and number of stages are considered. The dynamics model presented by Sachdeva is different from the models proposed by other investigators since it deals with each phase individually in deriving the equations for momentum balance whereas in other works, mixture momentum balance equations are being considered. In comparison with the work done by Furuya, assumption of a constant bubble diameter has not been done and it varies for different operating conditions of the pump. The author has tried to correlate the amount of $\frac{C_D}{r_b}$ based on overall pump performance. The only undetermined variable in his equations is the amount of r_b considered to be a function of inlet condition and liquid flow rate.

Cirilo (1998) performed experiments on three different submersible pumps. Two of them were mixed flow type pump while the other one was a radial pump. Air-water was used as the test fluid. Experiments were performed for different inlet pressure and gas volume fraction and speeds. The author observed the capability of the pump in handling higher gas volume fractions increases by increasing inlet pressure. Mixed flow type pumps showed a better performance in comparison with the radial pumps in handling free gas at

the inlet. He concluded that an increase in the number of stages would result in an improvement in the performance of the pump, because pressure rise in downstream stages causes an increase in the flow rate of upstream stages and as the result pressure rise increases for later stages.

Pessoa (1999) conducted some experiment on a tapered, 20-stage, axial flow pump which had 104 mixed flow stages. Real crude oil and natural gas were used as the test fluid. The test were performed on two kinds of crude oil which were light (32.5°API) and heavy (11.6°API) .Inlet pressure was varied from 150 to 400psig. The maximum inlet gas volume fraction that ESP with light oil was able to handle was 50% while for the heavy oil it was 42%. In contrary to light oil, no gas lock happened for heavy oil.

Romero (1999) studied the performance of a gas handling stage with a slotted impeller which was designed to increase the capability of the ESP pump in handling higher gas volume fractions. An advanced gas handler (AGH) manufactured by Schlumberger was installed upstream of an ESP pump, GN4000 pump, to provide the homogenous mixture for the ESP pumps. Performance curves for air-water mixture were obtained for different inlet pressures and gas volume fractions for combined AGH and GN4000 configuration. To predict the pump head performance a multiphase model was evaluated. In order to identify the stable operating condition, the author aslo calculated the maximum no-slip

inlet gas volume for AGH and combined AGH-GN4000 configuration. Another correlation was developed to predict the limiting flow rate at onset of surging.

Pessoa and Prado (2001) conducted various experiments on a two-phase ESP pump, GC-6100, with 22 stages manufactured by Centrilift. The experiment was performed by varying the inlet gas volume fraction and water flow rate while the inlet pressure and rotation speed were kept constant. According to the author, as the flow rate increases the surging moves from the downstream stages to the upstream stages. As the result of his findings, a study of an individual stage is necessary rather than looking at overall performance characteristic of entire stages. Overall pressure increase and overall power consumption throughout the entire pump was measured.

Estevan (2002), for the first time on ESPs, performed experimental and visualization studies to formulate a one-dimensional model for two-phase studies. The author used a scaled-down transparent radial pump. A high speed camera with stroboscopic light was used. Estevan observed an elongated or stationary bubble at the entrance of impellers, when the size of the elongated bubble reached a critical size, surge within the pump started to happen. The critical size and onset of it depends on the inlet condition and other operating conditions of the pump. Since the impellers blades do not have a hub, it may deviate the results from the existing conditions of commercial ESPs. He developed a model based on his observations, two-fluid approach and using hydraulic correction

factors. The values of drag coefficient were varied according to the observed flow pattern in the impeller. The author introduced surging indicator factor which is the relationship between drag and buoyancy forces exerting on the bubble. This coefficient shows the tendency of the bubble to be a stationary or moving bubble.

Duran (2003) conducted experiments to study the flow within an ESP with water and air as the working fluid. The author considered different inlet and gas volume fraction where water flow rate was changing. According to the author, three flow regimes exist in the pump according to the operating condition: Bubbly Flow, Elongated Bubble and Transition. He proposed some correlations to relate head degradation to the corresponding flow regime which exists in the pump. The correlations for head degradation were functions of fluid densities and flow rates.

Barrios (2007) developed a semi-experimental model to study the operation of a transparent ESP pump on its second stage. The impeller was an open-type impeller to facilitate the visualization throughout the blades. Applying a momentum balance on the individual gas bubbles using the experimental observations, she obtained a correlation to relate drag coefficient to flow regime exists in surging condition. She also developed a model to correlate the gas bubble diameter to the operating condition of the pump.

Gamboa (2009) conducted experiments in conjunction with visualization on a transparent prototype. The author performed an extensive number of experiments by varying inlet pressure and gas volume fraction, water flow rate and speed. He generated an operation map according to that. The author observed a cluster of bubbles that when surging starts to happen they coalesce and generate air pockets. He also performed experiments on SF_6 to replace air in his experiments which has density much higher than air. Surging occurred at much higher GVFs in comparison with air but the amount of head degradation remained the same. Studying the effects of adding a surfactant was also done by Gamboa. He found that due to non-coalescing effects of the surfactant, surging occurs at higher gas volume fractions.

1.2. Electrical Impedance Measurement in Two-Phase Flow

1.2.1. Electrical Resistance Tomography

1.2.1.1. Introduction to Electrical Resistance Tomography

To illustrate the concept of electrical resistance tomography two articles are used. One is the work done by Dickin (1996) and the other one is Butler (1998).

Dickin (1996) developed an electrical resistance tomography (ERT) which is a modified version of the ERT systems utilized in biomedical applications. In ERT systems, current is injected between two electrodes while other electrodes are used for measuring voltages. These boundary voltage measurements are applied to reconstruction image models to map conductivity distribution within a process fluid. A typical ERT system which is composed

of sensors, data acquisition and image reconstruction system is shown in Figure 1-8. The amount of variable current applied to the electrodes varies from 0 to 30mA (peak-peak) with the excitation frequency from 75 *Hz* to 153.6 *kHz*.

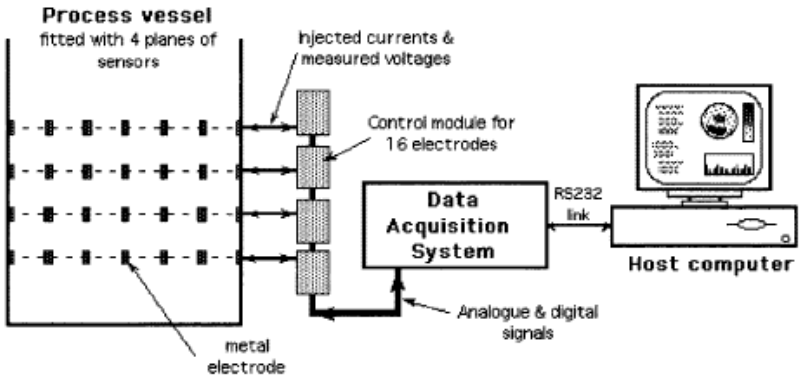

Figure 1-8: 4 plane ERT system used in a process vessel (Dickin (1996))

In the ERT system, the conductive electrodes are in direct contact with the process fluid. The conductivity of electrodes used in ERT should be higher than the process fluid in order to obtain a better signal to noise ratio. The electrodes are placed an equal distance from each other all around the process vessel. To ensure better accuracy in image reconstruction, positioning error of the electrodes should be less than $\pm 0.1\%$. Ideally, the electrodes for injecting current should be bigger than the electrodes used for measuring voltage. However, similar sized electrodes can be replaced with the minimal loss of sensitivity in voltage measurement. The installed electrodes should have connectivity throughout the process fluid and not through the vessel.

There are different strategies for data collection. Among different strategies, four of them usually are applied which are: adjacent, opposite, diagonal and conducting boundary.

In the adjacent strategy, current is injected between two adjacent electrodes and voltage is measured from pairs of neighboring electrodes (Figure 1-9). This procedure is repeated for all electrodes all around the circular array. The number of independent measurements is $N(N-3)/2$ where N is the number of electrodes.

Non-uniform distribution of current in this strategy and its sensitivity to noise makes this strategy non-efficient but since it is easy to be applied for image reconstruction schemes and required minimal hardware, it has been popularized.

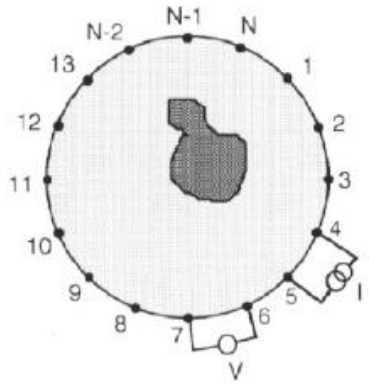

Figure 1-9: Adjacent data collection strategy (Dickin (1996))

In the Opposite strategy, current is injected between to diametrically opposed electrodes. The voltage is measured between other electrodes and an electrode located beside the injecting current electrode as the reference electrode (Figure 1-10). This procedure is repeated until all independent measurements are done. The total number of independent measurements for this strategy is $\frac{N}{4}\left(\frac{3N}{2}-1\right)$. In comparison with adjacent strategy, the total number of independent measurement in this strategy is lower but it is less sensitive to conductivity changes at the boundary and also it has more even current distribution.

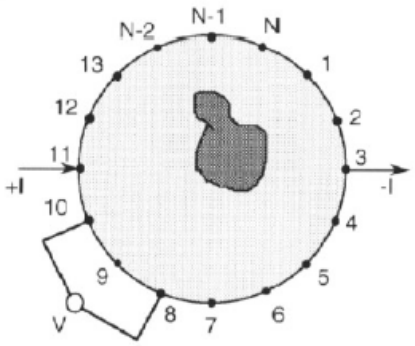

Figure 1-10: Opposite data collection strategy (Dickin (1996))

In the diagonal strategy, which is also called cross method, current is injected between a pair of electrodes positioned diagonally. According to Figure 1-11, electrode No.1 is selected as the current injecting reference electrode and electrode No.2 is selected as the reference for voltage measurements. Each time current is injected between electrode numbers 3,5,…,15 and the reference current injecting electrode (electrode No.1). For each

individual current injection pairs, voltage is measured between other electrodes and electrode No.2 as the reference electrode except current injection pair's electrodes.

Then, the current reference is switched to electrode No.4 and voltage reference to electrode No.3. Now, the current is injected between electrodes 6,8,…,16, 2and voltage is measured on the rest of the electrodes with respect to the reference electrode (Electrode No.3). Therefore for each pair of current injection electrodes (in total 7 current injection pairs for the same reference current injection and voltage) 13 voltage measurements are made. For the same current injection and voltage references, 91 data points can be captured. By changing the reference as described above the total number of 182 datapoints can be obtained for a 16 electrode array in which only 104 of them are independent. This strategy, in comparison with diagonal strategy, has a lower sensitivity around the boundaries of the vessel but better image qualities can be obtained by employing this method.

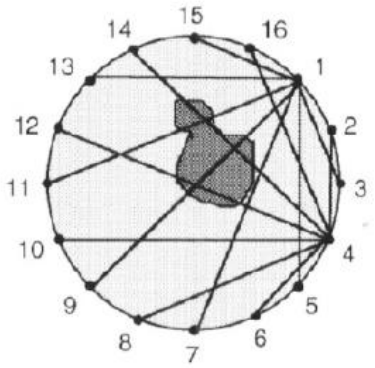

Figure 1-11: Diagonal data collection strategy (Dickin (1996))

This strategy can be used for the vessels with conductive walls. The electrodes are assembled on walls with insulating material to avoid the electrical connectivity of electrodes to the wall. In this strategy, as it can be seen from Figure 1-12, the conducting boundary is grounded to the same ground as the voltage measurement ground. Also the wall is used as the current sink. For each current injection, a set of voltage measurement all around the vessel is done except the injecting current electrode. This procedure is repeated by switching the injecting current electrode and new set of voltage measurements. The large wall used as the ground reduces the common-mode voltage between measurement electrodes.

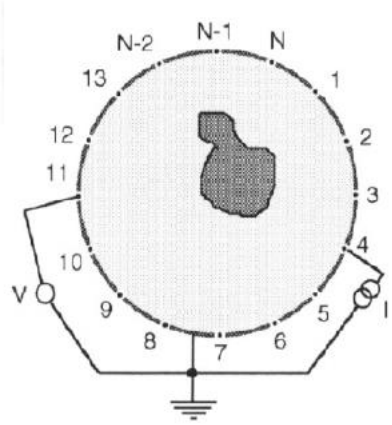

Figure 1-12: Conducting boundary measurement data collection strategy (Dickin (1996))

After all the independent voltage measurements are performed along the boundary of a vessel, a numerical algorithm (data inversion) is used to obtain an approximate value for

the conductivity distribution inside the vessel. Then, the resultant conductivity distribution is related to the component distribution within the volume which is under study. The problem in which collected data set is converted to the conductivity distribution is called the inversion problem.

To be able to solve the inverse problem, a problem called forward problem should be solved iteratively. In the forward problem, for a given conductivity distribution boundary values are calculated and compared with the collected data.

Process fluid within the vessel follows ohms law (Eq. (1.4))

$$J(x,y) = -\sigma(x,y)\nabla\varphi(x,y) \tag{1.4}$$

Where

J: Current density

σ: Electrical conductivity

φ: Potential

Considering injecting electrodes and non-injecting electrodes, the boundary conditions are set to solve the problem by assuming that the current density is uniform for the pair of injecting electrodes and also other electrodes do not make any disturbances to the potential field distribution.

The forward problem is applied to solve non-linear inverse problem. This method is an iterative method and takes long time to apply it for each current injection pairs.

Instead of solving the full non-linear inverse problem, it is possible to linearize the problem and solve it in one step. Linearization is done by linearizing the integral (Eq. (1.5)) obtained from Geselowitz compensation theorem (Butler (1998)).

$$Q(\phi_{Q+} - \phi_{Q-}) - q(\psi_{q+} - \psi_{q-}) = \int_{\Omega} (\sigma_{\varphi} - \kappa_{\psi}) \nabla\varphi . \nabla\psi dV \tag{1.5}$$

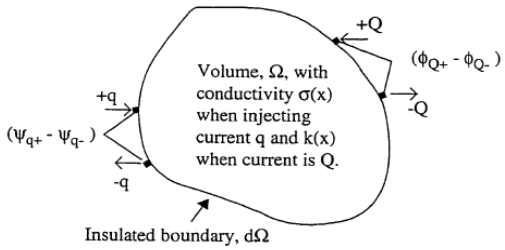

Figure 1-13: Current injected on electrodes with the current of q develops a potential difference of ψ between the same electrodes, Current injected on electrodes with the current of Q develops a potential difference of φ between the same electrodes (Butler (1998))

According to Figure 1-13, φ is the measured potential difference between the current injecting electrodes with the current value of Q in the media with the conductivity of $\sigma_{\varphi}(x)$ while ψ is the measured potential difference between the current injecting electrodes with the current value of q in the media with the conductivity of $\kappa_{\psi}(x)$.

$\kappa_\psi(x)$ is chosen to be a constant value throughout the media. By this assumption, $\sigma_\varphi(x)$ and its gradient remain unknown. If the deviation of the conductivity value from the mean value is small, the potential difference, φ, is found by Laplace's equation. The only remaining unknown would be the conductivity distribution $\sigma_\varphi(x)$. One way to obtain a solution is to divide the solution domain into separate elements with a constant conductivity. Therefore, the integral equation changes to the following equation.

$$\sigma_j \int_{\Omega_j} (\nabla\varphi_i . \nabla\psi)_i dV_j = \psi_i \tag{1.6}$$

In the above equation,ψ is the boundary measurements while σ is the conductivity in each individual cell Ω_j. The indices irepresents the voltage measurement pair.

Ahmed and Ismail (2008) obtained two innovative designs for two phase flow identification by capacitance measurements. The changes in dielectric properties within a two phase flow vary the response of the sensor. Two electrode designs are shown in the following figures.

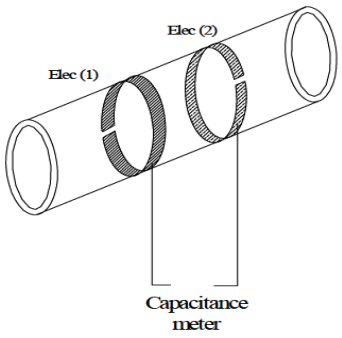

Figure 1-14: Ring Type capacitance sensor design by Ismail (2008).

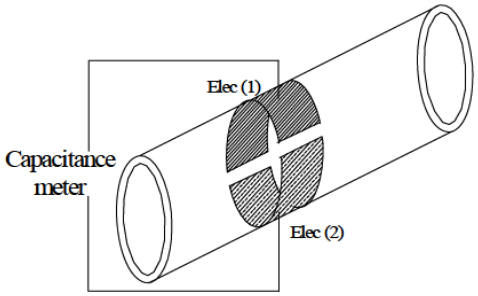

Figure 1-15: Concave type capacitance sensor design by Ismail (2008).

According to Figure 1-14, the ring type design, ring electrodes separated in the axial direction are embedded circumferentially within the tube. The small gap is designed for the purpose of facilitating the installation of electrodes. In the concave design, Figure 1-15, two brass strips are located on opposite sides of the pipe and embedded on the circumference of the tube. For the same spatial resolution, the ring type sensor has more sensitivity. Authors used the probability density function or power spectral density of the electrodes response to characterize the flow pattern. Flow regimes which are elongated bubble, slug and annular flow has been investigated by the aforementioned method. The results have been verified by using a high speed camera.

1.2.2. Impedance Needle Probe

1.2.2.1. Introduction to Impedance Needle Probes

Uga (1972) conducted experiments in an operating natural circulation in a boiling water reactor (BWR) to determine bubble size distribution inside a vapor-liquid two-phase flow. The author used a digital type void meter and a bubble speed meter and related them to

each other in the form of an integral equation. The detail drawings of the digital void meter and bubble speed meter are shown in Figure 1-16 and Figure 1-17. The digital void meter has a single electrode tip whereas in the bubble speed meter has two electrodes were used and placed at a specific distance.

The integral equation comes from the relationship between the probability density function F(D) of bubble diameter and penetration length g(x) for the distribution of bubbles in a two phase flow regime.

$$g(x)dx = \int_{x}^{\infty} f(x)dxF(D)dD \tag{1.7}$$

The probes were used at the same location one at a time.

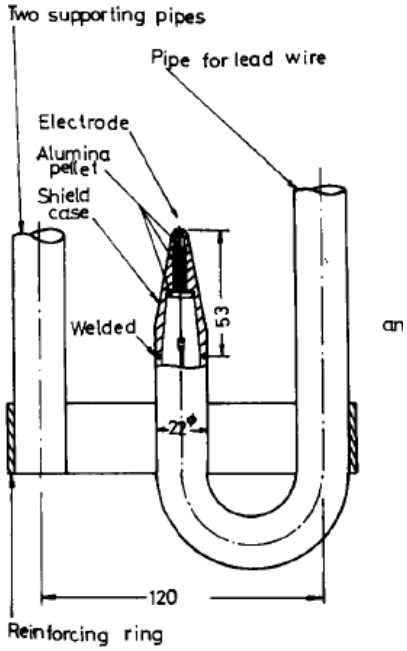

Figure 1-16: Digital Void meter (Uga (1972))

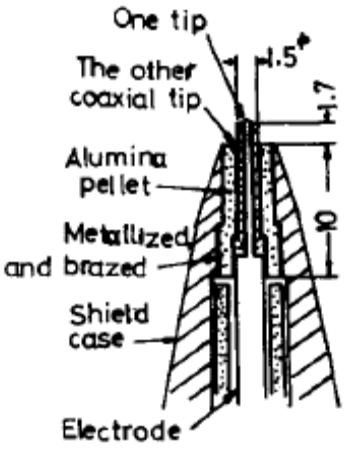

Figure 1-17:Bubble speed meter (Uga (1972))

Munholand (2005) designed four different conductive needle probes to identify the performance of each one in measuring gas volume fraction and bubble velocity. A camera was used to validate the results obtained from the needle probes. The four conductive needle probes are shown in Figure 1-18.

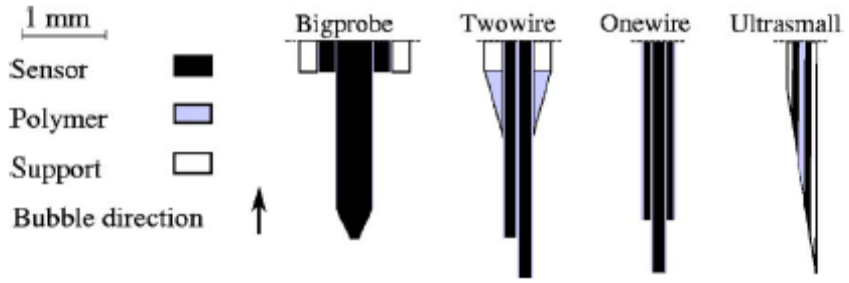

Figure 1-18: Four designed probes by Munholand (2005)

The test setup to investigate the probe performance is shown in Figure 1-19.

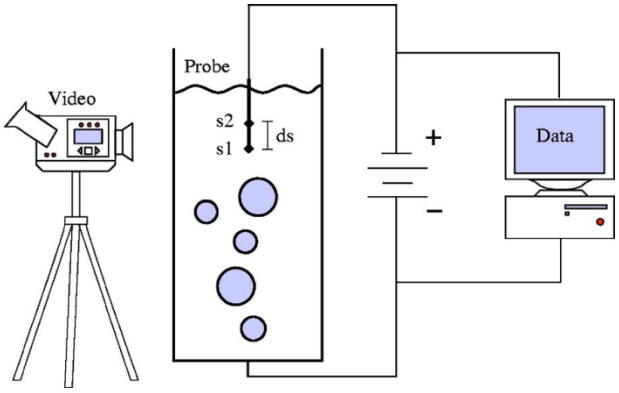

Figure 1-19: Test setup to quantify the probes performance used by Munholand (2005)

Double probe designs consist of two sensors installed in s_1 and s_2 with a distance of d_s. Two separate conductive measurements are performed between these sensors and the ground installed at the bottom of the tank as is shown in Figure 1-19. By knowing the

distance between the sensors and the time at which individual voltages start to decrease indicating the presence of gas, the bubble velocity in a single direction can be measured.

The probe performance has been compared by the number of detected bubbles by each probe. The authors found that one-wire and two-wire probes detect more bubbles in comparison to the big probe. It happens due to the small gap between sensors. The ultra-small probe detected the least number of bubbles. The low performance of ultra-small probe has been explained by signal to noise ratio (SNR). Decreasing the sensor diameter causes the SNR to increase while according to the theory the smaller the size of the sensors are the better the performance of the probe is.

Dyakowski (2005) performed a feasibility study to characterize heterogeneous flows by means of a dual modality sensor (Figure 1-20). The two measurement modalities are electrical and ultrasound. The two electrodes that were utilized to measure electrical response were connected to a piezoelectric layer. The probe consists of two transducers. In each transducer, a piezoelectric layer has been sandwiched between two layers of electrodes. Two transducers are placed in such a way that the second electrode from each individual transducer can be utilized for electrical measurement.

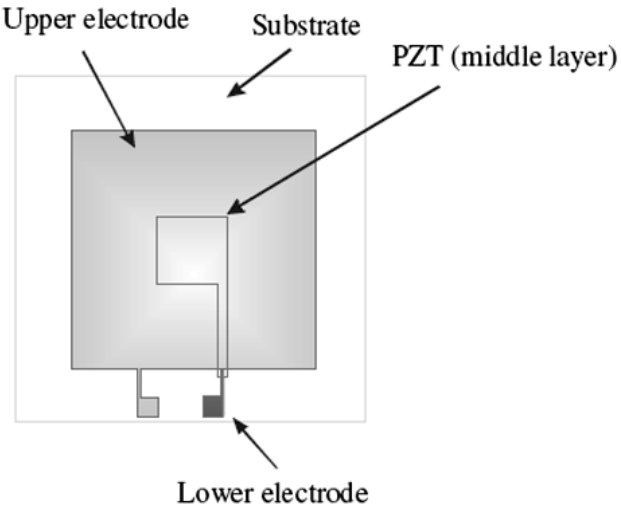

Figure 1-20: Layout of the sensor done by Dyakowski (2005)

Da Silva (2007) developed a novel needle probe to measure conductivity and capacitance to characterize dynamic multiphase fluid flows. A sinusoidal voltage is applied to the excitation electrode. By determining the complex value of current and knowing the supplied voltage, the admittance is calculated. The excitation frequency was set to be 200 kHz. To characterize the fluid the following equation is used.

$$Y = k_g(\kappa + j\varepsilon_0\varepsilon_r) \tag{1.8}$$

The geometry factor,k_g, is a function of length, distance and cross-sectional area of the sampled fluid. κ is the fluid electrical conductivity, ε_r is the relative permittivity of the fluid where ε_0 is the vacuum permittivity. Once the probe is calibrated for known fluids, k_g can be calculated and the probe can be utilized to characterize the fluids within the flow.

The manufactured probes with their dimensions are shown in Figure 1-21.

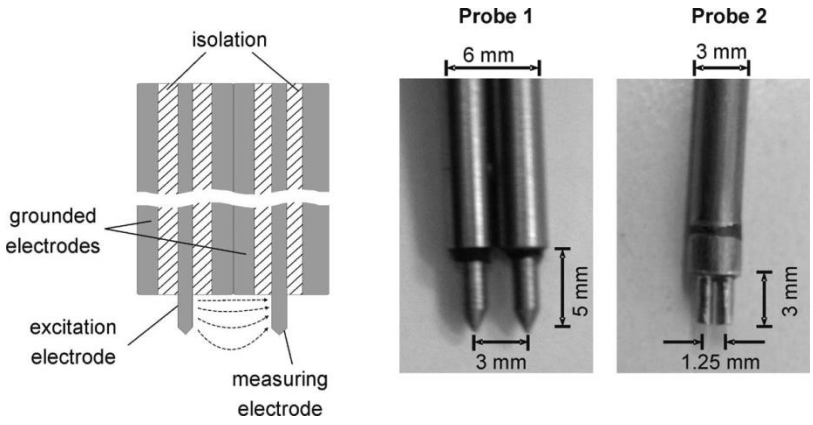

Figure 1-21: The schematic and two manufactured probes by Da Silva (2007).

Electrodes in probes 1 and 2 are stainless steel with diameters of 1 and 0.9 mm. The block diagram of the electronic circuitry is shown in Figure 1-22. A direct digital synthesizer (DDS) is used to generate the excitation voltage required for the electrodes. The digital signal is provided to DDS by A/D converter (12 bits, 20 000 samples/s/ch) of the USB data acquisition (DAQ) module PMD-1208FS (Measurement and Computing). The output voltage from trans-impedance amplifier is related to the measured admittance on the probe according to Eq. (1.9).

$$V_o = V_i . Y_M . \frac{1}{Y_f} \tag{1.9}$$

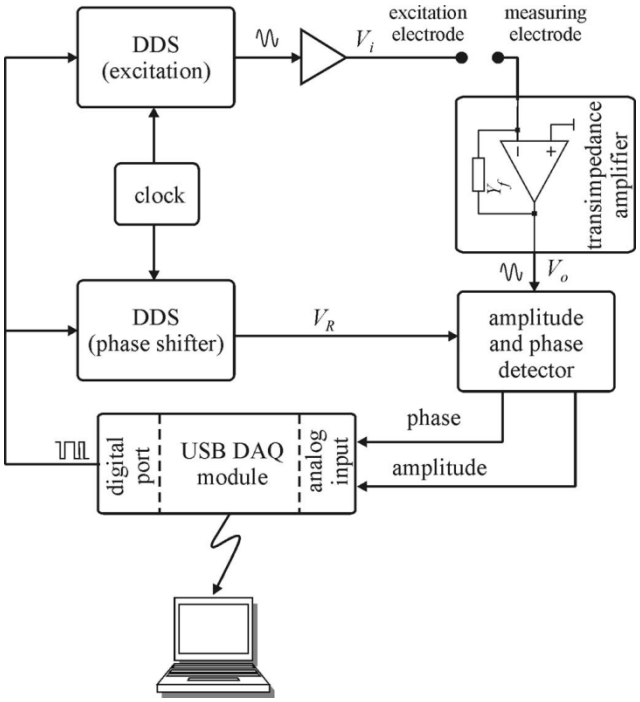

Figure 1-22: Block diagram of the electronic circuitry used by Da Silva (2007)

An amplitude and phase detector (IC AD8302, Analog Devices) is used to measure amplitude and phase of the signal. Since the phase detector operates in 90 degree with its best accuracy, a DDS phase shifter is utilized as a reference voltage with a 90 degree shift with respect to V_i to increase the accuracy of detecting small amount of phase shifts.

Schleicher (2008) introduced a novel type measuring dual modality needle probe which is able to measure conductivity accompanied by temperature in two phase flows. The necessity of measurement of temperature can be seen in steam-water two-phase

conditions. Their probe consists of a center electrode which is a 0.15 mm diameter direct sheath thermocouple and a second electrode which is a 0.8 mm diameter steel cannula. A 3 mm diameter steel tube is used as a ground electrode. Two ceramic tubes are placed between the electrodes to provide electrical insulation. The construction detail of the probe has been shown in Figure 1-23.

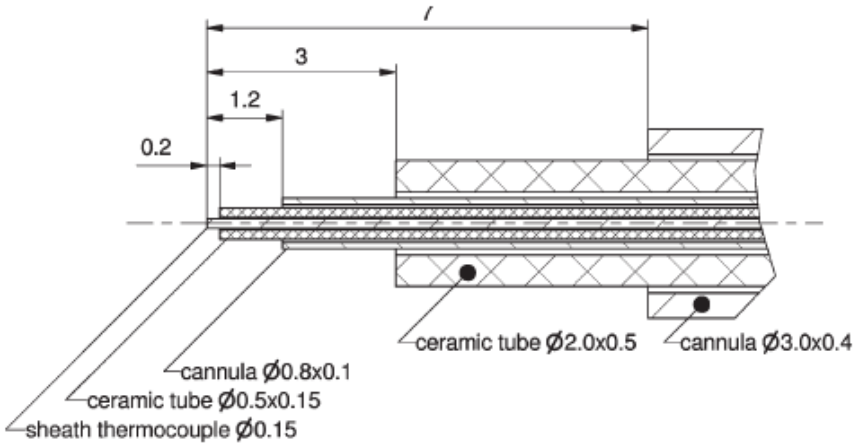

Figure 1-23: Layout of dual modality needle probe to measure local conductivity and temperature done by Schleicher (2008)

To measure the gas volume fraction, a 200 kHz sine wave is supplied to the measuring electrode. The signal obtained from the response of the probe is subtracted from the reference signal by a difference amplifier and by using a logarithmic amplifier the resulting amplitude of the signal can be detected.

In order to measure temperature, the low voltage signal generated by the thermocouple is amplified by a high gain and high common-mode rejection amplifier. Then a low pass filter with a cut-off frequency of 10 kHz is used.

The probe is designed for temperatures up to 300℃ and pressures up to 7 MPa.

1.3. Erosion Modeling

Recently, hydrodynamic modeling is being used to model the erosion process in pipe flows, bends and fluidized beds. According to the great influence of turbulence on erosion, studying the fluid flow and flow behavior near the solid walls is of the great importance. Erosion models generally are categorized into three groups (Lyczkowski and Bouillard (2002))

1. Single particle erosion models: In these models the influence of a single particle on a planar wall is considered. In these models the material can be removed in a purely ductile mode, purely brittle mode or the combination of both.

2. Dense phase erosion models: In these models, the repeated interaction of multiple solid particles is considered. The removal modes are considered to be ductile mode, brittle mode and low-cycle fatigue failure mode.

3. Power and energy dissipation models: In these models, energy transfer from solid particles to the solid surface is considered as the source of erosion.

Finnie (1960) studied the erosion resulting from a single particle. In the model, the author assumed that each particle acts like a machine tool on a ductile surface. In this model, the particle velocity (v) and impingement angle (α), which is the angle between velocity vector of the particle and the eroding surface, are the key parameters.

By using the above mentioned assumptions, the Finnie model is represented by,

$$Q = \frac{mv^2}{p\psi K}\left(sin2\alpha - \frac{6}{K}sin^2\alpha\right) \qquad \text{If } \tan\alpha \leq \frac{K}{6}$$
$$Q = \frac{mv^2}{p\psi K}\left(\frac{K}{6}cos^2\alpha\right) \qquad \text{If } \tan\alpha \geq \frac{K}{6} \tag{1.10}$$

Where Q is the volume of the eroded material, m is the particle mass; ψ is the depth of contact to the depth of the cut ($\psi = 1$), p is the flow stress and K is the ratio of the vertical to horizontal force (considered to be 2). Therefore, the volume of the eroded material is the function of kinetic energy of the particles interacting with the eroded surfaces according to the Finnie's model.

Considering *K=2,* when $\alpha \leq 18.43°$, while the particle is present near the solid surface the cutting process continues but when $\alpha > 18.43°$ the cutting process stops before the particle leaves the surface.

Bitter (1963) extended the erosion model developed by Finnie by introducing two concepts, threshold erosion rate and energy dissipation. In his model, a threshold impact velocity is considered in which below that no erosion can happen. The author combined the ductile and brittle erosion models and considered both the plastic and elastic behaviors. The wear curves according to his model for brittle and ductile materials are shown in Figure 1-24.

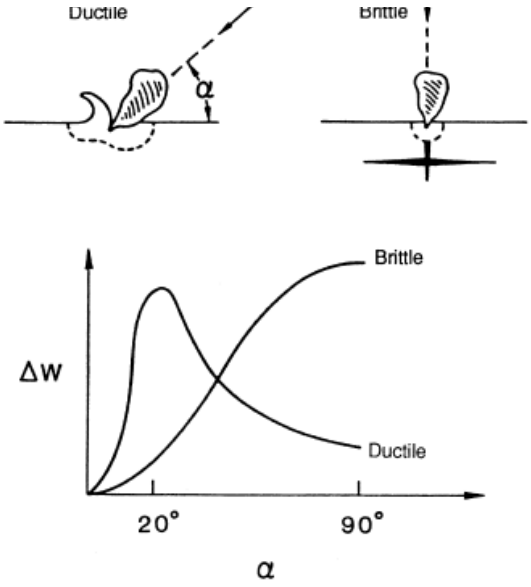

Figure 1-24: Erosion curves in brittle and ductile erosion mechanism for different impingement angles (Bitter (1963))

The deformation wear (W_d) which is caused by normal impinging velocity component (V_n) is considered to be fatigue damage from plastic deformation. The other form of erosion is the cutting erosion (W_c) which is caused by the tangential impingement velocity component (V_t) (Zhong and Minemura (1996))

$$W = W_c + W_d$$

$$W_d = \frac{0.5M_p(V_{ni} - K_1)^2}{\varepsilon_d}$$

$$W_c = \begin{cases} \dfrac{0.5M_pB(V_{ni} - K_1)^2\left\{V_{ti} - \dfrac{B(V_{ni}-K_1)^2\varepsilon_c}{\sqrt{V_{ni}}}\right\}}{\sqrt{V_{ni}}}, & \alpha < \alpha_0 \\ \dfrac{0.5M_p\{V_{ti}^2 - K_2(V_{ni} - K_1)^{1.5}\}}{\varepsilon_c}, & \alpha \geq \alpha_0 \end{cases} \quad (1.11)$$

The constant B, K_1 and K_2 are functions of materials properties. While ε_c and ε_d are the empirical erosion coefficients according to the Bitter's erosion model.

Ding and Gidasapow (1990) studied tube erosion process in fluidize beds. The authors developed a two-phase model to investigate the motion of sand particles and their influence on the erosion process. They used the kinetic theory of dense gases and assumed that the velocity distribution of sand particles follows the Boltzmann integral-differential equation (Eq.1.12).

$$\frac{\partial f}{\partial t} + u_i\frac{\partial f}{\partial x_i} + \frac{\partial}{\partial u_i}(F_i f) = (\frac{\partial f}{\partial t})_u \quad (1.12)$$

In Eq.1.12, f is defined in such a way that $f du$ is the differential number of sand particles that have the velocity within the range of u and $u + du$. $F$is defined to be the external force per unit mass exerting on each particle. In Eq.1.12, u is the instantaneous velocity of particles.

By modifying the thermal temperature present in kinetic theory of dense gases by granular temperature, the authors introduced two parameters which are solid viscosity and solid stress as the function of granular temperature. Granular temperature is defined as

$$\frac{3}{2}T = \frac{1}{2} < C^2 > \tag{1.13}$$

In Eq. 1.13, C is the fluctuating velocity of the particles.

The resulting solid bulk viscosity represented by,

$$\xi_s = \frac{4}{3}\epsilon_s \rho_p d_p g_0 (1+e)(\frac{T}{\pi})^{1/2} \tag{1.14}$$

And solid shear viscosity is obtained to be,

$$\mu_s = \frac{4}{5}\epsilon_s \rho_p d_p g_0 (1+e)(\frac{T}{\pi})^{1/2} \tag{1.15}$$

In above equations, e is the restitution factor and ϵ_s, ρ_p and d_p are sand concentration, particle density and particle diameter respectively. g_0 is given by Ogawa, Umemura et al. (1980) and defined as,

$$g_0 = \left[1 - (\frac{\epsilon_s}{\epsilon_{s_{max}}})^{1/3}\right]^{-1} \tag{1.16}$$

$\epsilon_{s_{max}}$ is the maximum amount of sand concentration that corresponds to the packing limit.

This model is the general form of the Navier-Stockes equation in order to consider the effects of sand particles. To obtain the solid viscosity and stresses the fluctuating energy equations are solved simultaneously.

Ding and Lyczkowski (1992)combined the Finnie's single particle model with the kinetic theory of the granular flow to model the erosion caused by repeated impact of sand particles to the targeted surface. It can be obtained by integrating Eq.1.10 over the range of particle and velocities using the parameter defined in Eq.1.12.

As the result, using the Maxwellian near wall velocity distribution, the erosion rate is obtained by,

$$\dot{E} = 2\epsilon_s \rho_p B_F \left[\frac{(2T)^{3/2}}{\sqrt{\pi}} F_1(\theta_c) + \frac{V_w^2}{2} \sqrt{\frac{2T}{\pi}} F_1(\theta_c) + \frac{3}{2} V_w T F_2(\theta_c) \right] \quad (1.17)$$

$if\ \theta_c = 71.57°$

$F_1(\theta_c) = 0.1$

$F_2(\theta_c) = 0.06$

In Eq.1.17, B_F is the function of Vickers hardness and V_w is solid phase near wall mean velocity.

In this model, erosion rate is the function of granular temperature, fluctuating kinetic energy, sand concentration and near wall particle velocity.

Cody, Goldfarb et al. (1996) performed experimental measurements of granular temperature as the function of velocity using novel non-intrusive vibration probes. The probes are used to measure the average kinetic energy by employing shot noise excitation of the vessel surface. They used this experimental data to check the consistency of the erosion measurements with granular temperature measurements.

1.3.1. Erosion Modeling in Pumps

Centrifugal pumps are often used to pump solid-fluid mixtures or slurry mixtures in high concentrations in different industries such as mining, pulp and paper industry. In some other cases, solid particles are present in the fluid mixture in low concentration during the extraction of oil or water. In these two above mentioned cases, erosion and hydrodynamic wear in different components of pump can occur and can cause severe damage to the pump. Therefore, studying the erosion and understanding the parameters affecting the wear is of great importance. Predicting the occurrence of wear in different components of the pump can lead to an optimum design of the pump with maximum durability and productivity.

Erosion in pumps has been studying by several investigators due to its complexity and various relevant parameters affecting it.

Zhong and Minemura (1996) investigated the wear in pump casing for wear-resistant materials. Applying Bitter's erosion model, the effects of particle impingement angle,

velocity, concentration and size were studied. Spinning of particles after collision to the wall make it possible to measure the particle impingement velocity.

Kruger et. al. (2010) studied the erosion of a radial centrifugal pump. The authors considered two main erosion processes which are shock-like and friction-like processes. In the friction-like process, solid particles are rubbing against the solid surface under pressure with low impingement angle and high near wall tangential velocity, on the other hand, shock-like process happens due to the particles with high normal velocity with a higher impingement angle. According to the authors, the key parameters affecting the pump erosion are,

- *Particle concentration*: Erosion rate and particle concentration are almost proportional. However, in high particle concentration, more interaction between particles results in less contact with the solid surface.

- *Impingement angle* : The maximum erosion rate for brittle materials happens when $\alpha = 90°$, for ductile materials it happens when $\alpha = 30°$ and for elastomers at $\alpha = 15°$

- *Particles size, hardness and shape*

- *Flow velocity:* Erosion rate is a power-law function of kinetic energy. The power coefficient varies from 0.9 to 5. The material is softening when the power is larger than 3 and is hardening for less than 3.

- *Turbulence:* Provides transport perpendicular to the flow direction. For the particles to reach the wall and pass through reduced Reynolds number of the boundary layer, adequate amount of turbulent kinetic energy is required.

- *Vortices and secondary flow*

The authors used the empirical models developed by Gülich (2008) and also CFD simulations (Euler-Euler approach) to predict the erosion in centrifugal pumps. CFD simulations performed on both non-eroded and eroded pump to understand the flow change due to the erosion in the pump. Using the flow results obtained from CFD, empirical quantitative erosion factor from the work done by Gulich (2008) used to predict the erosion rate in different parts of the pump. The erosion factor used is,

$$Erosion\ Factor = F_{KG}\left(\frac{C_{s,eq}}{C_{s,Ref}}\right)\left(\frac{w_{mix}}{w_{Ref}}\right)^{3} \tag{1.18}$$

where,

F_{KG}: Particles size factor,

C_s: Particle concentration

w_{mix}: Mixture velocity

w_{Ref}: Reference velocity ($10m/s$)

The comparison in erosion depth between simulation and experimental results along with the CFD results from the key parameters are shown in Figure 1-25.

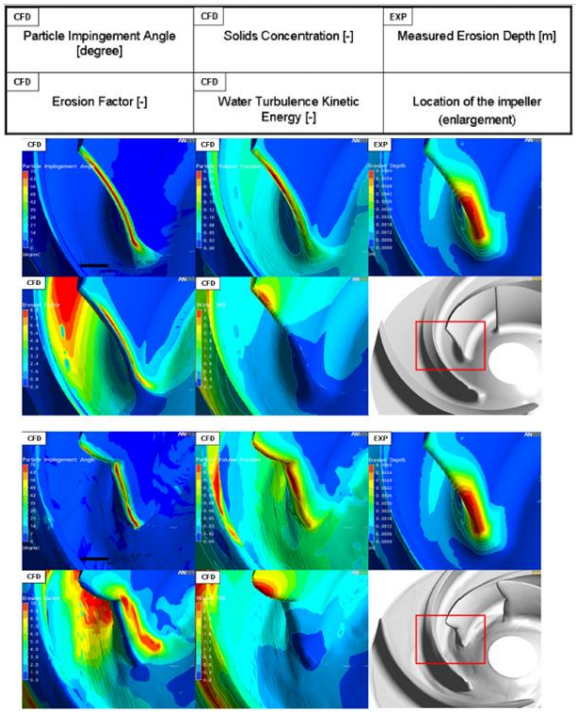

Figure 1-25: CFD results for non-eroded and eroded pump on leading edge of the blade for key erosion parameters and measured erosion depth (Kruger (2010))

2. OBJECTIVES

In this study, two ESP pumps manufactured by Baker Hughes Company are being studied, the MVP-ESP pump (G470) and the ESP-WJE1000.

Previous studies conducted on ESPs investigated the flow within the impeller, studying the bubble behavior and pressure rise in each single stage. In this work, stage by stage and overall performance of the MVP-ESP pump for different operating conditions is studied. Particularly, the flow behavior within the first and second stages of the pump diffuser is investigated.

One method to analyze the flow behavior is to use a high speed camera to visualize the flow. It includes bubble size measurement and flow pattern visualization. The bubble size at the inlet and outlet of two consecutive impellers are measured and their influence in different operating conditions on head degradation is studied.

To better understand the flow behavior within the stages of the pump, electrical resistance tomography (ERT) measurements are performed. Local gas concentration on the first stage and second stage diffusers is measured by using this instrument. Temporal and spatial average velocities of the components (air and water) through the diffuser are obtained by measuring the conductivity of the process fluid.

Pressure distribution through the pump along with first and second stage's diffuser pressure distribution are obtained for different pump operating conditions.

According to the acquired data from conductivity measurements, pressure measurements and high speed visualization, the relation between stage head degradation to effective parameters on the pump performance is developed.

To study the erosion process on the pump, CFD simulation on the first and second stages of ESP-WJE-1000 are performed. The key parameters affecting the erosion process on the main flow path of the pump including the balance holes are being considered. An empirical-numerical model to predict erosion rate on the centrifugal pumps in terms of the key parameters is introduced. The results are validated with the eroded surfaces of the ESP pump after being eroded after 175 hours of operation.

3. PROCEDURE*

3.1. Closed-Loop Flow Rig

The experimental closed loop two-phase facility at the Turbomachinery laboratory at Texas A&M University with all components is presented in this section. The facility is designed to provide two-phase flow conditions which are required to test two-phase pumps. In this experiment, water and air are used as the working fluid. Water which is extracted from the bottom of the separator tank is mixed with the extracted air from the top of separator tank. At the inlet of the pump a 6 inch water line and a 2 inch air line mix with each other in a 10 inch mixing chamber before entering the 8-inch diameter, 33 inch long, 3-stage MVP-ESP pump. Then, the flow is directed to the separator tank through a 6-inch outlet line. The separator tank uses centrifugal forces created in the tank to separate the gas and liquid.

The flow loop consists of three different circuits (Figure 3-1 and Figure 3-2). The primary loop, which is composed of three control valves, is employed to provide the required operating conditions of the pump. Control valves are used to vary the main operating conditions which are the water flow rate, pump inlet gas volume fraction (GVF) and pump inlet pressure. The secondary flow loop is used to cool the process fluid in the tank by

* Reprinted with permission from "Temporal Gas Volume Fraction and Bubble Velocity Measurement Using an Impedance Needle Probe" by Sahand Pirouzpanah and Gerald L Morrison, ASME 2013 Fluids Engineering Division Summer Meeting, Copyright 2013 by ASME.

means of an air cooled heat exchanger. A seal flush loop is used to supply the required amount of liquid for the mechanical seal installed on the pump input shaft.

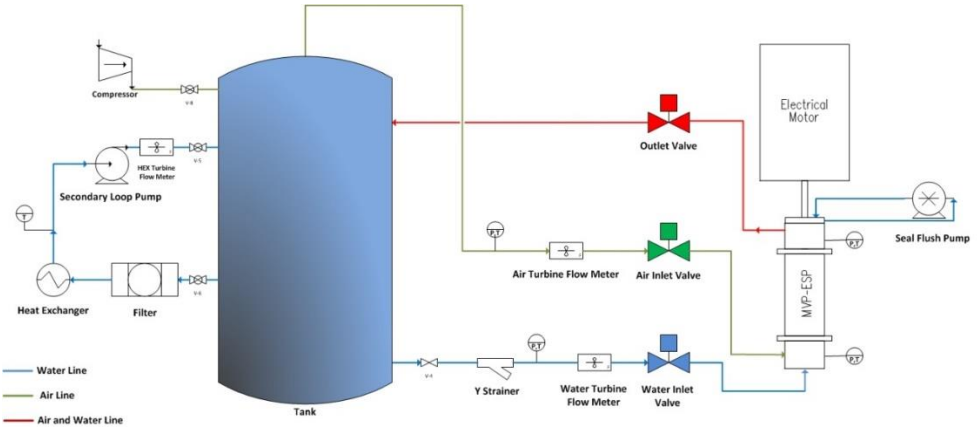

Figure 3-1: Schematic of the closed loop flow rig

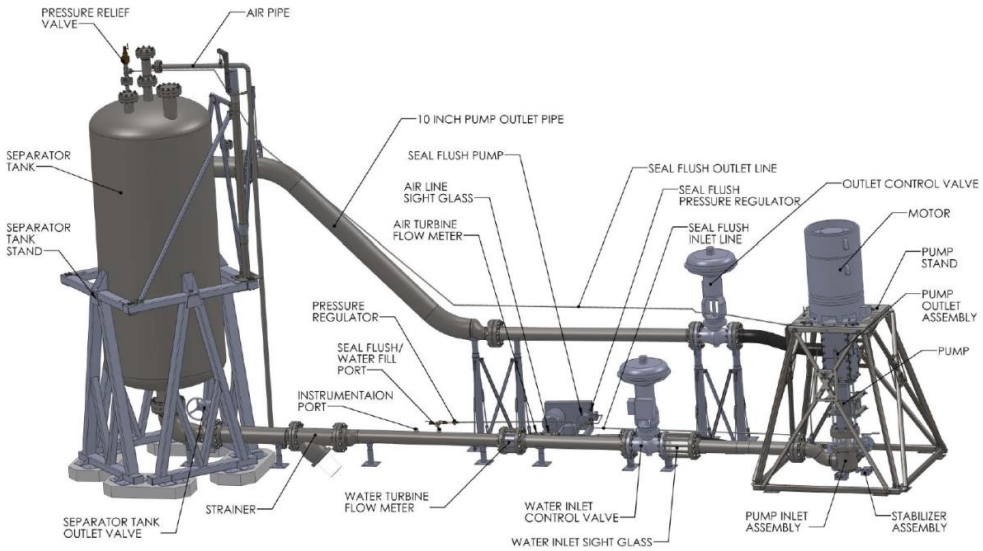

Figure 3-2: CAD drawing of the facility (Kirkland (2013))

The 304 stainless steel separator tank which has the capacity of 1760 gallon is rated for operating pressure of 450 psi (Figure 3-3). Since the mixture of water-air enters the separator tank tangentially, due to centrifugal forces, the two phases are separated from each other. A disk located at the bottom of the tank helps in the separation of air and water. As the result, the supplied air and water to the pump is free of entrained water and air respectively. To pressurize the entire close loop system and tank, a compressor is used in non-operating conditions. The compressor is disconnected when pump is in operation.

Figure 3-3: Separator Tank

The electrical motor used to rotate the pump is a 250 hp AC-60 Hz vertical motor. It is mounted above MVP-ESP and is manufactured by GE (Figure 3-4). A variable frequency drive (VFD), Yaskawa CIMR-P7U4160, is used to control the motor. The VFD allows the motor to run from 90 to 3600 RPM.

Air and water are supplied to the pump through two separate flow streams of air and water. Two pneumatically controlled valves (Figure 3-5) are located in these lines to control the operating conditions of the pump. The air and water valves are controlled via a Proportional/Integral (PI) controller available in the LabView program. The air valve is used to control the pump inlet pressure while the water valve is utilized to control the water flow rate. The GVF at the pump inlet is varied using a built-in PI LabView controller by varying the outlet control valve. When the pump is operated in single-phase conditions the outlet valve is used to set the pressure at the pump inlet.

Figure 3-4: 250 hp AC Motor

Figure 3-5: Control Valves, 1) Air control Valve, 2) Water control valve, 3) Outlet control valve

The front panel of the LabView program with the embedded controllers is shown in Figure 3-6.

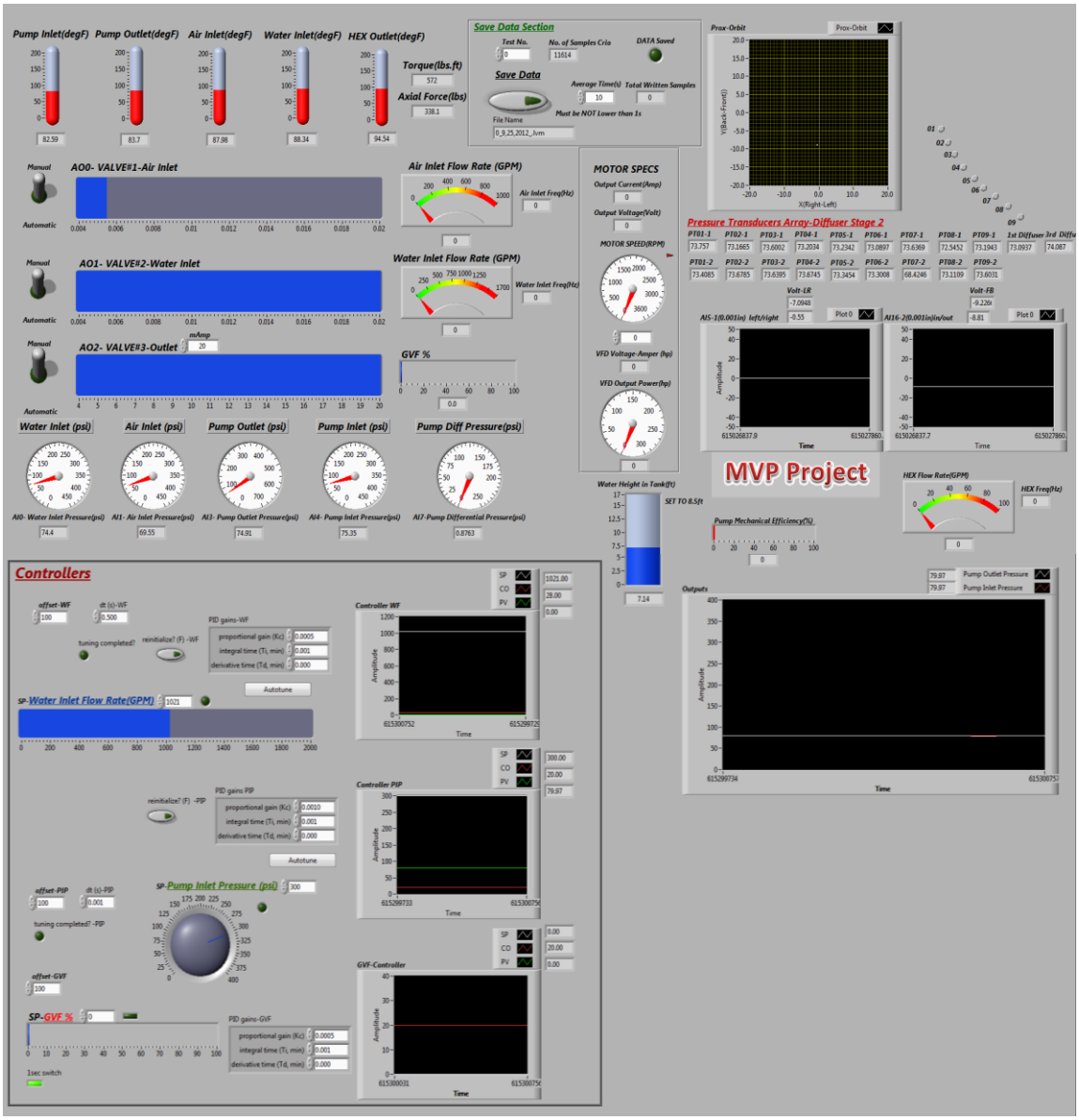

Figure 3-6: Front panel of LabView program to control and monitor the pump performance

The feedback required for the water control valve is provided by a liquid turbine flow meter (Figure 3-7), Turbine Incorporated WM0600X6, located in the water line according to Figure 3-1 (More information of liquid turbine flow meter in Appendix A). To measure

the amount of air supplied to the pump the air turbine flow meter FTB-938 from Omega Engineering (Figure 3-8) is employed (More information of air turbine flow meter in Appendix B). Frequency/Pulse signal conditioner obtains the frequency of the low level signal outputs from turbine flow meters magnetic pickups ($0\ \text{mV} - 120\ \text{mV}$) and converts them to the corresponding output voltage ($0\ \text{V} - 10\ \text{V}$). The output voltage is collected by the NI 9205 module installed in the NI CRIO-9074. By measuring the pressure and temperature at the location where the air turbine flow meter is located, the mass flow rate of air is calculated. Using the obtained air mass flow rate, the volumetric flow rate of air is calculated in any other locations within the system with a known pressure and temperature. By knowing the amount of air and water supplied to the pump, the gas volume fraction at the pump inlet is obtained.

Figure 3-7: Liquid turbine flow meter

Figure 3-8: Air turbine flow meter

3.1.1. Visualization Windows

Different windows have been placed in different parts of the flow path to visualize the flow. The window at the water inlet (Figure 3-9), right after water control valve, ensures that no air bubble enters the water line without being separated by the separator tank. The sight glass installed in the air line (Figure 3-10) is used to monitor and ensure no escaped water droplet enters the air line. This is important since any droplet of water can damage the air turbine flow meter located upstream of the sight glass. For the same purpose of visualization, two other windows (Figure 3-11 and Figure 3-12) have been placed at pump inlet and pump's 1st and 2nd stage diffusers. High speed visualization and conductivity measurements are also done throughout the window shown in Figure 3-12.

Figure 3-9: Water line sight glass

Figure 3-10: Air line sight glass

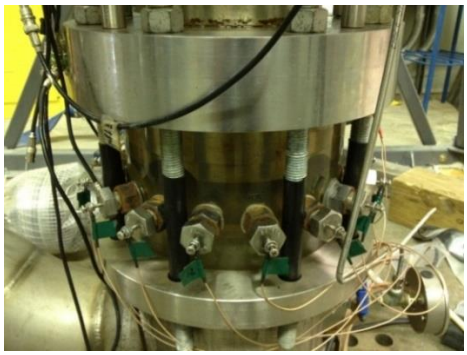

Figure 3-11: Pipe inlet window

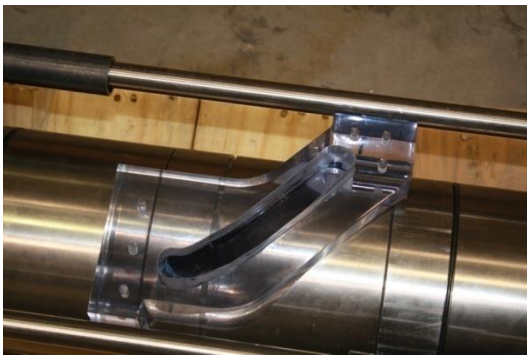

Figure 3-12: Window on the first and second stage of the pump

3.1.2. Instrumentation

3.1.2.1. Pressure Transducers

Two type of Omega Engineering's pressure transducers PX481A-500G5V and PX481A-1000G5V (output range: $1\ V - 5\ V$) are utilized to measure the pressure at the pump inlet and outlet respectively. Twenty Omega Engineering's pressure transducers, PX429-750GI and PX429-500GI (output range: $4\ mA - 20\ mA$), measure the pressure along the pump in different locations. NI-9205 collects the voltage output data from PX481A-500G5V and PX481A-1000G5V. The current output from PX429-750GI is converted to voltage by employing a resistor and the voltage is collected in NI-9205. The detail specification of the pressure transducers are given in Table 3-1.

Table 3-1: Pressure transducers specifications

Transducer	Max. Pressure (psig)	Output	Qt	Process Conn.	Accuracy	Total Err Band
PX481A-1000G5V	1000	1-5 Vdc	1	1/8 NPT	0.3% BFSL max. (includes linearity, hysteresis and repeatability)	1% FS
PX481A-500G5V	500	1-5 Vdc	1	1/8 NPT	0.3% BFSL max. (linearity, hysteresis and repeatability)	1% FS
PX429-750GI	750	4-20 mA	15	1/4 NPT	0.08% BSL max. (linearity, hysteresis and repeatability)	-
PX429-500GI	500	4-20 mA	5	1/4 NPT	0.08% BSL max. (linearity, hysteresis and repeatability)	-

3.1.2.2. Thermocouples

Temperature measurements are accomplished using T type thermocouples from Omega Engineering according to Table 3-2.

Table 3-2: Thermocouple specifications

Thermocouple Type	Max. Temp. Range (°F)	Limits of Error
T	-328 to 662	1.0°C or 0.75% Above 0°C

NI-9213 is used to acquire data from thermocouples.

3.1.3. Data Acquisition System (DAS)

The data acquisition system is composed of the components listed in Table 3-3. NI-CRIO-9074 chassis contains 8-slots into which modules NI-9205, NI-9265 and NI-9213 are installed. Frequency/Pulse Signal Conditioner Module, DRN-FP, is used to convert the frequency obtained from magnetic pickup of turbine flow meters to the voltage readable for NI-9205.

Table 3-3**:** Essential Components of Data Acquisition System

Chassis/Module	Model No.	Qt.	Description
Chassis	NI-CRIO-9074	1	8-Slot integrated 400 MHz real-time controller and 2M gate FPGA
Voltage Analogue Input Module	NI-9205	2	32 single-ended or 16 differential analog inputs ±200 mV, ±1, ±5, and ±10 V programmable input ranges, 16-Bit, 250 kS/s aggregate sampling rate
Current Analogue Output Module	NI-9265	1	4-Channel, 16-Bit, 0 to 20 mA output range, 100 kS/s, simultaneously updated
Thermocouple Input Module	NI-9213	1	16-Channel, 24-bit ADC for up to 0.02 °C measurement sensitivity, built-in CJC (cold-junction compensation)
Frequency/Pulse Signal Conditioner Module	DRN-FP	3	0.2 Hz to 50 kHz input range, low level signal input (magnetic pickups): 0 mV to 120 mV, AO 0-10 V, maximum current 10mA

3.2. Electrical Resistant Tomography (ERT)

Electrical resistant tomography is used to measure water and air distribution in the second stage diffuser of the MVP-ESP pump. The conductivity of the fluid is obtained in two-phase flow condition and is compared with the reference condition with single-phase water flow.

The conductivity measurements are performed by injecting current between two electrodes and measuring voltage difference between the rest of the electrodes. Then, the pair of injecting current electrodes is switched and voltage difference measurement is performed for the remaining electrodes. According to obtained results from voltage measurement for a known current injection, boundary conditions are defined for the reconstructing image schemes. All the process mentioned above is done in the electronic box and software provided by Industrial Tomography Systems Plc (its) shown in Figure 3-13.

Figure 3-13: Industrial Tomography Systems Plc (its) electronic box for conductivity measurements

17 brass electrodes (1 ground electrode and 16 measuring electrodes) were embedded on Stereolithography (SLA) window manufactured from WaterShed® XC 11122 (ABS-like) material. In the SLA method, epoxy based resins are cured by a UV laser layer-by-layer to grow a 3D object. The SolidWorks model and the manufactured part are shown in Figure 3-14. The brass electrode and its dimensions are shown in Figure 3-15. The window is sealed by an O-ring installed around the protruded part of the plastic window. To be able to connect to the ERT electronic box, wires were soldered to the brass electrodes and connected to ERT cable shown in Figure 3-16 (more information about ERT electrodes' design is in APPENDIX C).

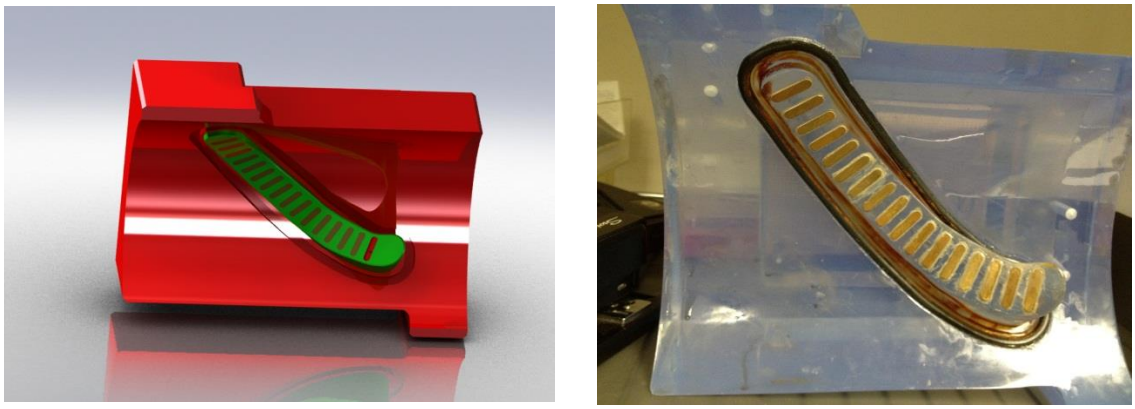

(a) (b)

Figure 3-14: Brass electrodes mounted on the window installed on the 2nd stage diffuser. (a) Solidworks model (b) Stereolithography (SLA) window manufactured from WaterShed® XC 11122 (ABS-like) material

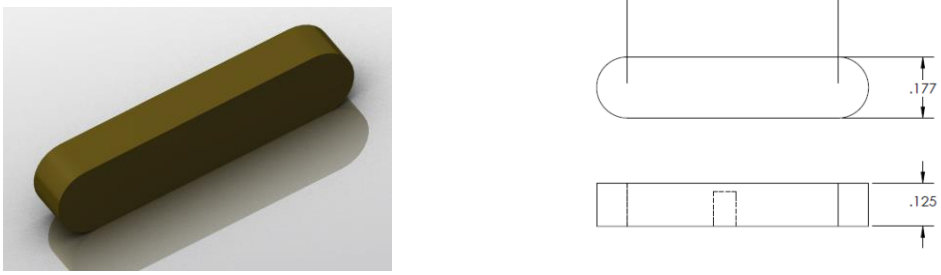

(a) (b)

Figure 3-15: (a) Brass electrode (b) Electrode dimensions

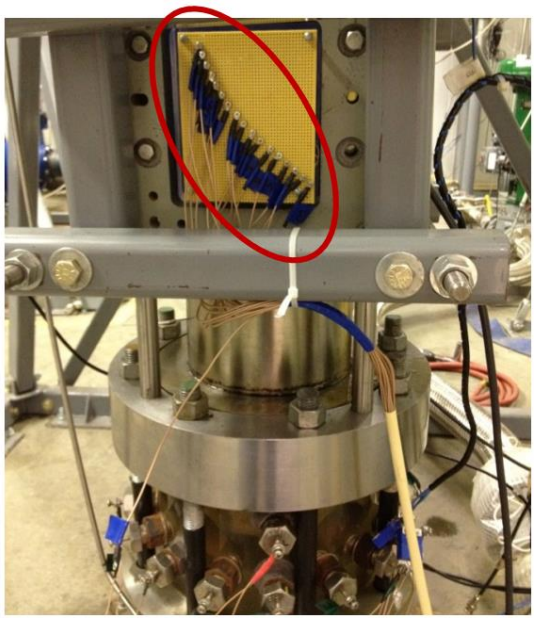

Figure 3-16: Installed and wired electrodes on the pump's 2nd stage diffuser

This arrangement allows the conductivity to be measured on the radial-axial plane along the meridional plane of the diffuser passage.

To utilize the electrodes and ERT system properly, there are some requirements that need to be considered.

1. The electrodes must be in direct contact with the process fluid

2. The primary fluid (in this case water) must be a conductive fluid to retain the conductivity between the electrodes

3. The electrodes must be installed on a non-conductive vessel. (In this application electrodes were assembled on an ABS-like window shown in Figure 3-14)

4. The surrounding conductive walls either should be grounded or insulated (Figure 3-17)

(a) (b)

Figure 3-17: Pump's 2nd stage diffuser (a) before applying insulator paint (b) after applying insulator paint on the non-rotating part of stage. Impellers have been electrically grounded

The resultant conductivity tomogram for the linear array is the $20\ \text{pixel} \times 10\ \text{pixel}$ rectangle that shows the average conductivity at each location in meridional plane of the diffuser stage. The depth of the measurement is the half of the electrode array length. The physical dimension of each pixel is 3/8" by 3/8". The "its" electronic box is capable of reaching injecting currents amplitude up to 75 mA and frequency up to 153600 Hz. The maximum sampling rate of 20 frames per second (fps) can be obtained. 104 individual measurement sets are used to reconstruct an average frame for a 16 electrode configuration.

One of the important parameters that can be obtained from tomography results is the concentration obtained from the Maxwell equation, which is calculated according to the following equation.

$$c = \frac{A_G}{A_G + A_L} = \frac{2\sigma_L - 2\sigma_{mc}}{\sigma_{mc} + 2\sigma_L} \tag{3.1}$$

Where

c (concentration) - Area fraction of the dispersed phase (gas) in each pixel,

$\sigma_L(mS/cm)$ - Conductivity of the continuous phase (liquid),

$\sigma_{mc}(mS/cm)$ - Measured conductivity,

$A_G(m^2)$ - Area occupied by gas in electrode location,

$A_L(m^2)$ - Area occupied by liquid in electrode location

3.2.1. Impedance Needle Probe

An impedance needle probe has been developed to measure local and temporal gas volume fraction through a conductive or non-conductive process fluid. Measuring both resistance and capacitance allows this probe to be functional in even non-conductive fluids. Two 1/32" insulated brass (alloy 260) rods with bare tips were placed intrusive to the flow. The gap between the electrodes is designed to be 0.085" (Figure 3-18). To provide the linear movement to the probe, a stepper motor has been connected to the tube which holds the

electrodes. Electrodes were mounted inside a Nylon rod which has been glued to the stainless steel tube.

A 100 kHz - 5 V (pk-pk) sinusoidal voltage is supplied to the electrodes. The measured voltage drop across the electrodes passes through a buffer and an amplifier. Then, the output AC signal goes to an amplitude detector (AD8307) which changes the input AC signal to DC with a proportional coefficient of 25 mV/dB. The output DC signal is filtered and the offset is removed using the circuit shown in Figure 3-19. A 4-Ch differential NI-9215 DAQ system with the maximum sampling rate of 100 kHz installed on NI-cRio-9074 chassis is utilized to capture and store the signal.

The probe can measure directional bubble velocity when a bubble passes through both electrodes. When bubble passes between electrodes the acquired signal varies. The duration of time, when the gradient of the obtained signal is non-zero, specifies the time when the bubble edge moves into the gap between two electrodes. For a known distance between electrodes and by the measured time, directional bubble velocity in the direction of the connecting line between electrodes can be measured. The ratio between the time intervals when signal is non-zero to the total time represents the temporal gas volume fraction.

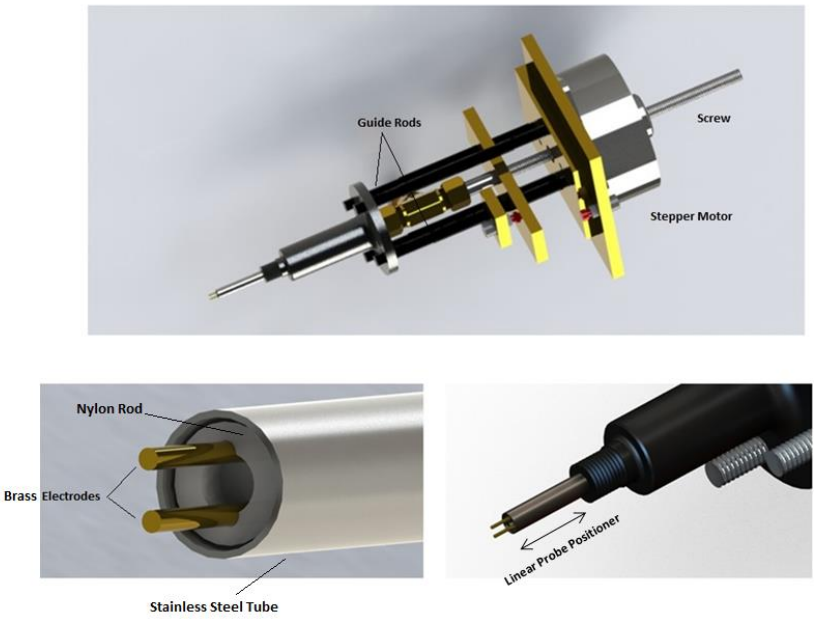

Figure 3-18: Impedance needle probe

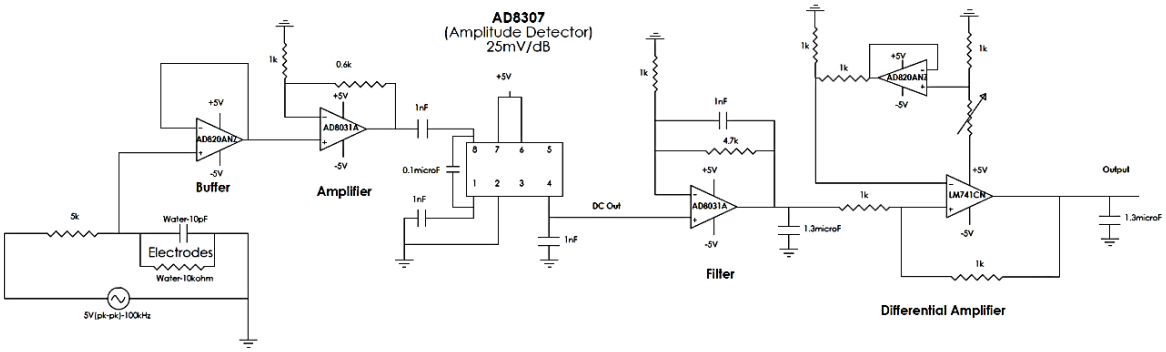

Figure 3-19: Circuit Diagram of the Impedance needle probe

The typical raw signal acquired from the circuit and its gradient are shown in Figure 3-20.

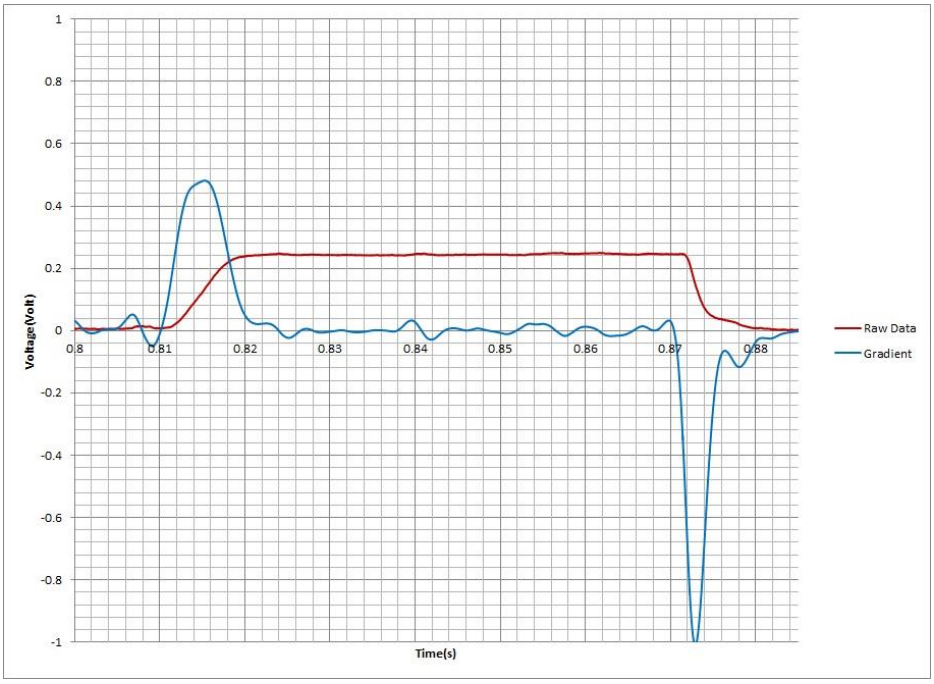

Figure 3-20: Captured signal when a bubble passes through the electrodes-Red line is the acquired signal-blue line is the gradient of the obtained signal

3.3. Pressure Distribution along Pump

To better investigate the performance of the pump in different operating conditions, pressure taps have been inserted in different locations of the pump. In Figure 3-21, the locations of pressure taps are shown. Twenty seven pressure taps have been inserted to measure the pressure distribution in pump's 2nd stage and in the meridional plane along first stage. On the suction side, meridonal plane and pressure side of the diffuser, 9 pressure taps in each line were drilled (Figure 3-21 and Figure 3-22). Pressure taps named as"PT08-2" in stage#2 and "PT-08-3" in stage#3 corresponds to each other according to their position. PT09, PT08-2 and PT07 are located on 2nd stage diffuser, right before the diffuser starts. PT01 is located just after the point where the diffuser ends. The

corresponding pressure taps at the inlet and outlet of the pump are shown by “PI” and “PO” respectively.

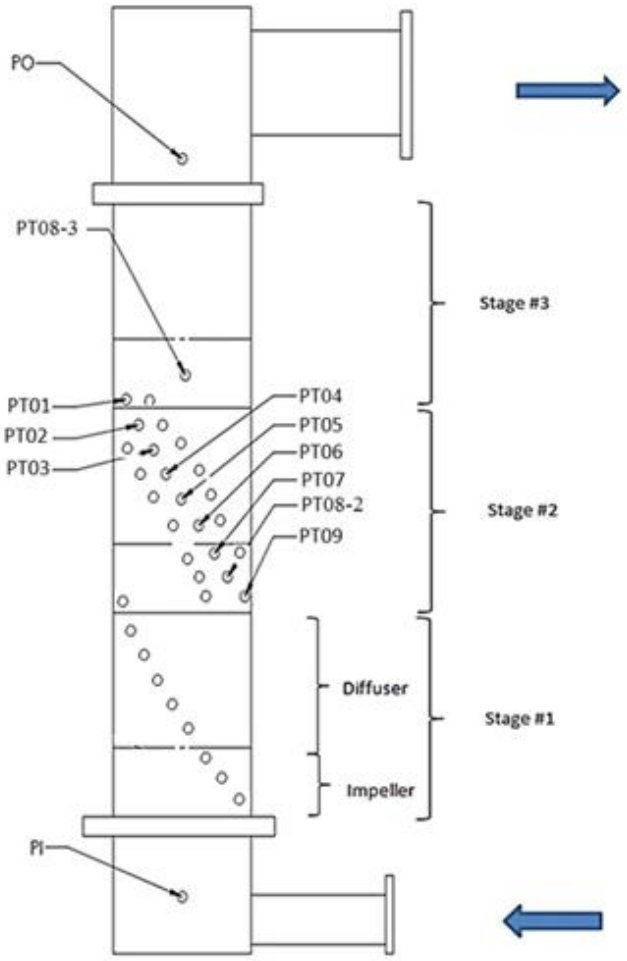

Figure 3-21: Pressure taps locations along the pump

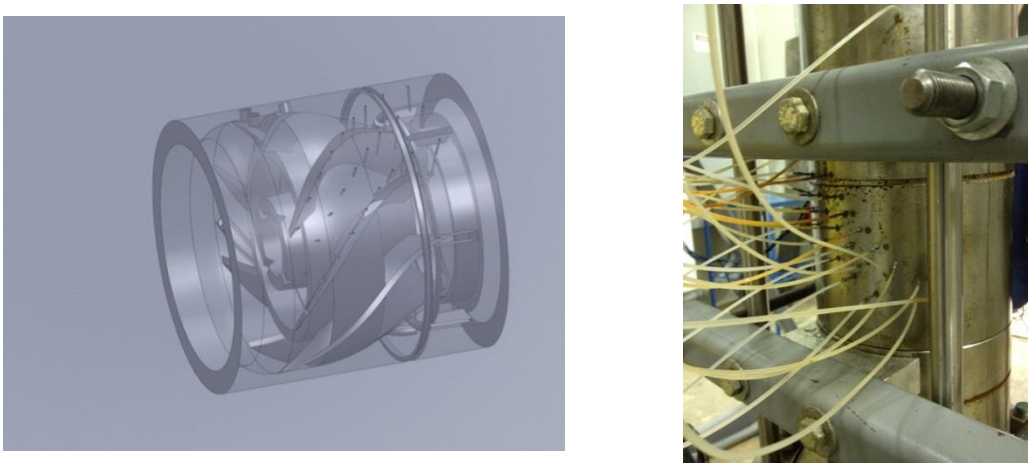

Figure 3-22: Location of the drilled pressure taps holes at second stage diffuser

3.4. High Speed Visualization

To measure the bubble size and bubble velocity a high speed camera (Phantom V711, Figure 3-23) is utilized. The specifications of the camera are summarized in Table 3-4.

Table 3-4: Phantom V711 specifications

Camera Type	Maximum Speed (fps)	Sensor size (mm × mm)	Maximum Resolution(pixels)
Phantom V711	1,400,000	25.6×16.0	1280×800

A continuous wave, 532 μm wavelength, green laser sheet with 1 watt power illuminates the process fluid.

Obtained images are analyzed in Insight 4G software to obtain the bubble size and bubble velocities.

Figure 3-23: Phantom V711 high speed camera

3.5. Test Matrix

The behavior of the pump is studied according to the test matrix shown in Table 3-5 for single-phase and two-phase flow conditions.

Table 3-5: Test Matrix

Speed (RPM)	Pump Inlet Pressure (psi)	Inlet Water Flow Rate GPM-(BPD)	Gas Volume Fraction (%)
3600	300	1459-(50,000)	0
3300	200	1313-(45,000)	5
3000	100	1167-(40,000)	10
		1021-(35,000)	15
		875-(30,000)	20
		729-(25,000)	25
		583-(20,000)	30
		437-(15,000)	35
			40
			45
			50
			55

For different configuration of the parameters mentioned in the table, pressure increment in the entire pump and 2nd stage diffuser were obtained.

3.6. Computational Analysis

Computational analysis was performed to study and model the erosion phenomena in an ESP pump, a WJE1000, manufactured by the Baker Hughes company. CFD analysis was carried out on the pump for the best efficiency point (BEP) which is the experimental testing operating condition used to experimentally study the erosion phenomena in this pump conducted in the Turbomachinery Laboratory at Texas A&M University. The experimental tests were performed for 129 hours on the ESP pump using Water-sand mixture with 2 $\mathrm{gr/lit}$ concentration and the average sand particle size of $150\mu\mathrm{m}$. The operating condition of the pump in its BEP occurs at the water flow rate of 331 $\mathrm{m^3/hr}$ for the rotating speed of 3600 RPM.

A single stage of the pump including impeller, diffuser and balance holes was meshed using Gambit 2.4.6. The entire geometry was meshed using 3D hexahedral elements to reduce the total number of elements (in comparison with 3D tetrahedral mesh), to eliminate the problems associated with skewness and increase the convergence rate. The boundary layer mesh was utilized to keep the y^*within its accepted limits to consider wall effects accurately. The 6.79 million node meshed model (Figure 3-24) was exported to ANSYS Fluent 13.0 as the CFD solver.

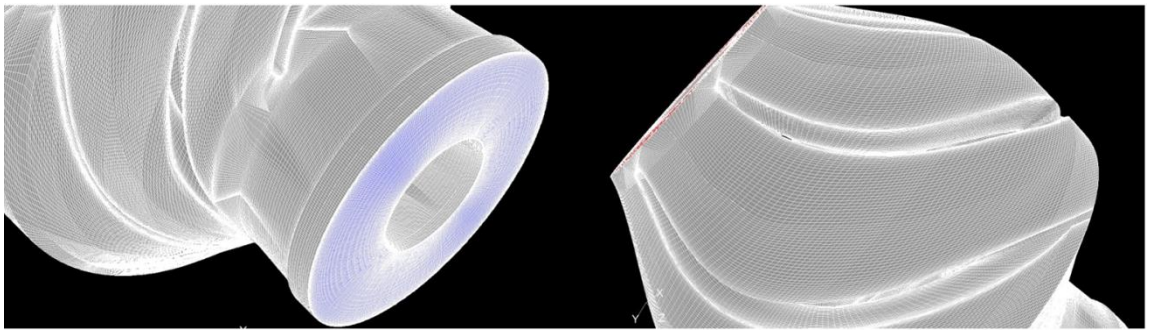

Figure 3-24: Mesh generated on single stage ESP

In Fluent software, to model the turbulence flow within the pump, the standard $k-\epsilon$ model has been utilized. This model is used to obtain the Reynolds stress term in the Reynolds Averaged Navier-Stokes Equation (RANS). The continuity and momentum equation in RANS equation are shown in Eqs. 3.2 and 3.3.

$$\frac{\partial \rho}{\partial t}+\frac{\partial}{\partial x_i}(\rho \bar{u}_i)=0 \tag{3.2}$$

$$\frac{\partial}{\partial t}(\rho \bar{u}_i)+\frac{\partial}{\partial x_j}(\bar{u}_i \bar{u}_j)=-\frac{\partial \bar{p}}{\partial x_i}+\frac{\partial}{\partial x_j}\left[\mu\left(\frac{\partial u_i}{\partial x_j}+\frac{\partial u_j}{\partial x_i}-\frac{2}{3}\delta_{ij}\frac{\partial \bar{u}_l}{\partial x_l}\right)\right]+\frac{\partial}{\partial x_j}(-\rho\overline{u_i' u_j'}) \tag{3.3}$$

The Reynolds stress term in the RANS equation, which is a function of fluctuating velocities, in $k-\epsilon$ model is obtained by following equation,

$$-\rho\overline{u_i' u_j'}=\mu_t\left(\frac{\partial u_i}{\partial x_j}+\frac{\partial u_j}{\partial x_i}\right)-\frac{2}{3}\left(\rho k+\mu_t\frac{\partial u_k}{\partial x_k}\right)\delta_{ij} \tag{3.4}$$

In Eq. 3.4, the turbulent viscosity (μ_t) is computed using k and ϵ to be,

$$\mu_t = \rho C_\mu \frac{k^2}{\varepsilon} \tag{3.5}$$

Transport equation to obtain turbulent kinetic energy *k* is given by,

$$\frac{\partial}{\partial t}(\rho k) + \frac{\partial}{\partial x_i}(\rho k u_i) = \frac{\partial}{\partial x_j}\left[\left(\mu + \frac{\mu_t}{\sigma_k}\right)\frac{\partial k}{\partial x_j}\right] + P_k + P_b - \rho\varepsilon - Y_M + S_k \tag{3.6}$$

And for ϵ is given by,

$$\frac{\partial}{\partial t}(\rho \varepsilon) + \frac{\partial}{\partial x_i}(\rho \varepsilon u_i) = \frac{\partial}{\partial x_j}\left[\left(\mu + \frac{\mu_t}{\sigma_\varepsilon}\right)\frac{\partial \varepsilon}{\partial x_j}\right] + C_{1\varepsilon}\frac{\varepsilon}{k}(P_k + C_{3\varepsilon}P_b) - C_{2\varepsilon}\rho\frac{\varepsilon^2}{k} + S_\varepsilon \tag{3.7}$$

Where, P_k, the production of kinetic energy as the result of mean flow velocity is calculated by,

$$P_k = \mu_t S^2 \tag{3.8}$$

In Eq. 3.8, *S* is the mean rate of stress tensor and is computed by,

$$S = \sqrt{2 S_{ij} S_{ij}} \tag{3.9}$$

P_b, which is the production of kinetic energy due to buoyancy is the function of temperature gradient ($\frac{\partial T}{\partial x_i}$)and is defined as,

$$P_b = \beta g_i \frac{\mu_t}{P_{rt}}\frac{\partial T}{\partial x_i} \tag{3.10}$$

In Eq. 3.10, P_{rt} is the Prandtl number for energy, and g_i is the gravity, and β is the coefficient of thermal expansion and is given by,

$$\beta = -\frac{1}{\rho}\left(\frac{\partial \rho}{\partial T}\right)_p \tag{3.11}$$

Y_M, shows the influence of fluctuating dilatation in compressible turbulence on the total dissipation rate and S_E, S_K are the user defined source terms.

The model constants are given as follows as default values,

$$C_{1\varepsilon} = 1.44 \tag{3.12}$$

$$C_{2\varepsilon} = 1.92 \tag{3.13}$$

$$C_{\mu} = 0.09 \tag{3.14}$$

$$\sigma_k = 1.0 \tag{3.15}$$

$$\sigma_{\varepsilon} = 1.3 \tag{3.16}$$

To consider the wall effects, boundary mesh is utilized. According to the law-of-the-wall for mean velocity U^* (dimensionless velocity) is defined as,

$$U^* = \frac{1}{\kappa}\ln(Ey^*) \equiv \frac{U_p C_\mu^{1/4} K_p^{1/2}}{\tau_\omega/\rho} \tag{3.17}$$

The logarithmic law is valid for 30 <y^*< 300, where the constant are considered as $\kappa = 0.4187$ and $E = 9.793$

And dimensionless distance from wall (y^*) is computed by,

$$y^* = \frac{\rho C_\mu^{1/4} k_p^{1/2} y_p}{\mu} \tag{3.18}$$

3.6.1. Erosion Modeling

The WJE-1000 ESP pump consists of a five-blade impeller and a seven-blade diffuser (Figure 3-25). Five balance holes are located on the impeller hub close to the suction side of impeller blades (Figure 3-26) to decrease the axial force exerted on the pump. This pump, which is also a mixed flow pump, has a continuous impeller blade rather than the split blade in MVP pumps. Therefore, these regular ESP pumps are not able to handle as high gas volume fraction as multi-vane pumps (MVP).

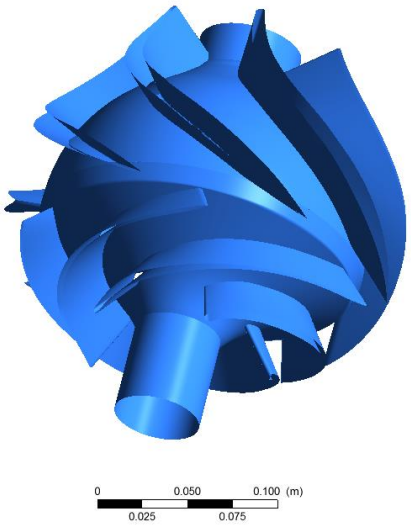

Figure 3-25: Single Stage blades and hub of ESP pump

Figure 3-26: ESP impeller and balance holes

The erosion phenomena in the main flow path of the pump including the flow injected from balance holes is considered. CFD simulations were performed by dividing the fluid domain into four regions,

- Impeller
- Diffuser
- Inlet
- Balance holes

Transient analysis was performed to simulate the flow within the pump accurately. Moving mesh was considered for impeller and balance hole fluid domains while the rest were held stationary. Two-phase flow simulation was carried out on the pump using water-sand mixture as the working fluid.

Since, the leakage flow through the secondary flow path (the backflow through seals and the clearance between the impeller and casing) was not included in this study, to consider the effects of the balance holes on the flow field and erosion specifically in the impeller section, leakage flow was calculated and the estimated calculated value was included in the simulation.

To estimate the amount of leakage flow, using the experimentally obtained pressure rise across each stage and assuming a discharge coefficient of 0.6, the mass flow rate injecting to the main flow path from the secondary flow path was approximated. The leakage mass flow rate was estimated to be 5% of the total inlet mass flow rate. The effect of the additional mass flow rate due to the balance holes located at the first stage was excluded from the outlet profile of first stage. Therefore, in the simulation, both stages have the

same amount of mass flow rate passing through. This outlet profile was obtained by using the simulation results where the balance holes were removed from the simulation.

First stage and second stage of the pump were simulated separately due to the difference at the boundary condition at the stage inlet. The flow at the inlet of the first stage was considered to be homogenous while on the second stage, a non-zero velocity and sand concentration gradient were present. The flow condition exiting from the first stage was considered as the boundary condition at the inlet of the second stage.

The first stage and second stage of the pump were simulated separately because of the difference at the boundary condition at the stage inlet due to the additional mass flow rate through the balance holes. Also, according to the simulation results obtained by Rasmy Marsis (2012) on an ESP pump, the difference between CFD simulation results in stage-by-stage basis and entire pump basis were negligible. Therefore, unsteadiness caused by the interaction of stages can be neglected in these types of pumps. This is expected due to the relatively long distance between the diffuser of the first stage and impeller of the second stage.

In the first stage, as the inlet boundary condition, total mass flow rate with homogenous sand concentration was assigned while for the second stage, entire flow properties from

the first stage outlet condition was employed for the inlet of the second stage. The outlet boundary condition for both cases was assigned to be a constant pressure.

To simulate two-phase flow, Eulerian-Granular model in ANSYS-FLUENT was employed. The model solves the momentum and continuity equation for each phase considering the common pressure between two phases. The coupling between phases is obtained from pressure and interphase exchange coefficient. The required properties are modeled from application of kinetic theory. This model, allows the phases to be separate and still be in interaction with each other in contrast to the Eulerian-Lagrangian approach that is used in discrete phase model (DPM).

For the Eulerian model, the continuity equation for each phase p &q is given by,

$$\frac{1}{\rho_{rq}}\left(\frac{\partial}{\partial t}\left(a_q\rho_q\right) + \nabla.\left(a_q\rho_q\bar{v}_q\right) = \sum_{p=1}^{n}(\dot{m}_{pq} - \dot{m}_{qp})\right) \quad (3.19)$$

Where ρ_{rq} is the reference phase density or averaged phase density of q^{th}phase

The volume fraction V_q of phase q is given by:

$$V_q = \int_V \alpha_q \, dV \quad (3.20)$$

Where α_q is the phasic volumetric void fraction as $\sum_{q=1}^{n}\left(\alpha_q\right) = 1$

Hence, the effective density of the phase q is:

$$\hat{\rho}_q = a_q \rho_q \tag{3.21}$$

The conservation of momentum for the fluid phase q is,

$$\begin{aligned} &\frac{\partial}{\partial t}(a_q \rho_q \underline{v}_q) + \nabla.(a_q \rho_q \underline{v}_q \underline{v}_q) \\ &\qquad = -a_q \nabla p + \nabla.\underline{\tau}_q + a_q \rho_q \vec{g} \\ &\qquad + \sum_{p=1}^{n} (K_{pq}(V_p - V_q) + \dot{m}_{pq} \underline{v}_{pq} - \dot{m}_{qp} \underline{v}_{qp}) + (\vec{F}_q + \vec{F}_{lift,q} + \vec{F}_{vm,q}) \end{aligned} \tag{3.22}$$

The Fluid-Solid conservation of momentum for the solid phase s is given by:

$$\frac{\partial}{\partial t}(a_s \rho_s \underline{v}_s) + \nabla.(a_s \rho_s \underline{v}_s \underline{v}_s) = -a_s \nabla p + \nabla p_s + \nabla.\underline{\tau}_s + a_s \rho_s \vec{g} + \sum_{l=1}^{n} (K_{ls}(V_l - V_s) + \dot{m}_{ls} \underline{v}_{ls} - \dot{m}_{sl} \underline{v}_{sl}) + (\vec{F}_s + \vec{F}_{lift,s} + \vec{F}_{vm,s}) \tag{3.23}$$

Where p_s is solid pressure andF is the force vector, and $\bar{\tau}$ is the stress-strain tensor.

The exchange coefficient between the two phases is given by K_{pq} or as K_{ls} follows:

$$K_{pq} = \frac{a_q a_p \rho_p f}{\tau_p} \tag{3.24}$$

Where f is the drag function that includes the drag coefficient, and τ_p is the particulate relaxation time and is given by the following equation:

$$\tau_p = \frac{\rho_p d_p^2}{18\mu_q} \tag{3.25}$$

And d_p is the bubble diameter.

To quantitatively predict the erosion rate in different locations in the pump, a 3D scan of the non-eroded impeller and eroded impeller has been done. Subtraction of the results represents quantitative erosion depth after 185 hours of pump operation. By correlating the obtained results from CFD simulation and results of 3D scan allows introducing a new model to predict the erosion phenomena in pumps.

4. RESULTS AND DISCUSSION*

4.1. Entire MVP-ESP-G470 Performance Data

The performance of the three-stage MVP-ESP-G470 pump was investigated for different inlet gas volume fractions and different water flow rates (Figure 4-1). By increasing inlet GVF, the pressure rise across the pump decreases (Figure 4-1(a)). Introducing air into the pump decreases the density of the mixture, increases the total volumetric flow rate and creates interphasic forces resulted from relative motion of gas phase with respect to the liquid phase. All these factors cause pump pressure rise reduction due to additional air.

* Reprinted with permission from "Performance Evaluation of a Multiphase Electric Submersible Pump" by Gerald L. Morrison, Sahand Pirouzpanah, Lisset J. Barrios, Klayton Kirkland, and Stuart L. Scott, In Offshore Technology Conference 2014, Copyright 2014 by OTC.

Reprinted with permission from "Flow Characterization in an ESP pump Using Conductivity Measurements" by Sahand Pirouzpanah, Sujan Reddy Gudigopuram and Gerald L Morrison, ASME 2014 Fluids Engineering Division Summer Meeting, Copyright 2014 by ASME.

Reprinted with permission from "Predictive Erosion Modeling in an ESP Pump" by Sahand Pirouzpanah and Gerald L Morrison, ASME 2014 Fluids Engineering Division Summer Meeting, Copyright 2014 by ASME.

In Figure 4-1(b), the power supplied by VFD is shown. Due to the reduction of pressure rise across the pump, the input power required for the pump decreases. The hydraulic power in two-phase condition is computed by using Eq. (4.1). A portion of the power is imparted to the liquid phase and the other portion is imparted to the gas phase to compress the fluid. In Eq. (4.1), the compression process is assumed to be isothermal. This assumption is true for lower gas volume fractions.

$$P_{h,2ph} = Q_L(p_{out} - p_{in}) + Q_g p_{in} ln(p_{out}/p_{in}) \quad (4.1)$$

According to Figure 4-1(c), pump mechanical efficiency, η, decreases by increasing inlet gas volume fraction. The mechanical efficiency is calculated using the following equation.

$$\eta = P_{h,2ph}/P_{in} \quad (4.2)$$

Due to the pump head degradation by the additional air, the efficiency of the pump reduces and BEP shifts to the lower water flow rates.

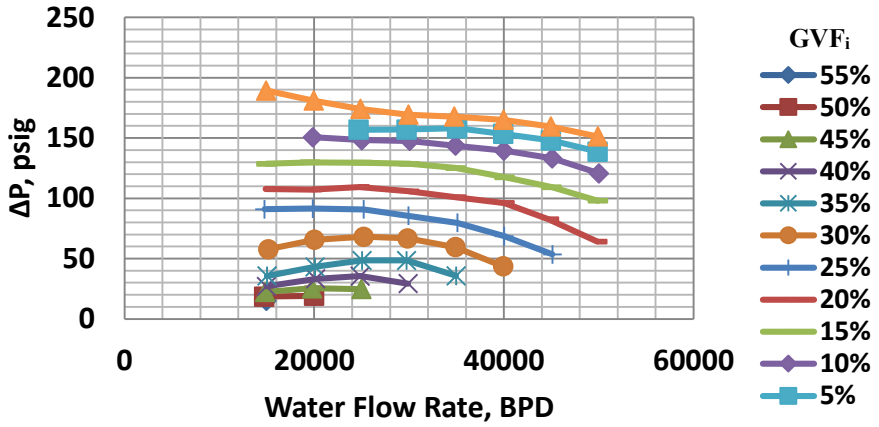

(a)

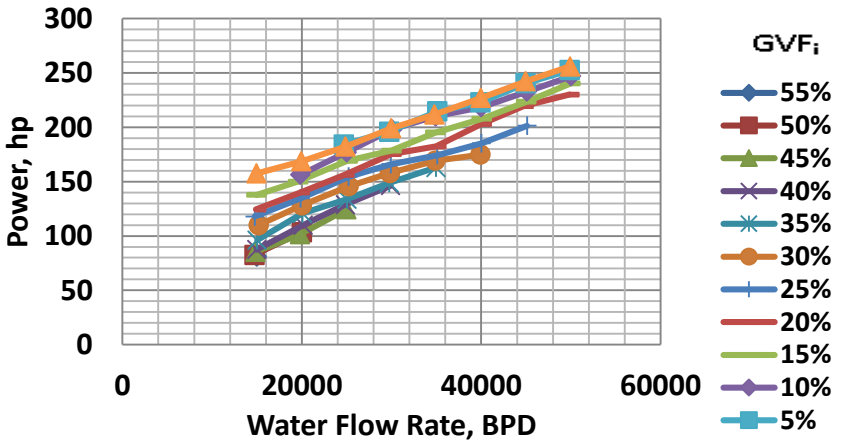

(b)

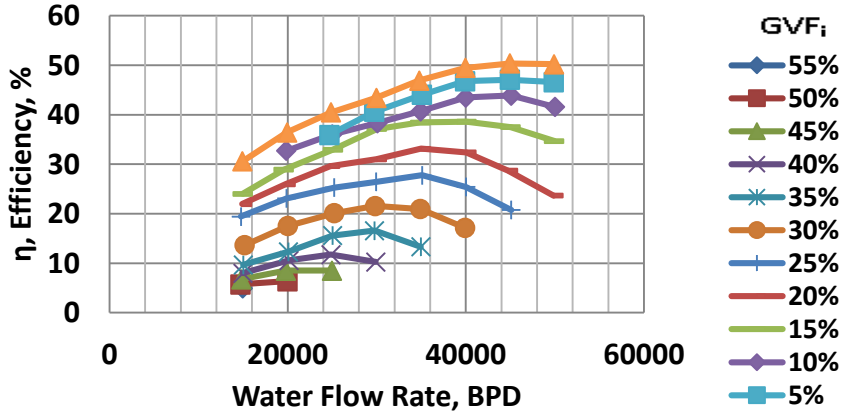

(c)

Figure 4-1: Entire MVP-ESP-G470 performance data (a) pressure rise, (b) pump input power, and (c) mechanical efficiency - rotating speed is 3600 RPM and pump inlet pressure is 300 psig

4.1.1. Rotating Speed Effects on Entire Pump Performance

According to the affinity laws for a homogenous flow in pumps, Equations (4.3) - (4.5), by increasing the rotating speed, pressure rise across the pump increases. Although, due to head degradation in pumps in two-phase and heterogonous conditions, pump performance does not exactly follow the affinity laws but it is fairly a good approximation in determining the general trend of the pump performance.

$$\Pi_1 = \frac{Q}{ND^3} \tag{4.3}$$

$$\Pi_2 = \frac{P_{in}}{\rho_{mix} N^3 D^5} \tag{4.4}$$

$$\Pi_3 = \frac{\Delta p}{\rho_{mix} N^2 D^2} \tag{4.5}$$

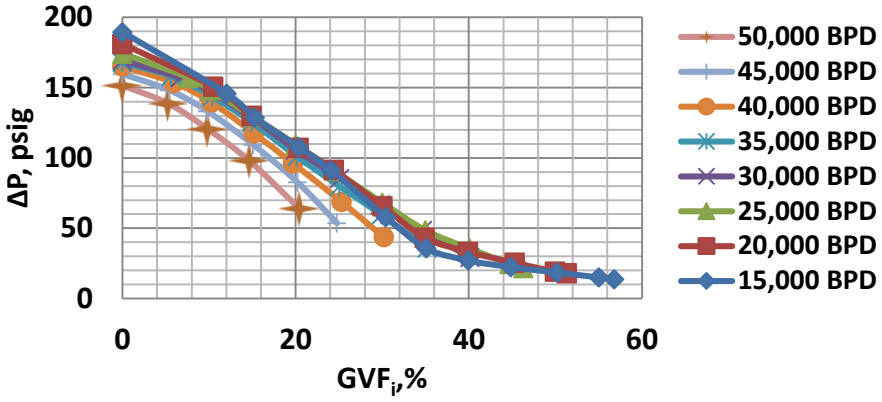

(a)

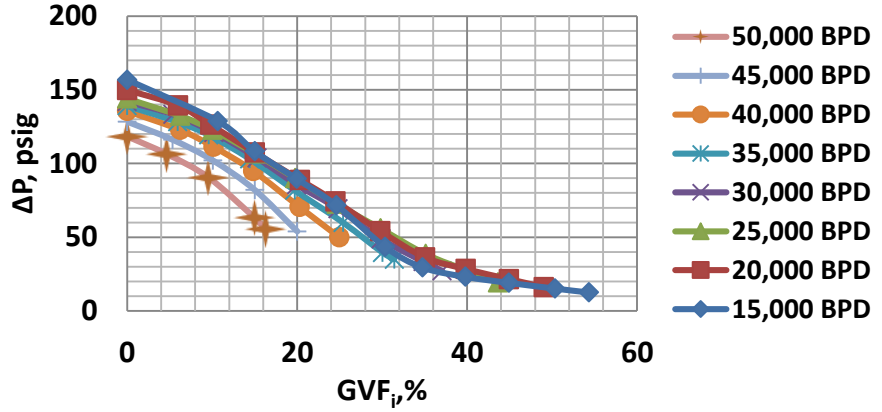

(b)

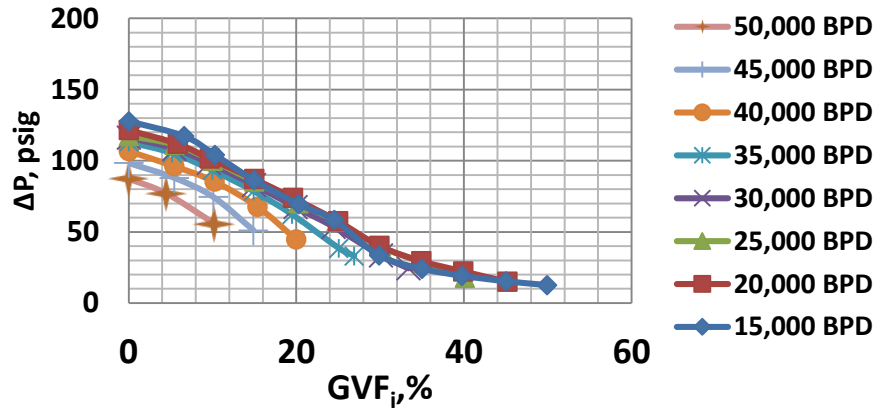

(c)

Figure 4-2: Rotating speed effects on the MVP-ESP pump performance (a) 3600 RPM, (b) 3300 RPM, and (c) 3000 RPM at 300 psig inlet pressure for different water flow rates

An increase in the rotating speed of the impeller causes the bigger bubbles to get chopped off and also, due to the increase in the pressure rise, the bubbles get compressed. Therefore, increasing the rotating speed increases the gas handling capacity of the pump and as the consequence, pump can reach higher inlet gas volume fractions (Figure 4-2 (a-c)).

Increasing the rotating speed increases the inertial forces at the exit of the impeller. As the result, two phases get separated from each other and it leads to the head degradation in the pump. Due to the head degradation, affinity laws overestimate the pump performance.

4.1.2. Inlet Pressure Effects on Entire Pump Performance

By increasing the pump inlet pressure, density of the mixture increases. According to affinity laws modified for the homogenous model, the density increase leads into the higher pressure rise across the pump. Also, due to the higher pressure at the pump inlet, bubble size is smaller and compressibility of the gas phase at each stage decreases. Increasing the pump inlet pressure improves the gas handling capacity of the pump and the pump can reach higher inlet GVFs (Figure 4-3 (a-c)).

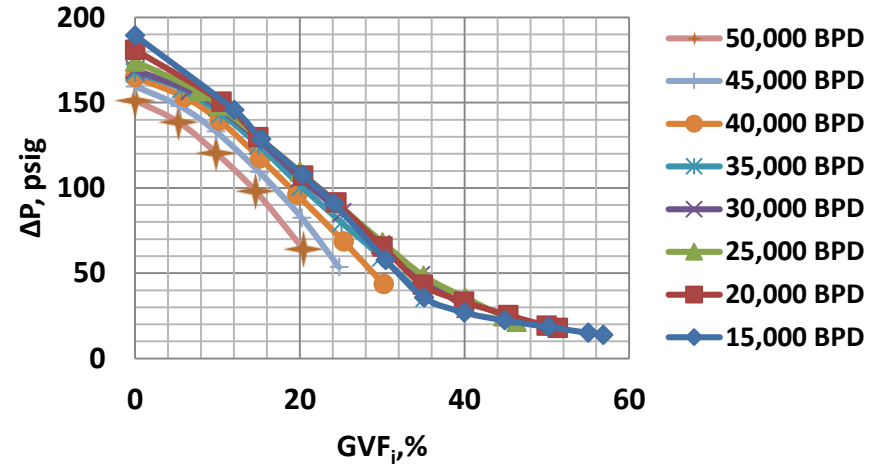

(a)

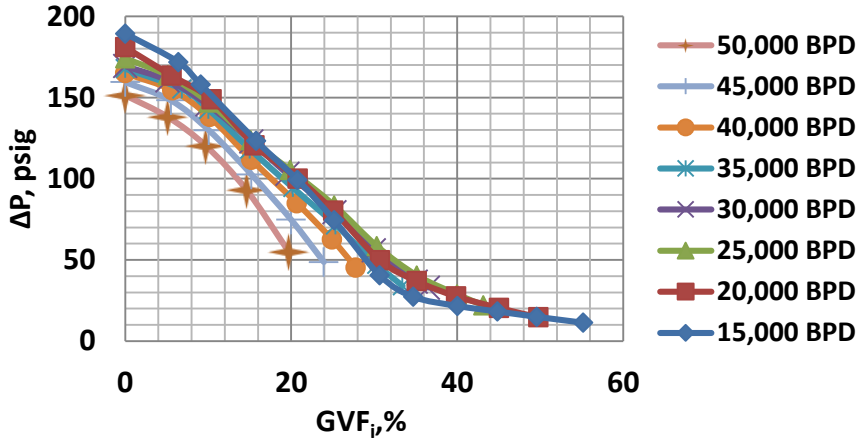

(b)

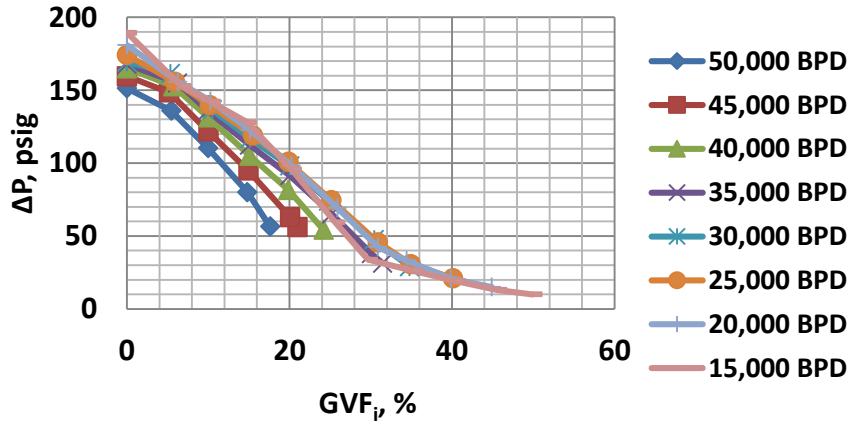

(c)

Figure 4-3: Pump inlet pressure effects on the pump pressure rise (a) 300 psig, (b) 200 psig, and (c) 100 psig at 3600 RPM for different water flow rates

High inlet pressure has more influence on the pressure rise at higher gas volume fractions than lower gas volume fractions. As the inlet pressure increases, the pressure rise in lower gas volume fractions becomes almost independent of the inlet pressure.

The head generated by the 3-stage MVP pump for different inlet pressures, total inlet flow rates and inlet mixture densities in different rotating speeds is shown in Figure 4-4 which is representation of the results discussed in Figure 4-2 and Figure 4-3 in 3D plots. According to Figure 4-4, by increasing the inlet pressure and rotating speed the head generated in the pump increases. The effects of the rotating speed are more dominant than the effects of the inlet pressure. Also, by increasing the inlet pressure and rotating speed, the operating envelope of the pump extends.

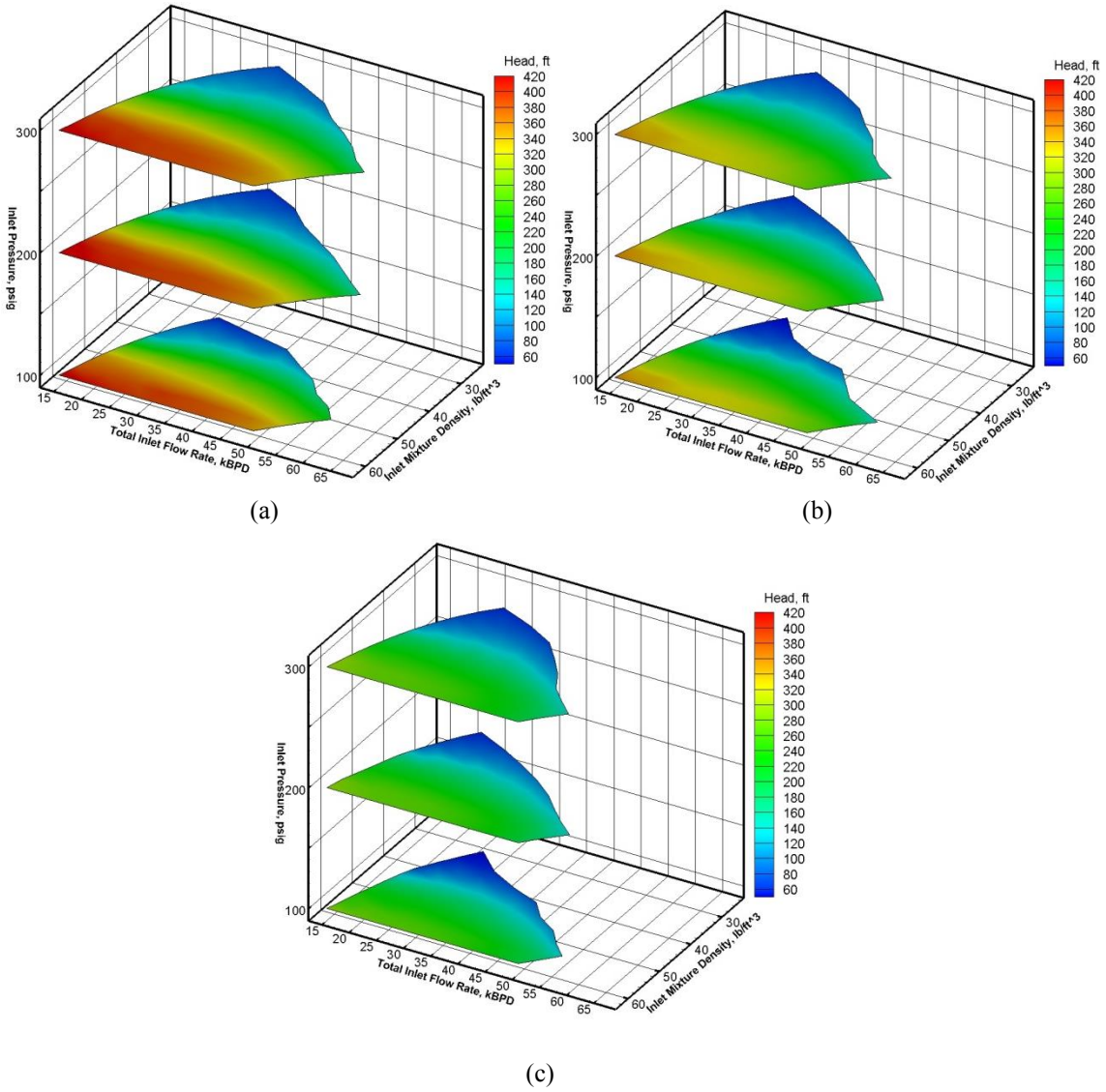

Figure 4-4: Head generated by 3-stage MVP pump for different inlet pressures, inlet mixture densities and total inlet flow rates in (a) 3600 RPM, (b) 3300 RPM, and (c) 3000 RPM

4.1.3. 1-D Momentum Equation

Assuming the homogenous flow within the pump, the pressure rise is determined by considering the effects of mixture density and total volumetric flow rate entering the pump. In this model, no head degradation is considered and the theoretical pump performance is determined employing the pump performance for the single phase.

However, the flow within the pump is not homogenous and this model cannot predict the pump performance accurately. The non-homogeneity of the flow causes head degradation in two-phase pumps due to several reasons,

- *Interphasic forces*: Due to the heterogeneity of the flow, velocity of gas phase and liquid phase are different. Based on the study done by Sachdeva (1988) and Wallis (1969) the drag force per phase per unit volume is defined by the following equations.

$$f_{D,L} = \frac{3}{8}\frac{C_D}{r_b}\alpha^3(1-\alpha)^{-2n+2}\rho_L(V_L - V_G)^2 \tag{4.6}$$

$$f_{D,G} = \frac{3}{8}\frac{C_D}{r_b}\alpha^2(1-\alpha)^{-2n+3}\rho_L(V_L - V_G)^2 \tag{4.7}$$

  In Equations (4.6) and (4.7), n is the function of the Reynolds number. If $Re_\infty > 500$, n is considered to be 2.39 and for low Reynolds number it is considered to be equal to 2.33.

- *Apparent mass:* This force forms in accelerating and decelerating flows. The liquid around the bubbles tends to equalize its kinetic energy with the bubble. As a result, it creates an additional force on the bubble and represents itself as an apparent or additional mass. The apparent mass reduces the head degradation caused by the relative motion of the phases.

$$f_{am,L/G} = -0.5\rho_{L/G}V_{L/G}\frac{d}{ds}(V_L - V_G) \tag{4.8}$$

- *Wall friction losses:* According to the flow regime and gas concentration in each location wall friction losses vary in different sections of the pump.

- *Velocity angles and recirculation zones:* Additional air in the flow changes the velocity angles; therefore it can create or suppress the recirculation zones in the flow path.

4.1.4. Stage By Stage Performance

To understand the pump performance in more detail, a stage by stage study on the pump is performed. Generated head from each pump stage was calculated based on the mixture density at the stage inlet. The results for the 100 psig pump inlet pressure are shown in Figure 4-5 (a-c) for each three stages at 3600 RPM. For higher GVFs the generated head due to the pump head degradation is lower. By increasing the number of stages the homogeneity of the flow increases. This means the head plot curve for each pump inlet GVF (GVF_i) approaches the head plot curve for pure water.

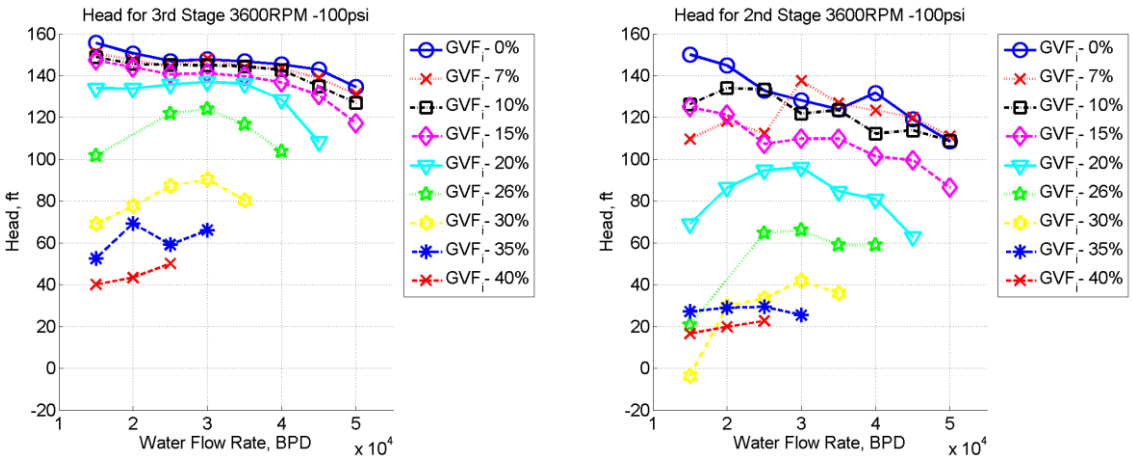

(a) (b)

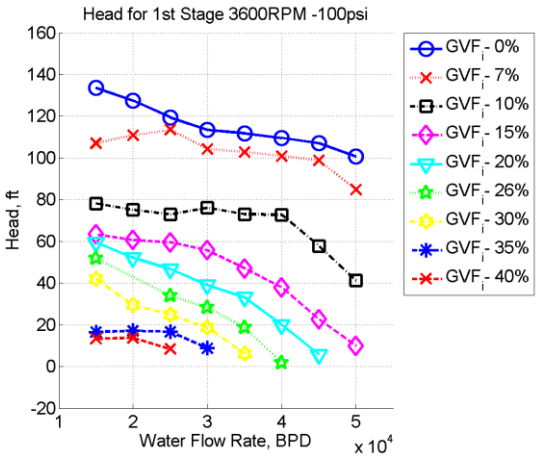

(c)

Figure 4-5: Stage head generation for (a) 3rd stage, (b) 2nd stage, and (c) 1st stage in 3600 RPM and 100 psig pump inlet pressure

To demonstrate the deviation of flow homogeneity for different stages the "Head Ratio" is defined according to the following equation,

$$Head\ Ratio = \frac{Head_{exp}}{Head_{homogeneous}} \tag{4.9}$$

In Equation (4.9), $Head_{homogeneous}$, is the theoretical pump stage head according to the homogenous model and affinity laws. In Figure 4-6 (a-c), Head Ratio for different stages with respect to the gas volume fraction at the stage inlet, GVF_s, is shown. The plots are for different water flow rates at 100psig pump inlet pressure and rotating speed of 3600RPM.

The closer the Head Ratio curve is to one, the more homogenous the flow within a stage is. In the 3rd stage, all the head ratio plots for different water flow rates almost lie on a common curve, also for 2nd stage except for very low water flow rates and low gas volume fractions, the rest of the curves follow the same trend. Whereas, in the 1st stage, head ratio plots only follow the same trend until almost 10% GVF. In the second stage for very low water flow rate, 15 kBPD, high pressure rise fluctuations were observed.

The plots shown in Figure 4-6 are related to the head ratio curves at 100 psig pump inlet pressure. To investigate the pump inlet pressure effects on the head ratio at the 3rd stage, head ratio plots for different pump inlet pressures are plotted in Figure 4-7 (a-c). Since, the effects of the pump inlet pressure are included in the calculation of $Head_{homogeneous}$, the head ratio curves are slightly a function of pump inlet pressure. However, for higher inlet pressures, the head ratio curves move slightly toward the unity head ratio.

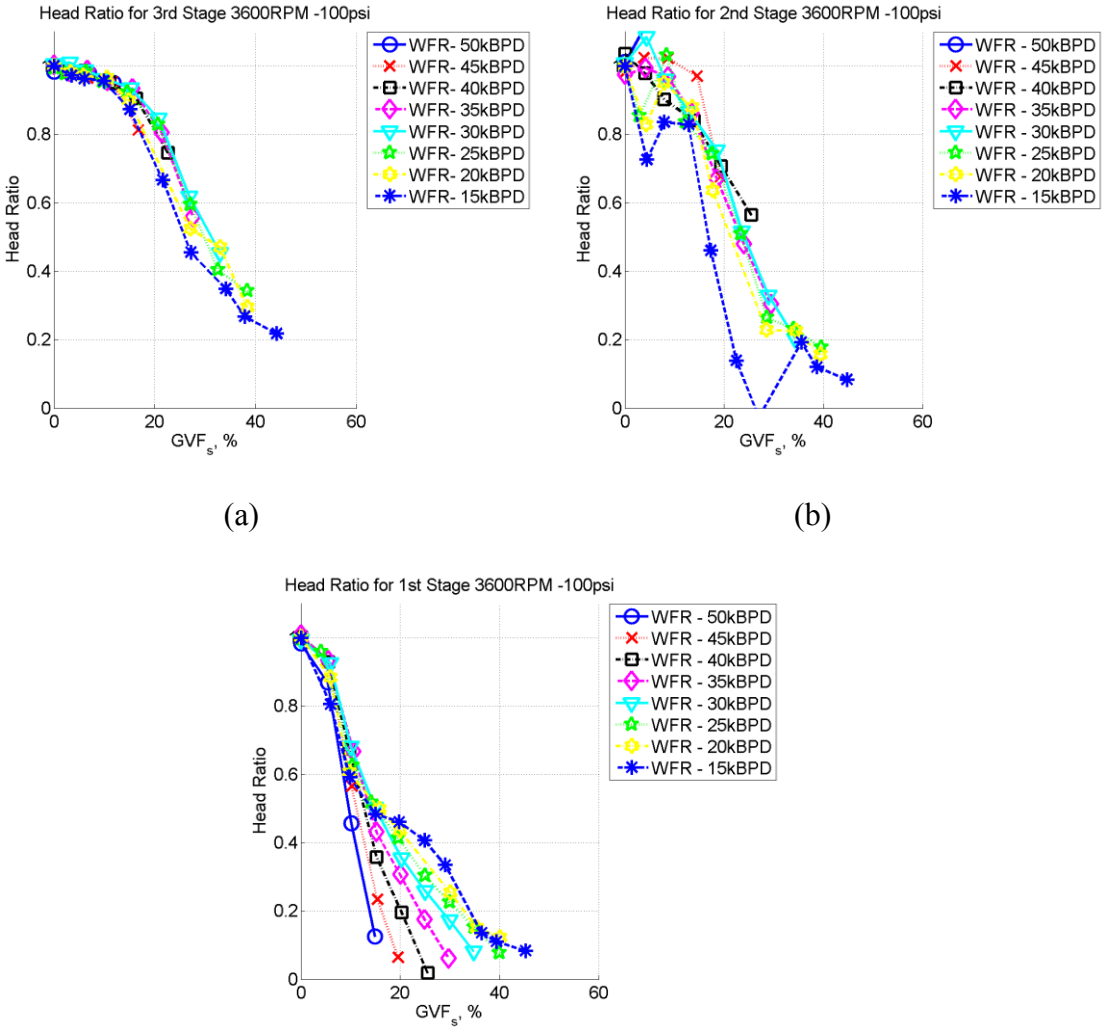

Figure 4-6: Stage by stage head ratio (a) 3rd stage (b) 2nd stage, and (c) 1st stage in 3600 RPM and 100 psig pump inlet pressure

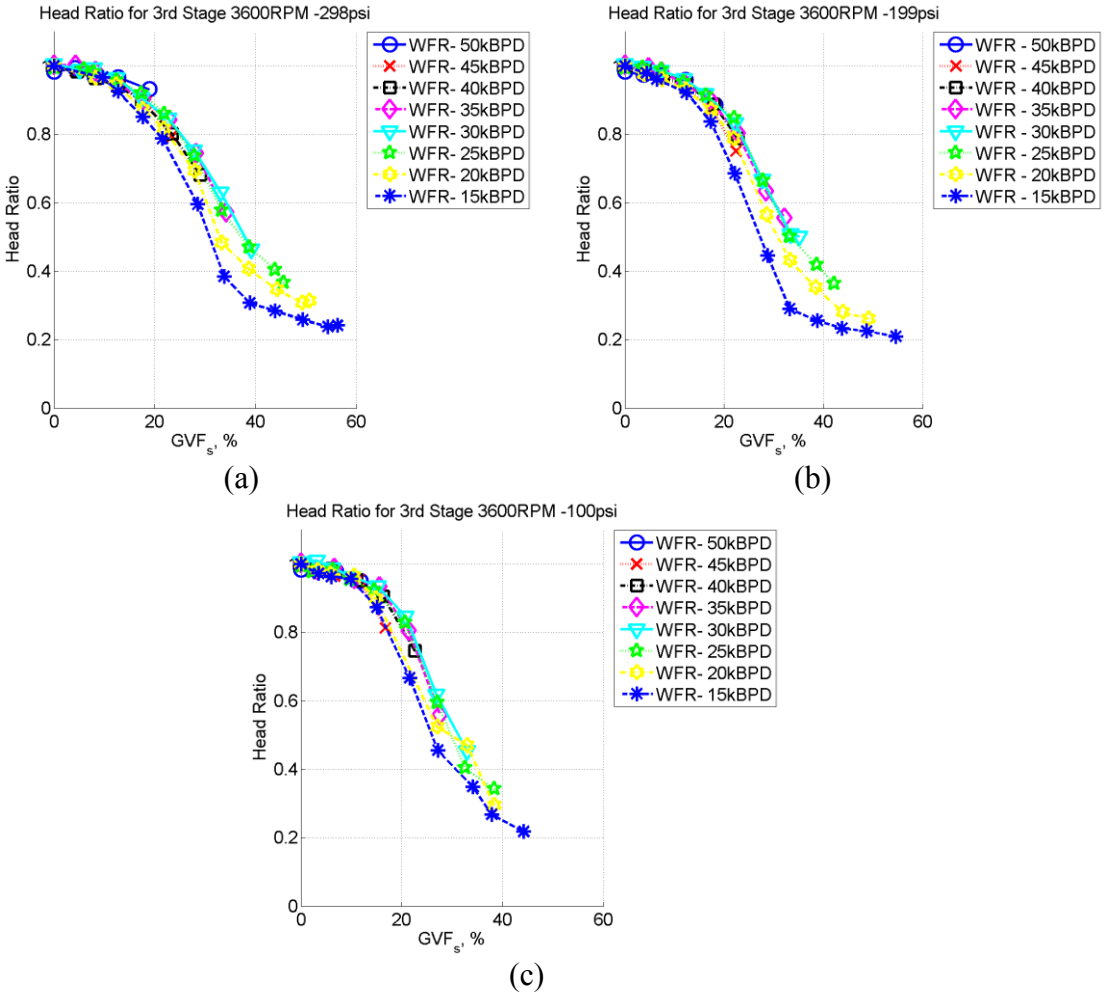

Figure 4-7: Pump inlet pressure effect on the head ratio of the 3rd stage (a) 300 psig (b) 200 psig (c) 100 psig at 3600 RPM

In Figure 4-8 (a-c), head ratio plots for different rotating speeds at 300 psig pump inlet pressure are shown. Similar to the effects of the inlet pressure, since the influence of the rotating speed is considered in $Head_{homogeneous}$, head ratio is slightly a function of rotating speed. In higher rotating speeds the homogeneity of the flow within the pump increases which corresponds slight move of the head ratio curves toward the unity head ratio.

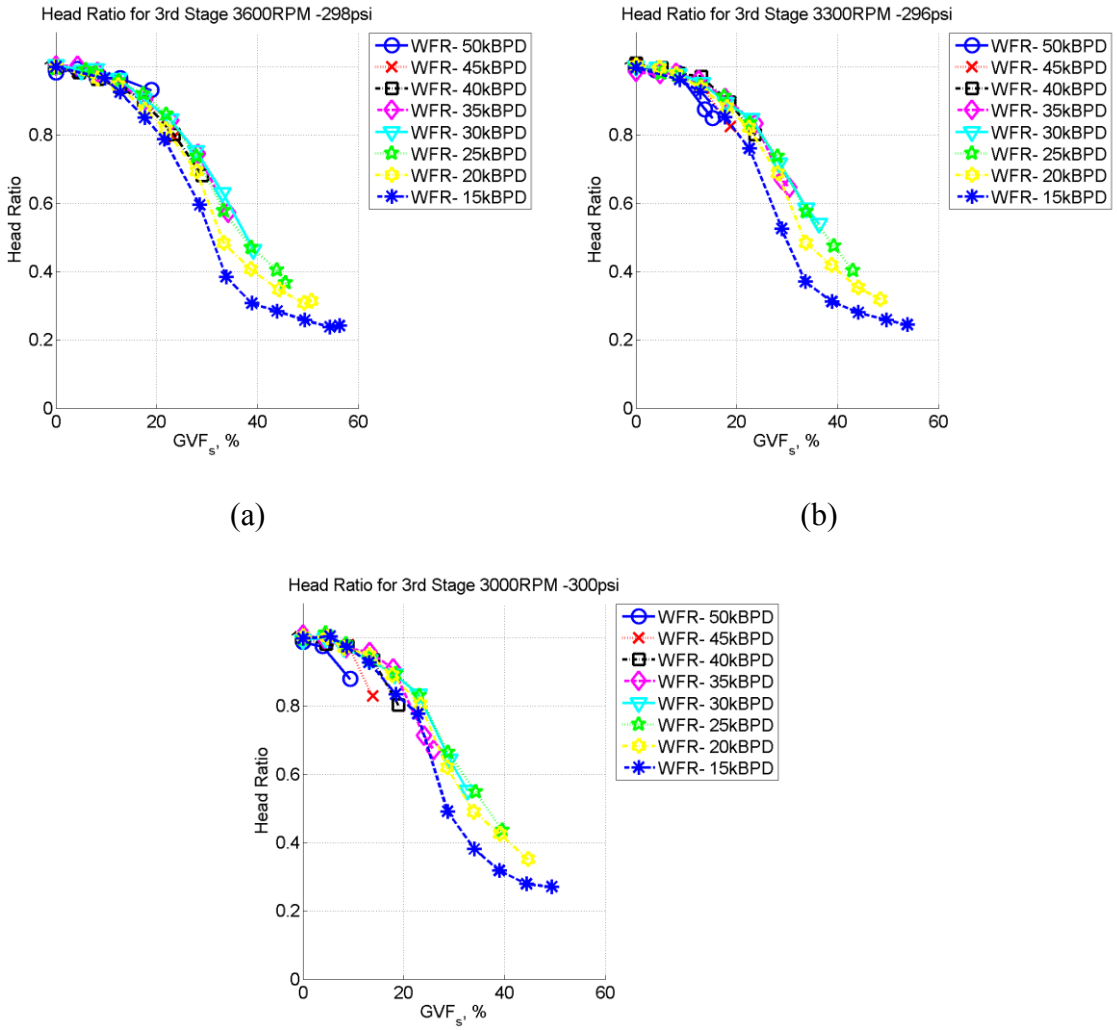

Figure 4-8: Rotating speed effects on 3rd stage head ratio (a) 3600 (b) 3300 (c) 3000 RPM for 300 psig pump inlet pressure

4.1.5. Pressure Distribution along MVP-ESP Pump

To study the performance of the pump better, the stage with pressure taps is located in two stages. According to Figure 4-9, one pressure tap is located right after the impeller, Figure

4-9 (a), and one pressure tap is located right before the impeller, Figure 4-9 (b). The three pressure taps, at the diffuser outlet in Figure 4-9 (c), measure the equivalent pressure between the chamber located between the inner and outer wall of the diffuser and the next stage impeller inlet. Therefore, the pressures measured in this location correspond to the combined pressure at the impeller inlet and pressure observed at the impeller shroud.

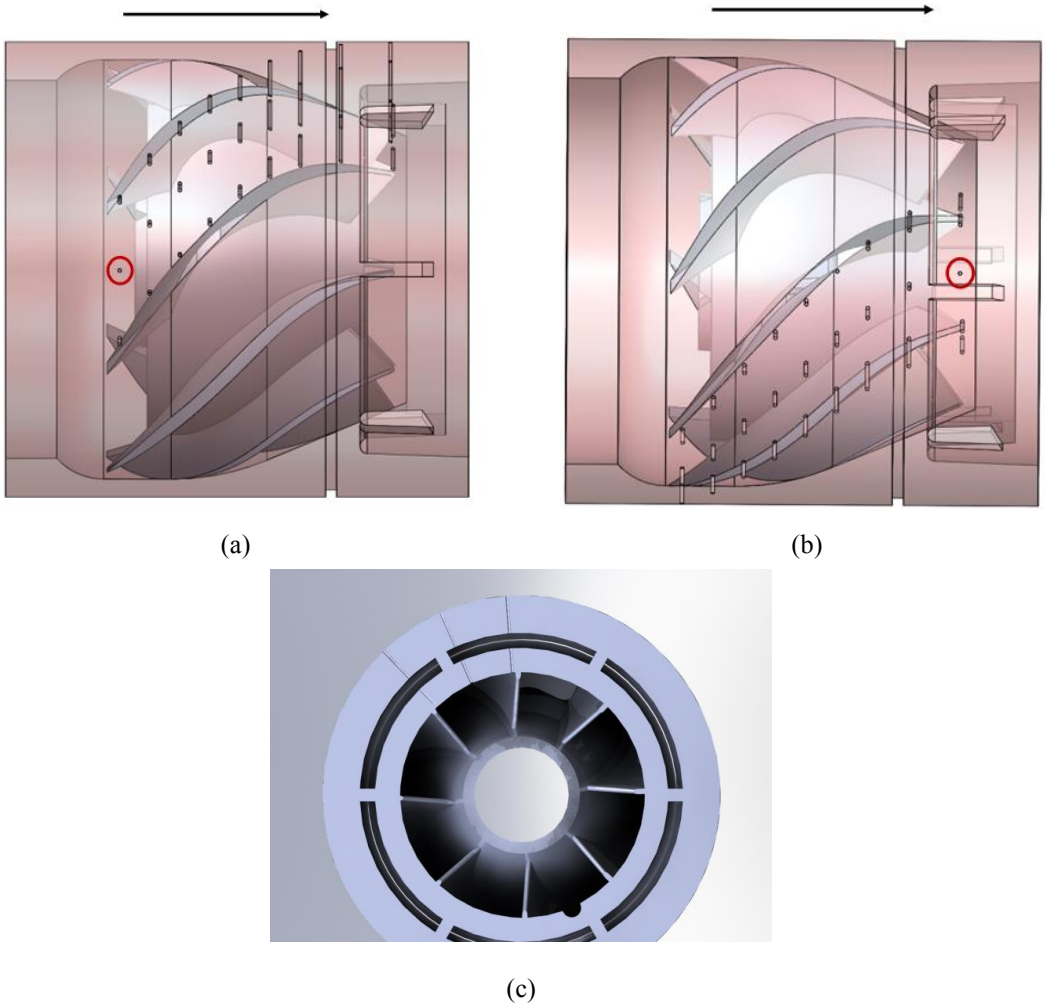

(a) (b)

(c)

Figure 4-9: Pressure tap locations (pressure and suction side and meridional plane) on diffuser (a) side view 0deg (b) side view 90 deg (c) location of pressure taps at the outlet of diffuser

The pressure distribution along the meridional plane of the pump is shown in Figure 4-10 for two different water flow rates. Two common pressure drops in the diffuser section in both stages are noticeable. The first pressure drop occurs at the 4/9 of the stage length, and the other one happens at 7/9 of the stage length. The location of these two pressure drops in the flow path is shown in Figure 4-11 (a-b). The pressure drop that occurs at the impeller outlet or the diffuser inlet, $L_1(\frac{x}{L_s} = 4/9)$, is more noticeable than the one happens within the diffuser, $L_2(\frac{x}{L_s} = 7/9)$. Increase in GVF causes a decrease in pressure drop in L_1 whereas an increases in pressure drop for L_2 for both the first and second stages of the pump. By increasing the amount of gas content in the working fluid, the pressure rise by the impeller decreases while the pressure drop caused by the recirculation zone at the impeller exit (L_1) due to the air presence decreases.

According to Figure 4-10, in high gas volume fractions, the pressure within the first stage stays nearly below stage inlet pressure. At the second stage outlet, pressure slightly starts to go above the pump inlet pressure. These low performance stage characteristics are due to the non-efficient mixing performance of the first and second stage impellers in the presence of high GVFs.

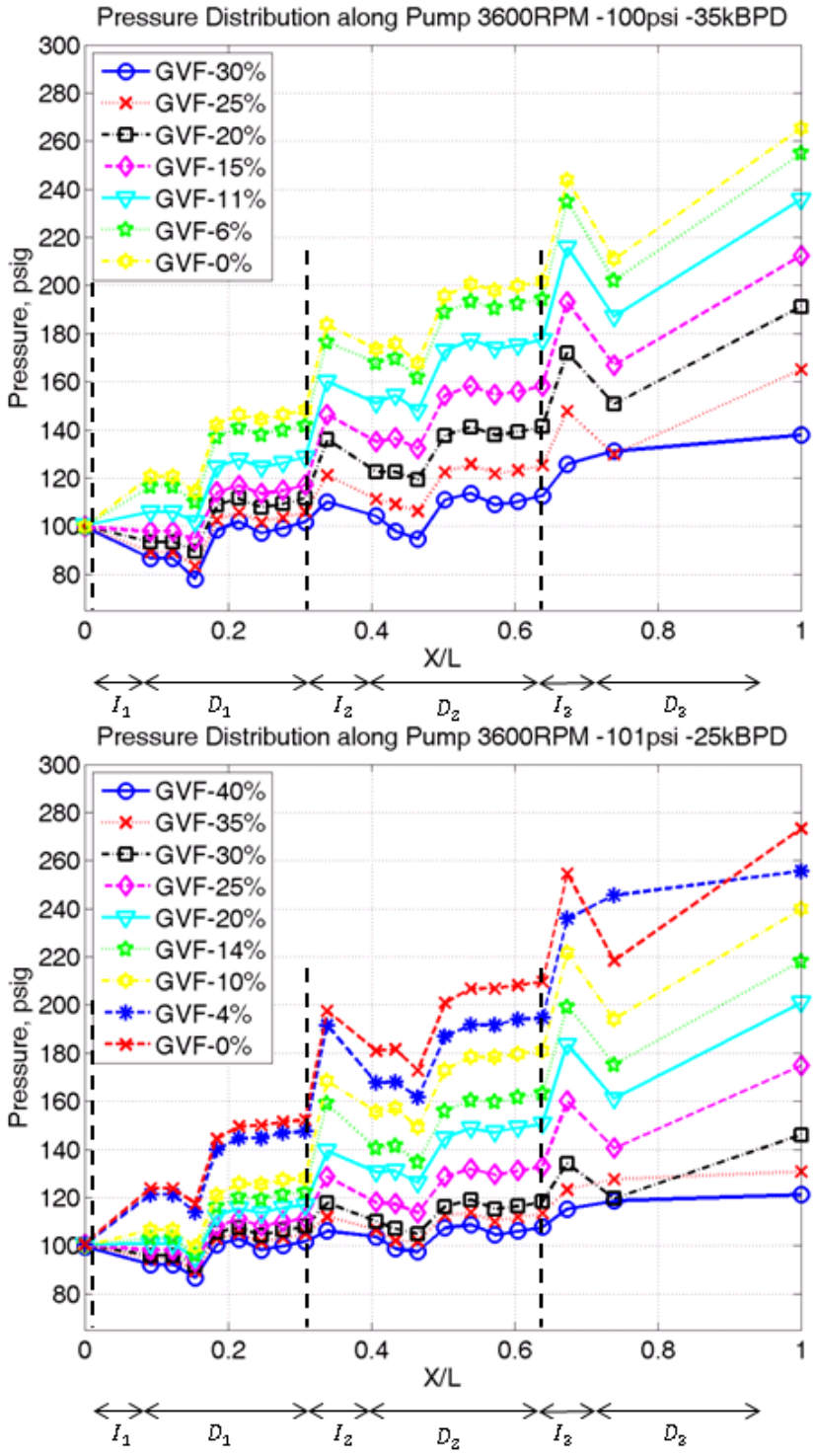

Figure 4-10: Pressure distribution along meridional plane of three stages of the MVP pump for different pump inlet GVFs and two water flow rates 25 kBPD and 35 kBPD
(I_n: $Impeller\ No.n$, D_n: $Diffuser\ No.n$)

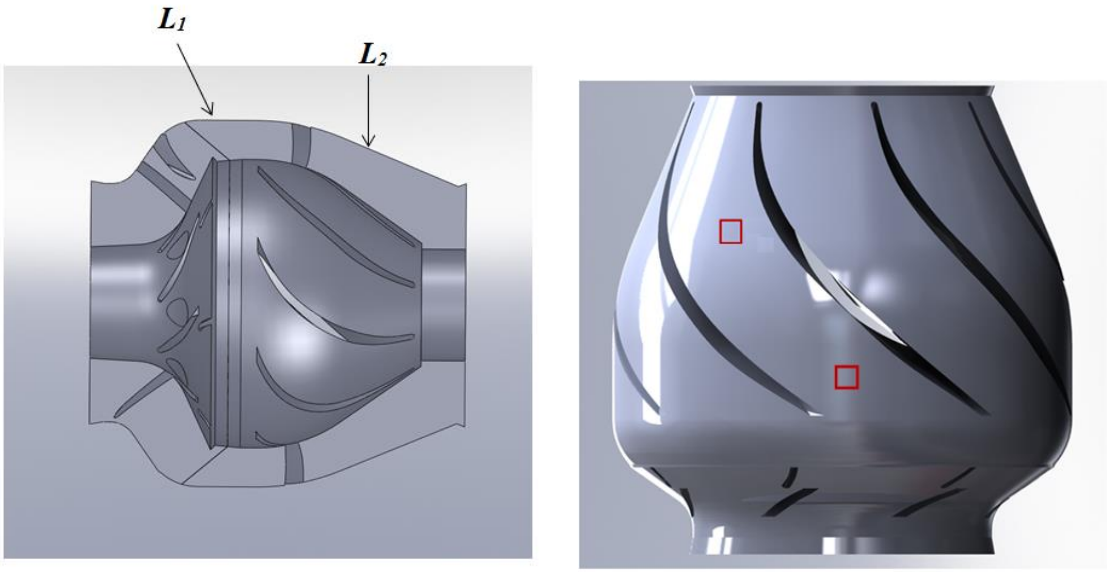

(a) (b)

Figure 4-11: Pressure drop locations on the stage flow path (a) section view (b) side view

In Figure 4-12, the comparison of pressure distribution along the meridional plane in the first and second stages are shown. According to this figure, the pressure distribution follows the same trend. Also, the pressure drop locations are quite the same.

In Figure 4-13, the pressure distribution in 2nd stage diffuser along pressure side, meridional plane and suction side are shown. In location L_1, due to the change of the flow path angle from outward flow to axial flow, a recirculation zone near to the diffuser hub is created. This phenomena cause a pressure drop in this location.

In location L_2, due to the existence of a recirculation zone, the pressure at suction side and meridional plane are nearly close to each other. According to Figure 4-11 (a), since the flow path angle changes in L_2, a recirculation zone is produced in this region.

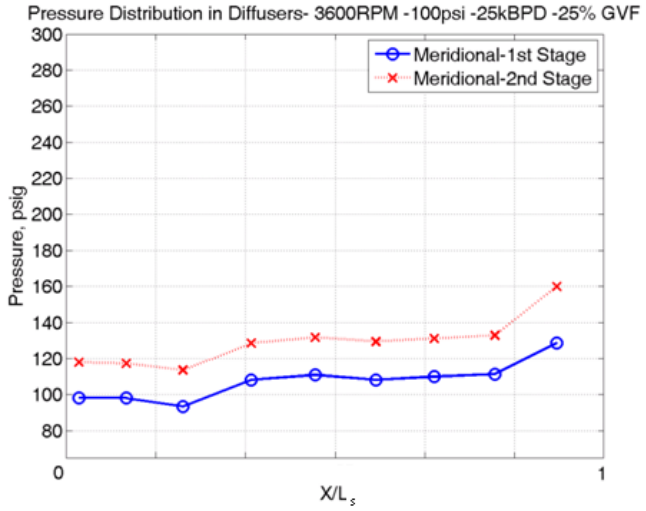

Figure 4-12: Pressure distribution along the meridional plane of the first and second stages - rotating speed: 3600 RPM – Pump inlet pressure: 100 psig – Water flow rate: 25 kBPD – Pump inlet GVF: 25%

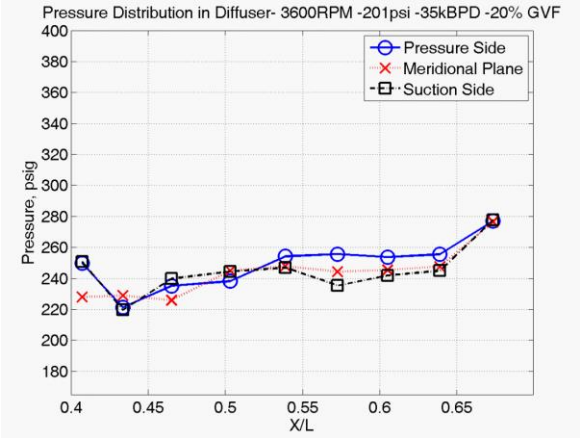

Figure 4-13: Comparison of pressure distribution between pressure side, suction side and meridional plane in second stage diffuser

4.2. High Speed Photography

The high speed photography setup is shown in Figure 4-14. This setup is employed to measure the bubble size, bubble velocity and also used to identify the location of recirculation zones. In recirculation zones, the quality of gas concentration in comparison with other regions is also the point of interest.

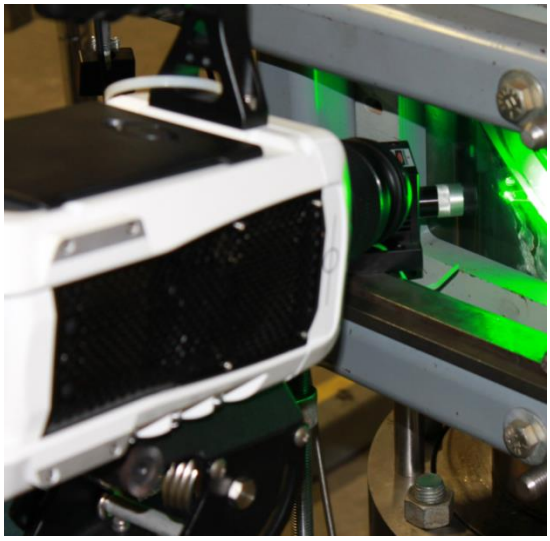

Figure 4-14: High speed photography with the laser source

4.2.1. Bubble Size and Velocity Measurement

To measure the bubble size and bubble velocity isolated bubbles needs to be captured. It can be accomplished in low gas volume fraction and low water flow rates (Rotating speed: 3000 RPM, $GVF_i < 3\%$, Water flow rate: 10.28 kBPD). To obtain the better quality in images, backlight technique using the reflected light from diffuser's hub is utilized. A sample image before preprocessing for location L_2 is shown in Figure 4-15 (a) using the

image properties summarized in Table 4-1. Insight 4G software is utilized to process and invert the images. This software is capable of measuring the bubble sizes and velocity vectors.

Table 4-1: Image properties

Resolution	Speed, FPS	Pixel size
320×240	50,000	$19\mu m$

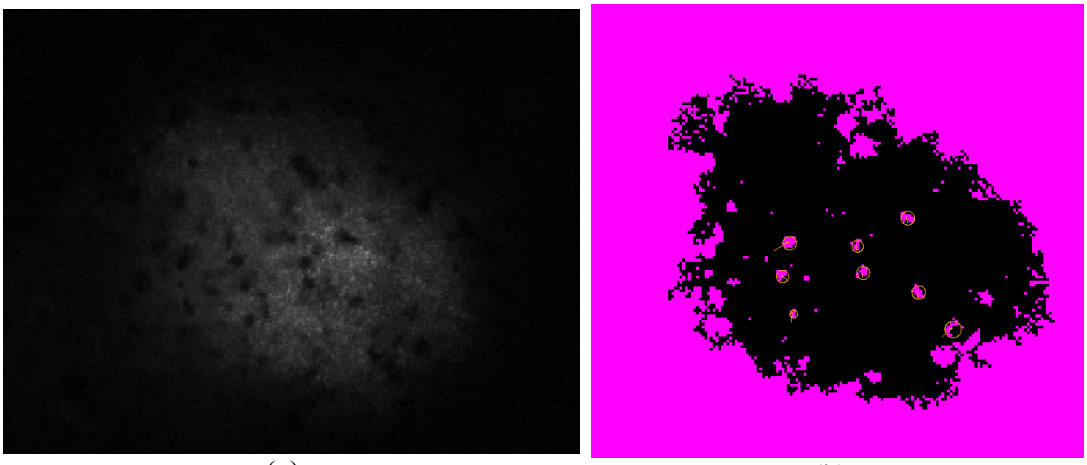

(a) (b)

Figure 4-15: (a) Captured image for location L_2 from reflected light (back light) (b) processed image with bubble size and velocity vectors generated in Insight 4G software – Rotating speed: 3000 RPM, $GVF_i < 3\%$, Water flow rate: 10.28 kBPD

Employing the images processed and obtained from Insight 4G software, the transient average bubble diameter (Figure 4-16) and bubble diameter Histogram (Figure 4-17) are calculated. The average bubble diameter for all the frames in this operating condition and this location was obtained to be $95\mu m$.

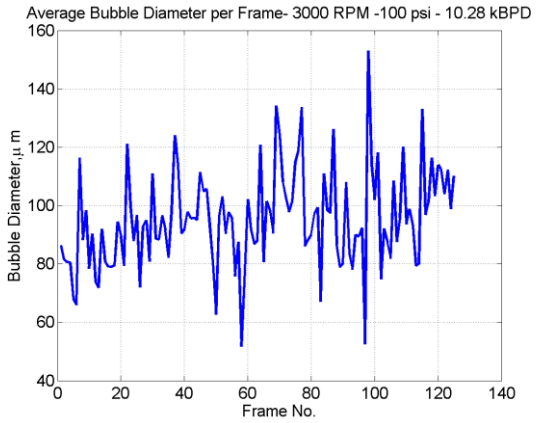

Figure 4-16: Average bubble diameter per image

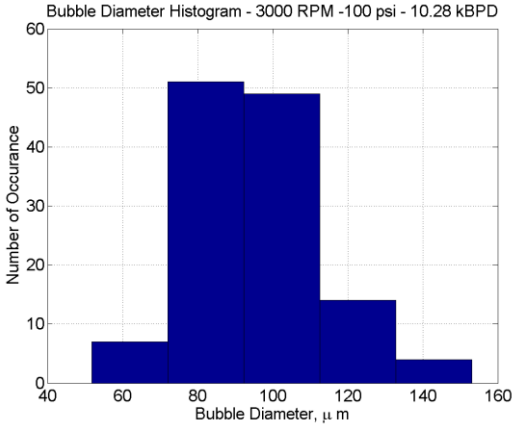

Figure 4-17: Bubble diameter Histogram

Transient bubble velocity and its Histogram are shown in Figure 4-18 and 4-19 respectively.

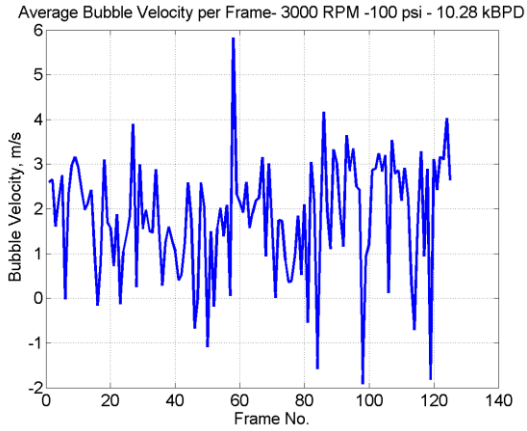

Figure 4-18: Average bubble velocity per frame

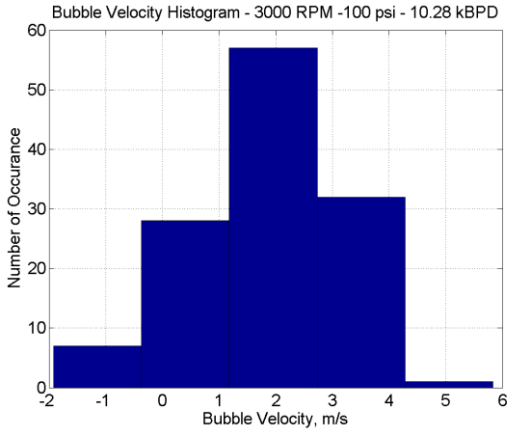

Figure 4-19: Bubble velocity Histogram

For a known gas volume fraction and water flow rate at the location of high speed photography, average water velocity is calculated if no recirculation occurs in this

location. In Table 4-2, the aforementioned water velocity is compared with the average air bubble velocities obtained by high speed photography. The difference between velocities can be the result of,

- Slip velocity between phases
- Existence of the recirculation zone
- Near shroud air bubble velocity measurement in high speed photography

Table 4-2: Velocity Comparison

	Velocity, m/s
Calculated Water Velocity in L_2	2.12
Measured Air Bubble Velocity in L_2	1.81

4.2.2. Recirculation Zone

According to CFD results performed by Rasmy Marsis (2012) for the MVP-G470, a recirculation region was captured (Figure 4-20). He found that in this region gas concentration, Figure 4-20 (a), is lower and also the velocity of water phase, Figure 4-20 (b), is lesser.

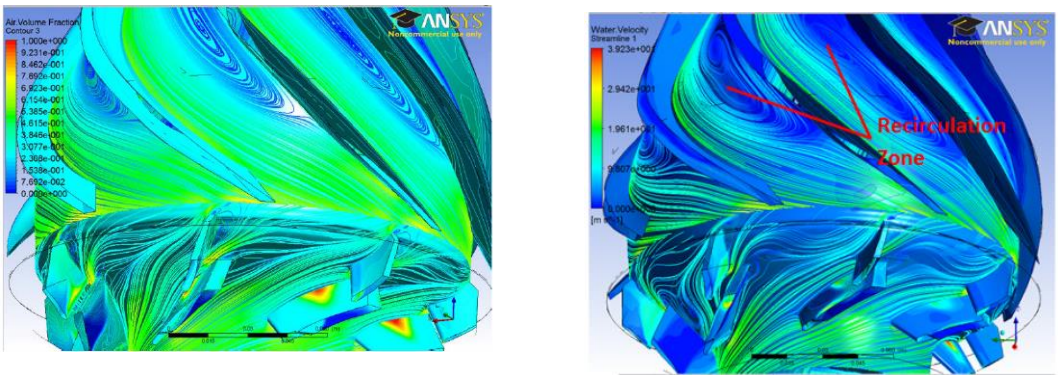

(a) (b)

Figure 4-20: CFD simulation performed by Rasmy Marsis (2012) (a) Air volume fraction (b) Water velocity streamlines

Using high speed photography in the recirculation region which corresponds to location L_2, slow moving isolated bubbles are captured (Figure 4-21). This shows a good agreement between the experimental results obtained from high speed photography and the CFD results. As it was discussed, this region causes a pressure drop within the diffuser.

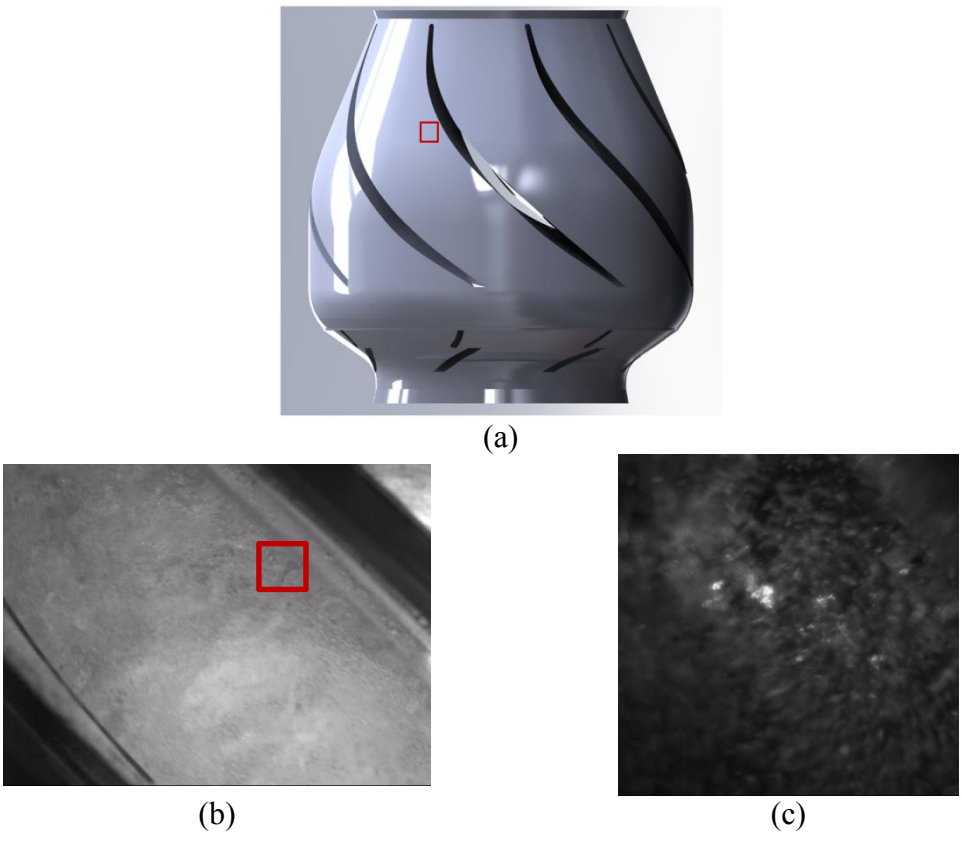

Figure 4-21: Recirculation zone (a) the location of the image in the flow path (b) Two -phase flow in diffuser (c) slow moving isolated bubbles

The low gas concentration of the recirculation zone can be resulted from the dynamic response of bubbles in an oscillatory fluid field with very low pressure gradient (Tavoularis (2005)). For rigid particles suspended in a sinusoidal oscillating fluid field with different density ratios, particles' oscillation amplitude ratio varies for different Stokes numbers according to the Figure 4-22.

In this figure, density ratio is defined as,

$$\gamma = \frac{\rho_p}{\rho_f} \tag{4.10}$$

and the Stokes number is defined as,

$$S = \sqrt{\frac{\omega d_p^2}{8\upsilon_f}} \tag{4.11}$$

In obtaining Figure 4-22, drag forces and apparent mass were considered to be exerted on particles and no pressure gradient was included in obtaining these results.

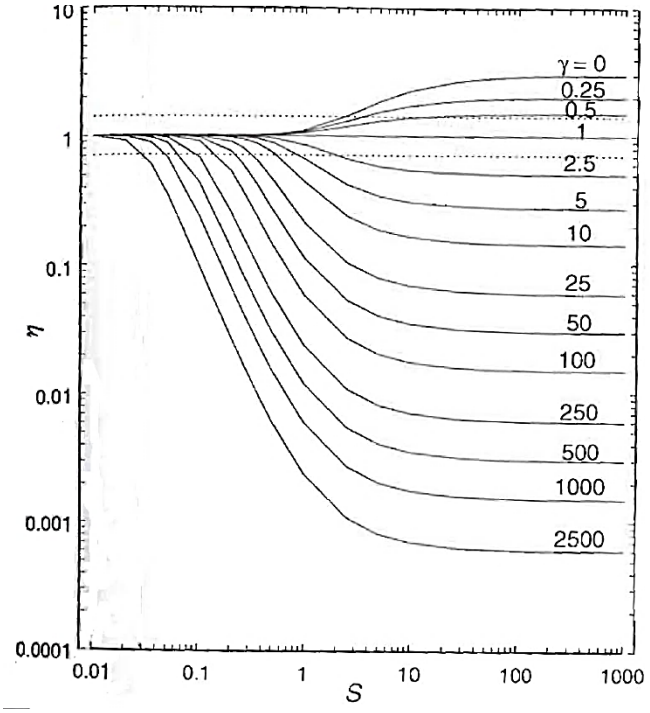

Figure 4-22: Rigid particles' response in an oscillating flow field (Tavoularis (2005))

According to Figure 4-22, for particles with low density ratios when Stokes number is higher than one, amplitude ratio of the particles is higher than one. It means for particles with lower density, i.e. air bubbles in water, particles' oscillation amplitude is higher in a flow field with low pressure gradient in the flow field. For the bubble diameter of 95 μm obtained from section 4.2.1 and with the assumed recirculation angular velocity of 3.3 $krad/s$ ($\omega = \frac{10m/s}{3mm}$), Stokes number for recirculation zone which occurs within the diffuser is found to be about 2. According to the low azimuthal pressure gradient shown in Figure 4-13, and aforementioned discussion, bubble tend not to follow the water streamline to enter the recirculation zone. Also, due to their high amplitude ratio, the gas bubbles tend not to follow sharp curvatures. In conclusion, this phenomena decrease the number of bubbles in the recirculation region.

4.2.3. Electrical Resistance Tomography

Experiments were carried out for different inlet pressures, liquid flow rates, GVFs and rotational speeds to find the concentration of two phase flow across the diffuser flow path in a 3-stage MVP-ESP. The resistivity of fluid in diffuser section of 1st and 2nd stage was measured. Based on the resistivity of fluid, gas concentration is obtainable. In Figure 4-23, raw conductivity tomogram for different inlet gas volume fractions with 30 kBPD water flow rate and 100 psig inlet pressure is shown. In Figure 4-23, the effect of temperature on fluid conductivity has not been considered. Since the experiments were carried out over a period of time maintaining constant inlet temperature which was similar to reference frame was very difficult. In order to compensate the effects of varying inlet temperature, the conductivity tomogram for different inlet temperatures was obtained by running the

ERT system in a constant liquid flow rate and varying temperatures. The obtained variation was used to obtain corrected concentration using Eq. (3.1). The ERT system has a measuring domain of $20\ pixel \times 10\ pixel$. The physical dimension of each pixel is 3/8" by 3/8". The boundaries of the fluid domain are shown in Figure 4-24. The black line corresponds to the wall with electrical insulating paint whereas the orange line corresponds to the location of 16 electrodes on the window. The white lines represent inlet and outlet of the fluid domain in the diffuser.

According to Figure 4-23, as it is expected, an increase in the inlet gas volume fraction from 0% to 35% reduces the measured relative conductivities at the pixels located in the fluid domain.

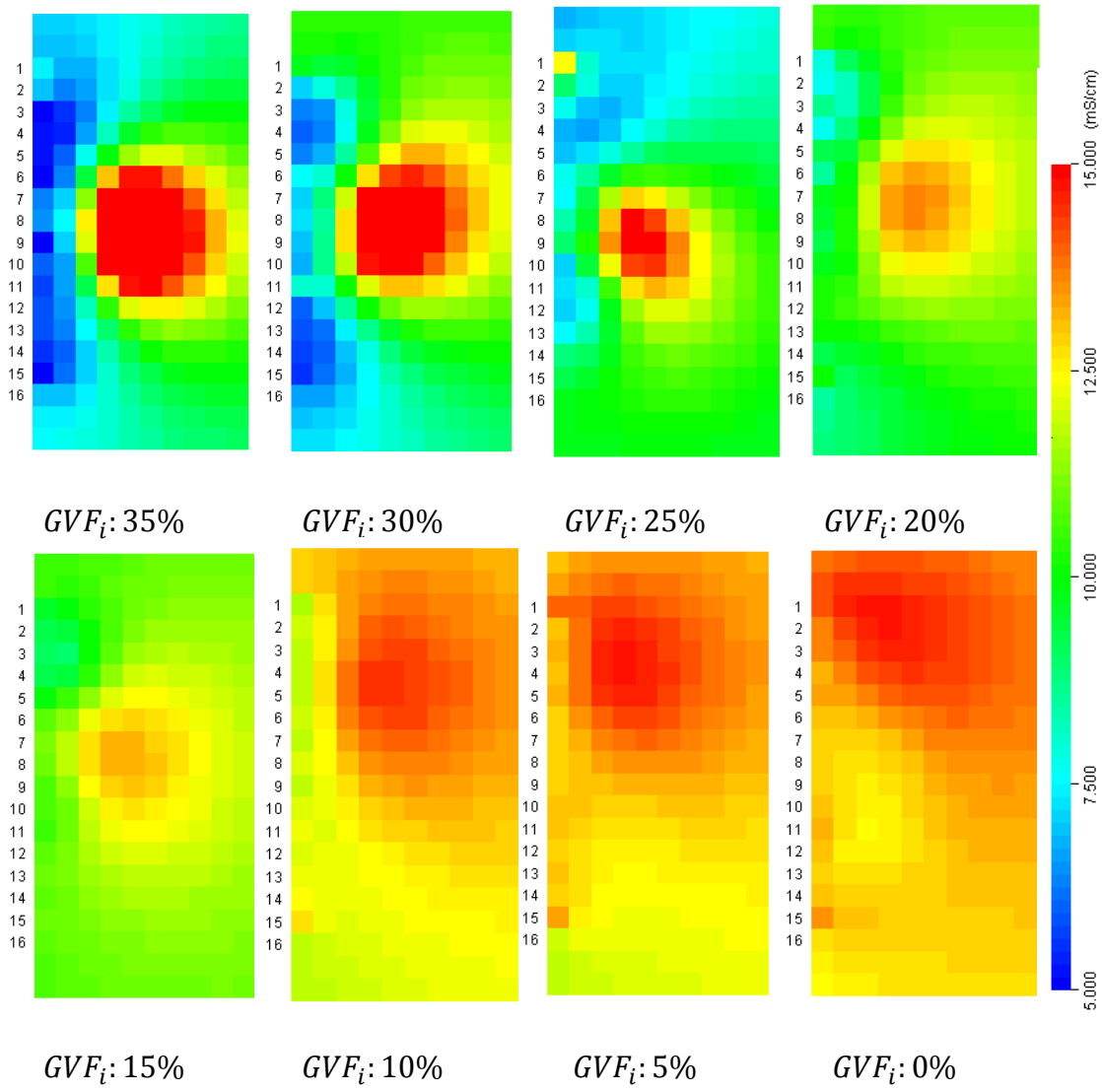

Figure 4-23: Raw conductivity tomogram for different inlet GVFs with 30 kBPD water flow rate and 100 psig inlet pressure

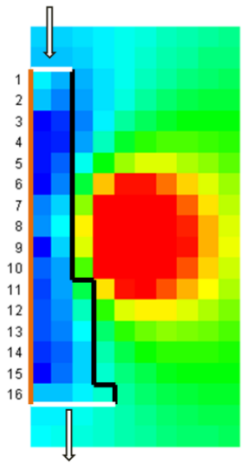

Figure 4-24: Fluid domain of the resistivity tomogram in diffuser – black line is the inner wall of the diffuser, orange line corresponds to the outer wall of the diffuser where electrodes are installed and white lines represent inlet and outlet of the fluid domain in the diffuser

In Figure 4-25, the comparison of measured concentration (solid lines) and calculated GVF (dashed lines) for different inlet no-slip gas volume fractions (λ_i) for the first stage is shown. The conductivity values employed in computing the concentration in Figure 4-25 are the radial averaged values of the pixels shown in Figure 4-24 for each of the 16 electrodes. The GVF is calculated based on the local temperature and pressure where the electrodes are located.

At the inlet of the diffuser, which corresponds to L_1 =x/L_s = 4/9 (L_s : stage length), due to the centrifugal forces of the impeller and also inertial forces' differences between liquid and gas phase, the velocity of the liquid phase tends to be higher than the gas phase. As a result, according to the mass conservation, liquid phase occupies less space at this location which leads to higher gas concentration in comparison with the local gas volume fraction.

The difference between local gas concentration and gas volume fraction demonstrates high slip velocities between two phases.

Within the diffuser (4/9<x/L_s<1), according to Figure 4-25, phase velocities tend to be equal to each other. Therefore, gas concentration decreases and approaches the value of the local GVF. However, a sudden dip in concentration value occurs at L_2 =x/L_s =7/9 for all different inlet gas volume fractions. According to Figure 4-11, since the flow path angle changes in L_2, a recirculation zone is produced in this region. At the recirculation zone of the first stage ($L_2 = \frac{X}{L} = 0.24$), as it was discussed in section 4.2.2, gas concentration is low. Due to the lower gas content within this region, the gas concentration decreases sharply at this location. The recirculation zone captured based on ERT measurements was also shown in the CFD results obtained by Marsis (2012) on the same MVP-ESP pump. At the end of the diffuser, according to the effects of the impeller and the value of the inlet gas volume fraction, the amount of gas concentration varies.

At higher inlet gas volume fractions the deviation between gas concentration and local GVF is higher.

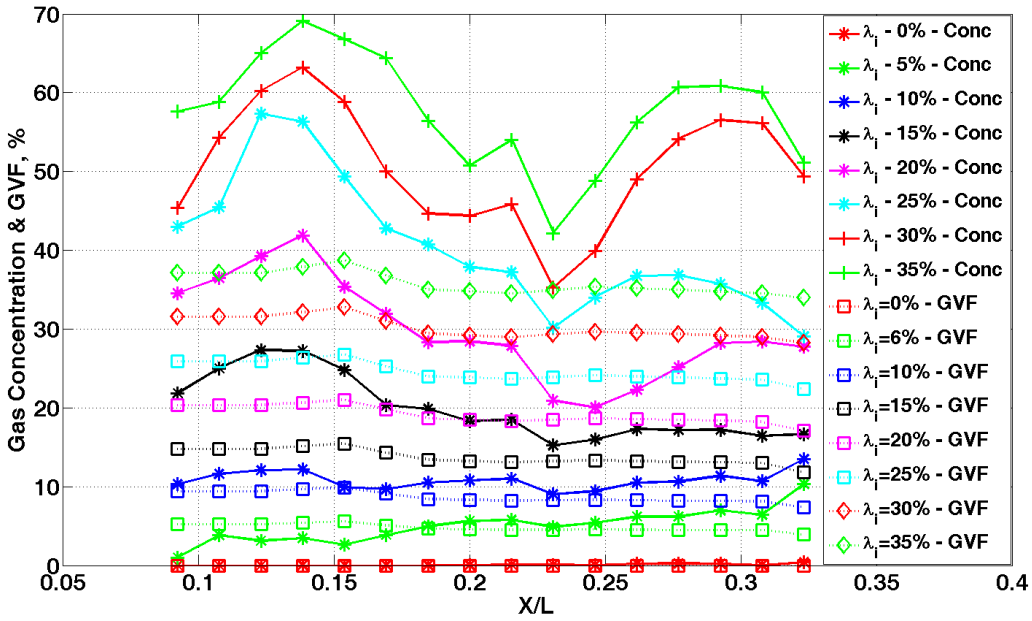

Figure 4-25: Gas concentration and GVF distribution along diffuser of the first stage – speed: 3600 RPM, inlet pressure 100 psig, and water flow rate: 30 kBPD – solid lines are related to concentration and dashed lines are related to GVF

In Figure 4-26, the concentration and local GVF distribution for the 1st and 2nd stages are shown for two different water flow rates. By increasing the water flow rate, the deviation between gas concentration and local GVF decreases. The lower deviation between two curves corresponds to higher homogeneity. This means, in higher water flow rates the homogeneity of the flow increases.

In Figure 4-26 and Figure 4-27, for the second stage, due to the mixing effects of the second impeller, the deviation between two curves which are the gas concentration and local GVF decreases.

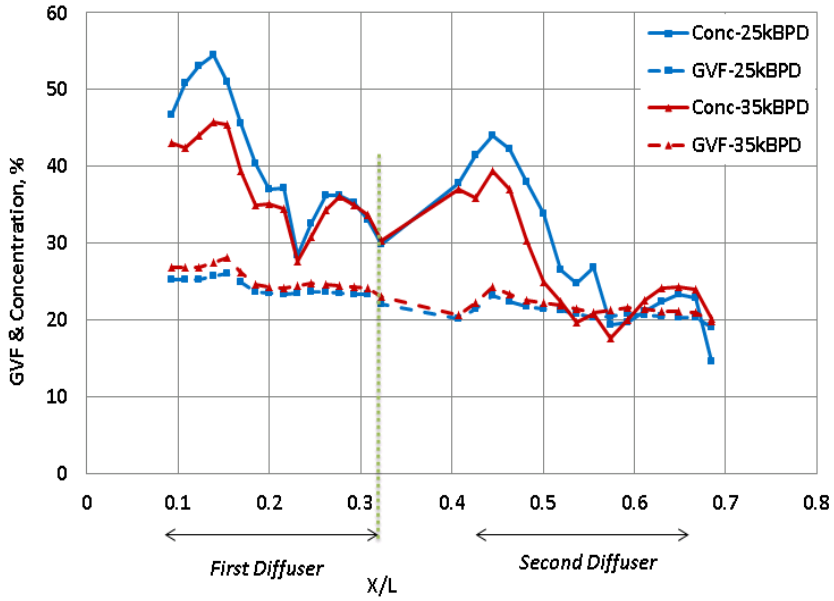

Figure 4-26: Water flow rate effects on GVF and concentration distribution along the first and second stages - rotating Speed: 3600 RPM, inlet pressure: 100 psig, inlet GVF: 25%

In Figure 4-27, the effects of the inlet no-slip gas volume fraction are studied. In higher inlet GVFs, the deviation between two curves is higher which corresponds to higher slip between phases and higher head degradation.

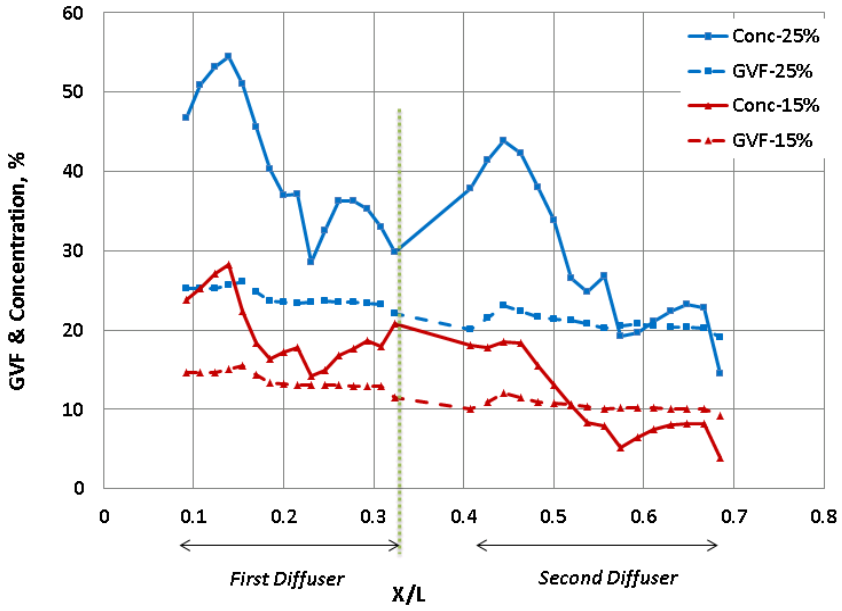

Figure 4-27: Inlet GVF effects on GVF and concentration distribution along first and second stages – rotating speed: 3600 RPM, inlet pressure: 100 psig, water flow rate: 25 kBPD

According to Figure 4-28, higher inlet pressure increases the deviation between the local GVF and concentration. In higher inlet pressures, the compressibility of fluid decreases. As the results, the variation of the local GVF and concentration throughout a single stage decreases.

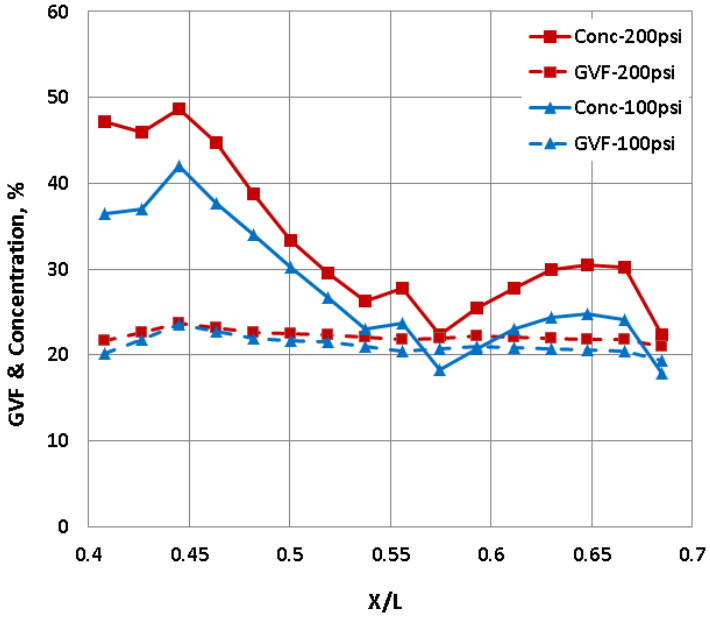

Figure 4-28: Pressure effects on concentration distribution at the second stage diffuser water flow rate: 30 kBPD, inlet GVF: 25% and 3600 RPM

In higher rotating speeds of the impeller, due to the higher centrifugal forces and phases' inertial differences, slip velocity between phases increases. Since, the velocity of liquid phase in comparison with the velocity of the gas phase in higher rotating speeds is higher, therefore, the liquid phase occupies less space which results in a higher gas concentration in that location. In contrast with the concentration, local GVF for higher rotating speeds is lower due to the higher pressure that pump generates in higher rotating speeds. The comparison of the gas concentration and local GVF for different rotating speeds is shown in Figure 4-29.

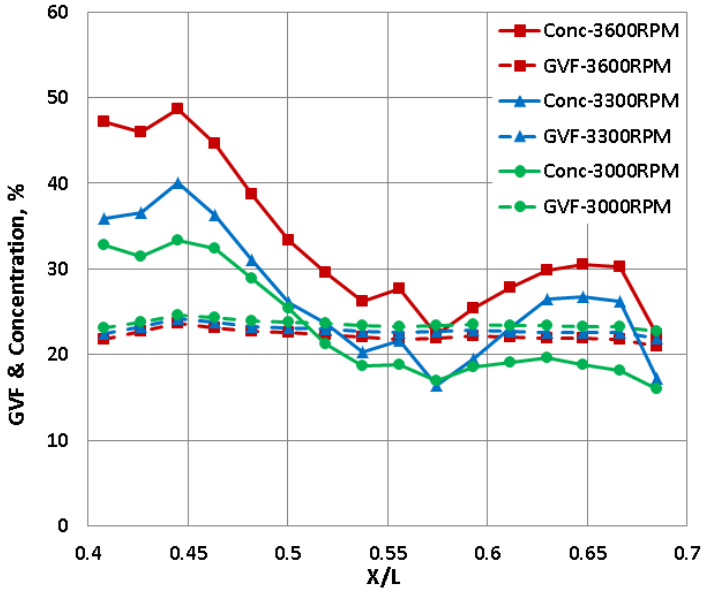

Figure 4-29: Rotating speed effects on concentration distribution at the second stage diffuser - water flow rate: 30 kBPD, Inlet pressure: 200 psig and Inlet GVF: 25%

Stage-by-stage pressure distribution for this pump (Figure 4-10) demonstrated two common pressure drops occurring at L_1 and L_2, the same locations where very high and very low concentration values were obtained. The agreement between pressure and concentration measurements represents the direct relationship between stage's head degradation to the deviation between gas concentration and local GVF.

4.2.4. Stage by Stage Head Ratio Prediction

In this section theoretical head ratio prediction is studied to relate the variation of head ratio for different stages in Figure 4-6 (a-c) to the experimental measured values obtained from resistance and pressure measurements discussed respectively in sections 4.3 and 4.1.5.

As it was discussed in previous sections, two common pressure drops occur in locations L_1 and L_2 in the understudy first and second pump stages. Pressure drop in location L_1 demonstrates more influence on the stages performance than location L_2. This location (L_1) that corresponds to the impeller outlet was studied in more detail to relate the flow characteristics in this location to the stage's head performance.

In Figure 4-29 (a) and (b), the gas concentration, obtained from ERT system, at the stage's impeller outlet for the first and second stage of the pump for different stage inlet GVF at 3600 RPM and 100 psig pump inlet pressure are shown. As it is expected, by increasing the stage inlet GVF, the concentration value at the impeller outlet increases. The concentration values at impeller outlet are lower in the second stage than the first stage. The lower concentration at the second stage is due to higher pressure and higher turbulence and mixing that is generated by the second impeller.

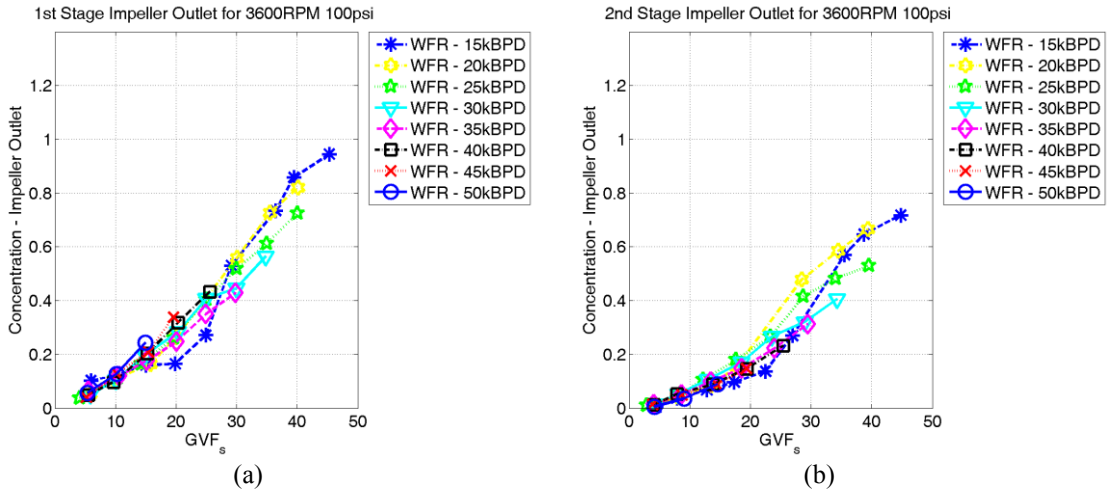

Figure 4-30: Impeller outlet concentration versus the stage inlet GVF for (a) the first stage and (b) second stage at 3600 RPM and 100 psig pump inlet pressure

According to the obtained concentration values, slip ratio of the mixture at the outlet of the impeller can be calculated by this assumption that no recirculation occurs in this location. The slip ratio is obtained by Equation (4.12),

$$s = \frac{V_g}{V_l} = \left(\frac{\lambda_{g_s}}{1-\lambda_{g_s}}\right)\left(\frac{\rho_{g_s}}{\rho_{g_c}}\right)\left(\frac{1-c}{c}\right) \tag{4.12}$$

In Figure 4-31 (a) and (b), the slip ratio at the stage's impeller outlet for the first and second stages of the pump for different stage inlet GVF at 3600 RPM and 100 psig pump inlet pressure are shown. By increasing the inlet stage GVF, slip ratio decreases which is equivalent to the higher velocity difference between the liquid and gas phases.

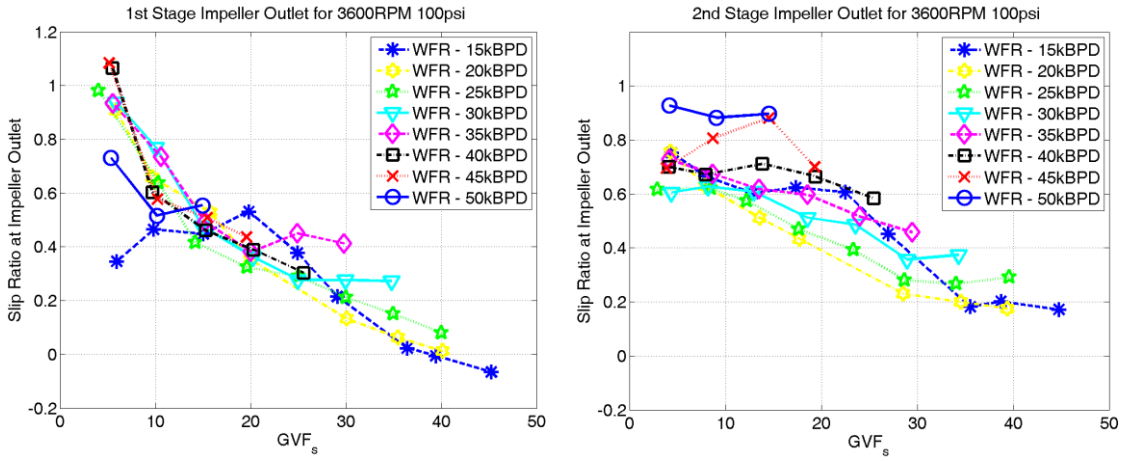

Figure 4-31: Impeller outlet slip ratio versus the stage inlet GVF for (a) the first stage and (b) second stage at 3600 RPM and 100 psig pump inlet pressure

The head degradation coefficient (HDC) is defined by the following equation,

$$HDC = 1 - a_1 \left(\frac{c}{\lambda_{g_s}}\right)^{0.75} \left(\frac{Q_L}{Q_{bep,s}}(s-1)\right)^2, \qquad (4.13)$$

$$a_1 = 0.04169$$

In Figure 4-32 (a) and (b), each stage's HDC for different stage inlet GVF at 3600 RPM and 100 psig pump inlet pressure are shown. The values of HDC approach the unity from the first stage to the second stage. Head degradation equal to one corresponds to the condition which no head degradation within the pump stage occurs.

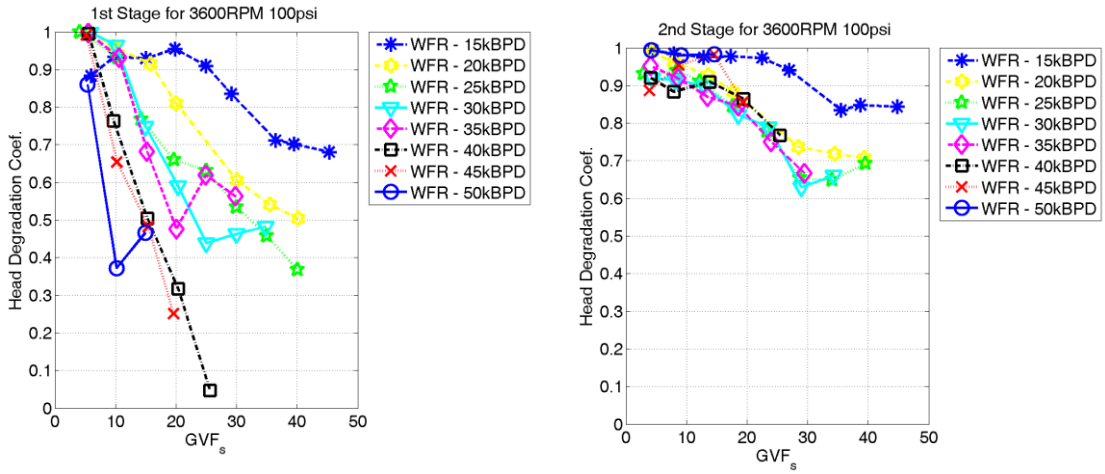

(a) (b)

Figure 4-32: Stage Head Degradation Coefficient versus the stage inlet GVF for (a) the first stage and (b) second stage at 3600 RPM and 100 psig pump inlet pressure

Assuming the third stage's HDC value to be equal to unity, the theoretical head ratio for the second stage and first stage are calculated using the 3rd stage's curved fit head ratio (obtained from Figure 4-6 (a)) which is plotted in Figure 4-33 and the curved fit equation is given in Equation (4.14).

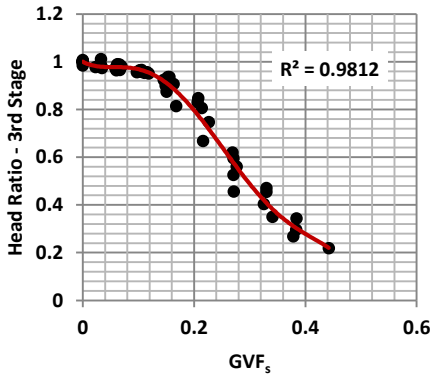

Figure 4-33: 3rd stage's curved fit head ratio – 3600 RPM and 100 psig inlet pressure

$$Head\ Ratio_3 = -475.62GVF_s^5 + 571.07GVF_s^4 - 222.92GVF_s^3 + 27.013GVF_s^2 - 1.3144GVF_s + 1.0003 \quad (4.14)$$

The equation to calculate the theoretical head ratio for the first and second stages is given as,

$$Head\ Ratio_{th_n} = Head\ Ratio_3 \times HDC \quad (4.15)$$

The plots for the calculated theoretical head ratios are shown in Figure 4-34 (a) and (b).

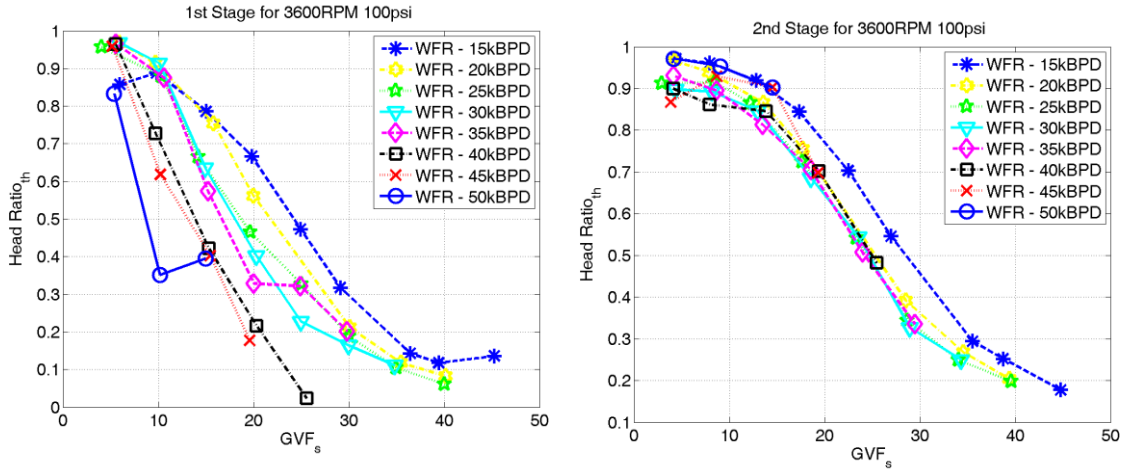

(a) (b)

Figure 4-34: Theoretical Head Ratio versus the stage inlet GVF for (a) the first stage and (b) second stage at 3600 RPM and 100 psig pump inlet pressure

To compare the results calculated by theoretical head ratios and obtained by experimental head ratios, the parameter, $(HR_{th} - HR_{exp})/HR_{exp}$, is used. The values of this parameter for different water flow rates and inlet gas volume fractions are shown for the first stage and second stage in Figures Figure 4-35 (a) and (b) respectively.

In the definition of Head Degradation Coefficient (HDC), Equation 4-10, the employed slip ratio was defined for non-recirculating regions. One of the primary reasons in deviation of the results from zero is considered to be due to the existence of the recirculation zone at the exit of the impeller. As the result of centrifugal forces and due to the presence of a bend at this location in the primary flow path, the existence of the recirculation region in this location is possible. However, pressure drops associated with the recirculation zone are not considered in Equation (4.13).

According to the Figure 4-35 (a), the value of the $(HR_{th} - HR_{exp})/HR_{exp}$ exceeds 0.75 in high water flow rates 35, 45 and 50kBPD in their corresponding high gas volume fractions. In these operating conditions, a larger and stronger recirculation region is expected.

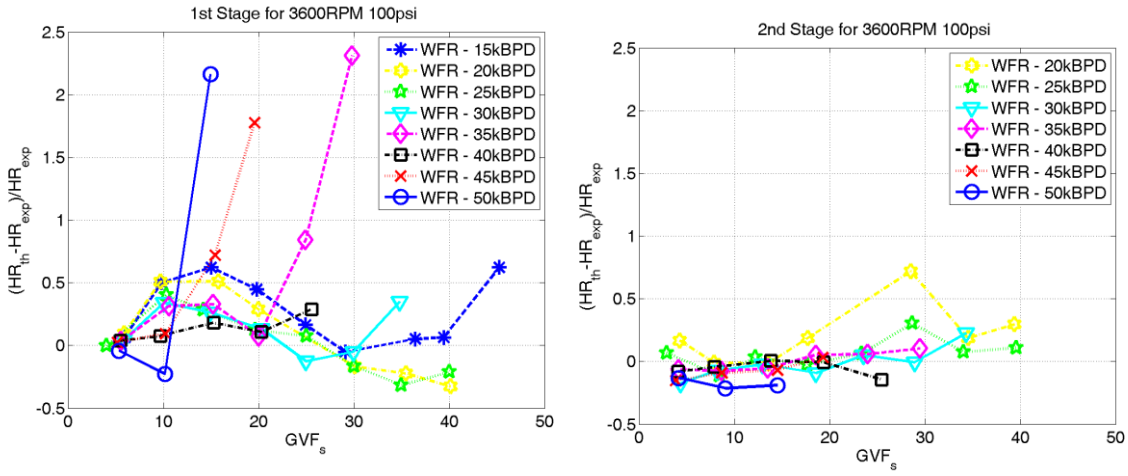

(a) (b)

Figure 4-35: Comparison between the results from Theoretical Head Ratio (HR_{th}) and Experimental Head Ratio (HR_{exp}) versus the stage inlet GVF for the first stage (a) and second stage (b) at 3600 RPM and 100 psig pump inlet pressure

In Figure 4-35 (b), the value of the $(HR_{th} - HR_{exp})/HR_{exp}$ for the second stage approaches zero except in 15 kBPD water flow rate. In this low water flow rate, high pulsation in the fluid flow in second stage was observed. The results from this operating condition were removed from Figure 4-35 (b) due to non-similar flow condition.

According to the assumptions made in this section the value of $(HR_{th} - HR_{exp})/HR_{exp}$ for the third stage was considered to be equal to zero.

4.3. CFD Erosion Simulation

Numerical erosion study that was carried out on the first and second stages of the ESP-WJE1000 manufactured by Baker Hughes Company is covered in this section. Computational fluid analysis was performed for pure water and water-sand mixture with 2 gr/lit sand concentration and single sand particle size of 100 mesh size. CFD analysis was implemented for the BEP of the pump at 3600 RPM. The results of the computational analysis were validated with the experimental results obtained from eroded surfaces obtained from the experimental erosion study performed for 129 hours of operation of the ESP pump at Turbomachinery Laboratory at Texas A&M University.

The 3D-CAD fluid model of the non-eroded stage was provided by 3D laser scanning. The erosion depth for the first and second stages was measured and provided by utilizing clay casting measurements and 3D laser scanning measurements respectively.

The key parameters influencing the erosion process on the main flow path of the pump were considered. An empirical-numerical model to predict the erosion rate on the centrifugal pumps in terms of the key parameters was obtained utilizing the erosion depth measured from experimental results.

A single stage of the pump was meshed using complete 3D hexahedral elements. The grid independency was performed to study the effects of the number of nodes on the simulation results. The grid independency study results are summarized in Table 4-3 and the

corresponding simulation results are shown in Figure 4-36 (a-c). The maximum y^* value of 300 is recommended for the standard wall function for turbulent flow simulations. The maximum of 1.5% dependency to number of nodes for torque values was captured. The 6.79 million node meshed model was chosen and exported to ANSYS Fluent 13.0 as the CFD solver.

Table 4-3: Grid independency study results in single phase flow at BEP

	Model 1	Model 2	Model 3	Model 4
y^* Value	<290	<270	<255	<130
Total No. of Nodes, Million	6.79	6.83	6.94	8.50

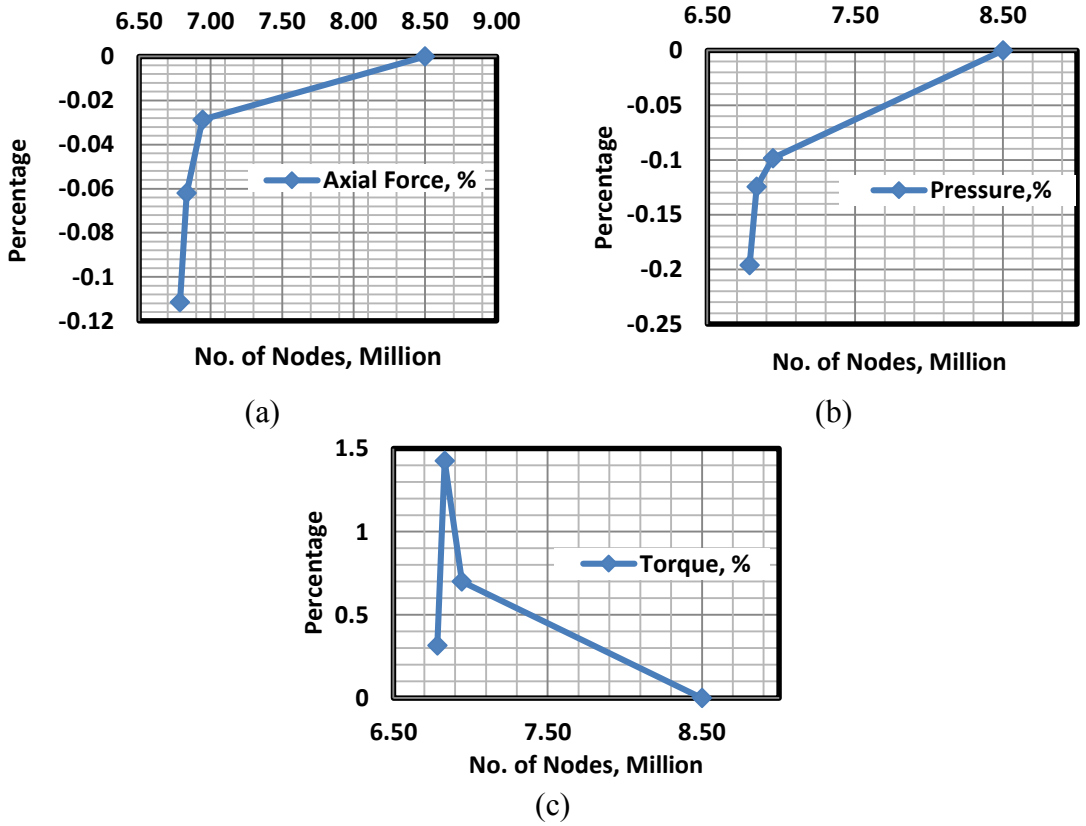

Figure 4-36: Simulation results of grid independency study for (a) axial force, (b) pressure and (c) torque

4.3.1. CFD Simulation Results

Single phase flow study on the first and second stages of the ESP-WJE1000 pump was performed at 331 m^3/hr (BEP) and 3600 RPM to validate the CFD simulation results for single phase. The results of the simulation were compared with the available experimental results obtained from experimental tests on the three stages of the pump. The available experimental results are based on the differential pressure measurements on the entire three stages. Therefore, experimental single stage pressure rise was considered to be 1/3 of the total pressure rise across the pump.

In Table 4-4, the comparison between experimental and computational stage pressure rise results for single phase flow simulation are summarized for the BEP and 3600 RPM.

Table 4-4: Comparison between experimental and computational stage pressure rise results, BEP and 3600 RPM

Method	Stage Pressure Rise, psi	Error, %	Uncertainty, %
CFD-1st stage	66.7	2.6	-
CFD-2nd stage	65.1	0.1	
Experimental	65	-	0.2

Due to the difference in flow conditions at the exit of the first stage (velocity, turbulence kinetic energy, …), the performance of the second stage is different. The slight difference in pressure measurements can be seen in Figure 4-37 (a, b).

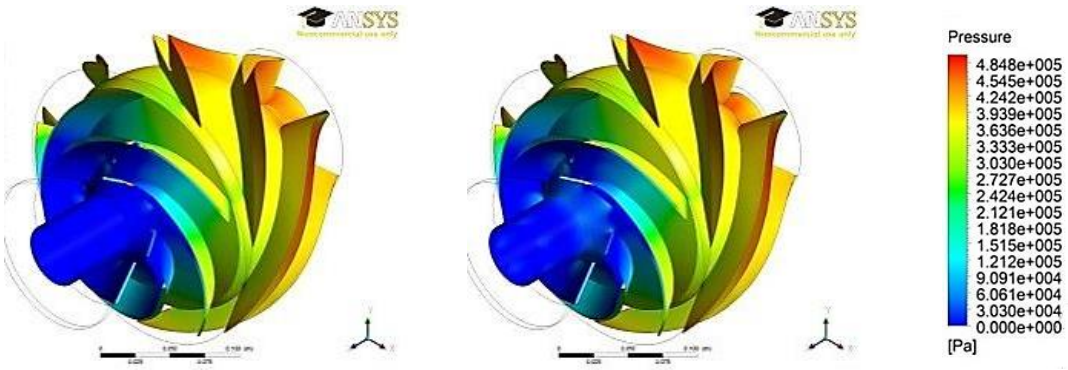

(a) (b)

Figure 4-37: Single phase pressure contour for (a) the first stage and (b) second stage ESP

In Figure 4-38, the water streamlines for the first and second stage for different span-wise locations are shown. In this figure, from left to right flow streamlines for inlet, impeller and diffuser are shown. Due to the flow condition at the outlet of the first diffuser, the inlet streamlines for the first and second stages are different. The velocity angles at the inlet of the second stage deviates the most near the shroud of the impeller in comparison with the first stage. One of the primary parameters in causing this difference is the recirculation region present in the diffuser section which moves toward the stage exit from hub to shroud.

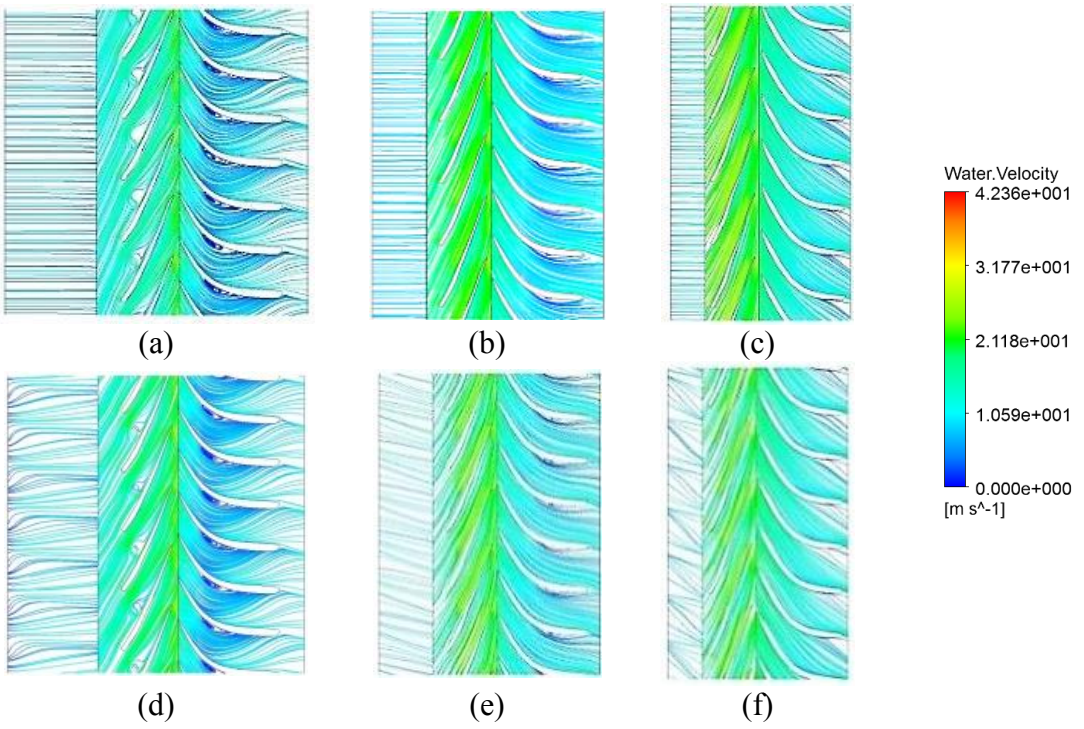

Figure 4-38: Water Streamlines for (a) the 1st Stage – Span: 0.1, (b) 1st Stage – Span: 0.5, (c) 1st Stage – Span: 0.9, (d) 2nd Stage – Span: 0.1, (e) 2nd Stage – Span: 0.5 and (f) 2nd Stage – Span: 0.9

In the two-phase flow simulations results, this behavior at the outlet of the first stage causes a non- homogenous distribution of sand concentration (Figure 4-39 (a)) and non-uniform distribution of the turbulence kinetic energy (Figure 4-39 (b)) at the exit of the first diffuser.

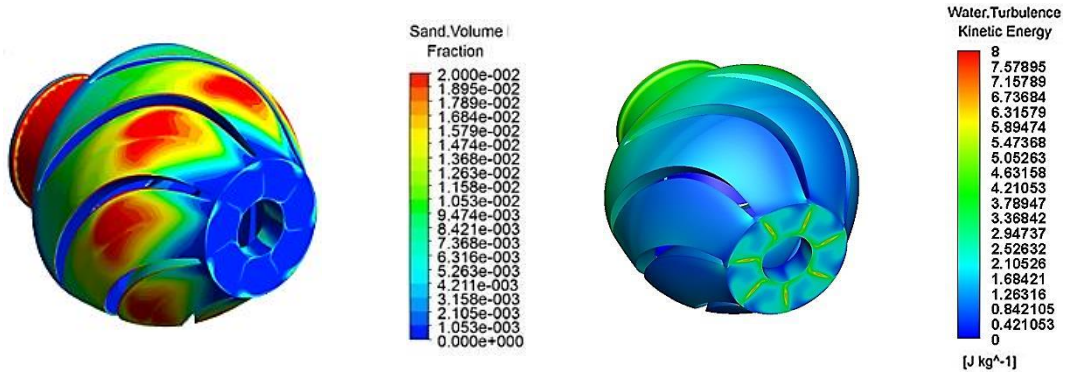

(a) (b)

Figure 4-39 : (a) Distribution of sand volume fraction and (b) water turbulence kinetic energy the first stage outlet diffuser

The key parameters influencing the erosion process on the main flow path of the pump were identified to be turbulence kinetic energy, local sand concentration and near wall relative sand velocity. Their importance was obtained by comparing the simulation results with the location of erosion depth obtained from the experimental erosion tests performed for 129 hours of operation on the ESP pump at Turbomachinery Laboratory at Texas A&M University. Turbulence provides transport perpendicular to the main flow stream. For the particles to reach the wall, adequate amount of turbulent kinetic energy is required. In Figure 4-40, distributions of the turbulence kinetic energy and sand volume fraction on the solid walls for the first and second stage of the pump are shown.

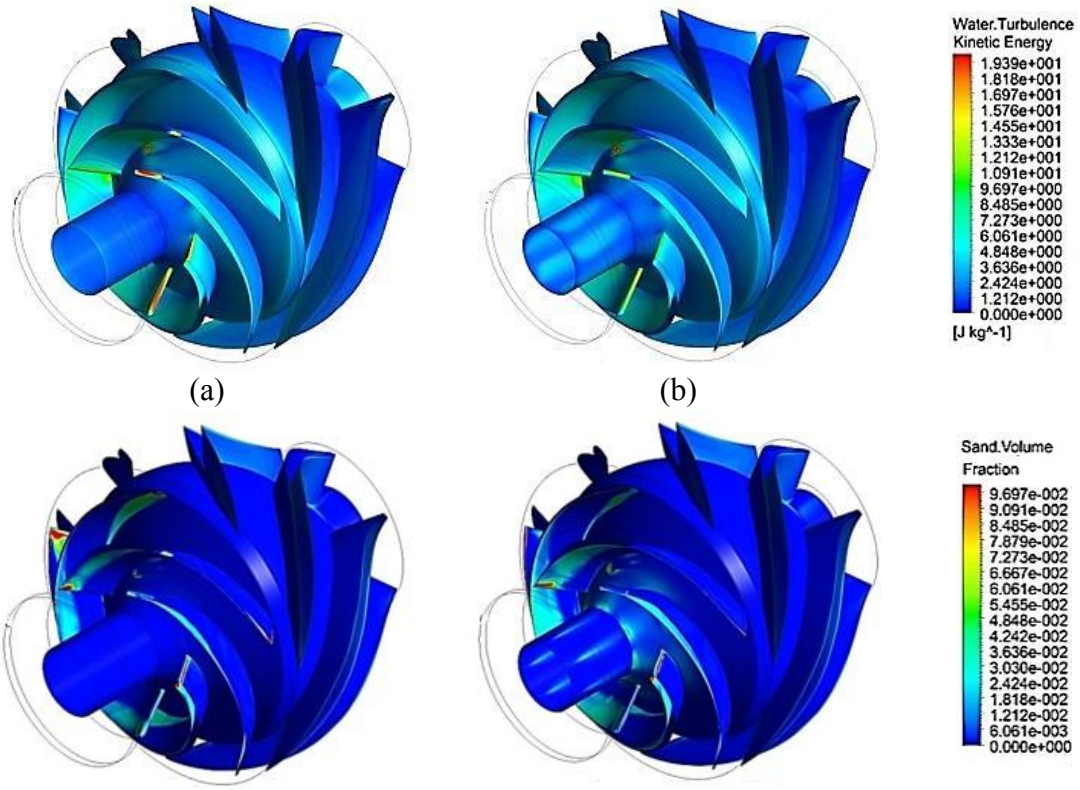

Figure 4-40: (a) Turbulence kinetic energy for the first stage, (b) turbulence kinetic energy for the second stage, (c) sand volume fraction for the first stage and (d) sand volume fraction for the second stage

In Figure 4-41 and Figure 4-42, the water turbulence kinetic energy and sand volume fraction in different span-wise locations on each stage's cascade are shown. According to these figures, sand volume fraction at the pressure side of diffuser blades is higher. In contrast with the uniform sand concentration at first stage inlet (Figure 4-42 (a-c)), for the second stage the high concentration jets enter the next pump stage with varying angle from hub to the shroud as it is shown in Figure 4-42 (d-f).

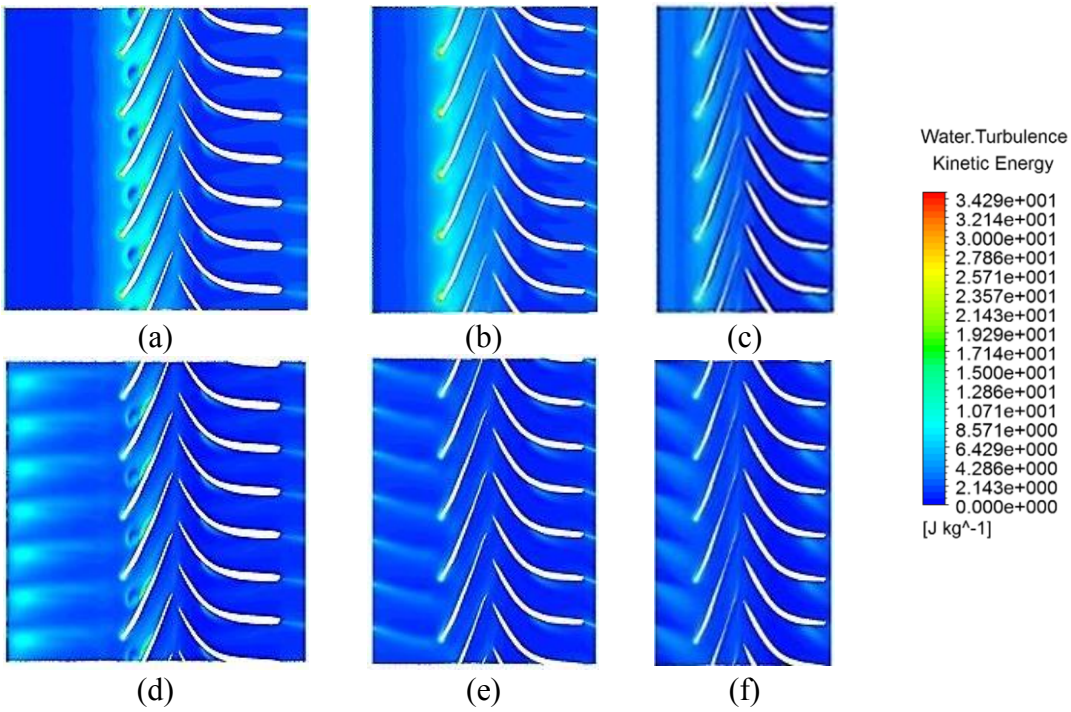

Figure 4-41: Turbulence kinetic energy for (a) the 1st Stage – Span: 0.1, (b) 1st Stage – Span: 0.5, (c) 1st Stage – Span: 0.9, (d) 2nd Stage – Span: 0.1, (e) 2nd Stage – Span: 0.5, and (f) 2nd Stage – Span: 0.9

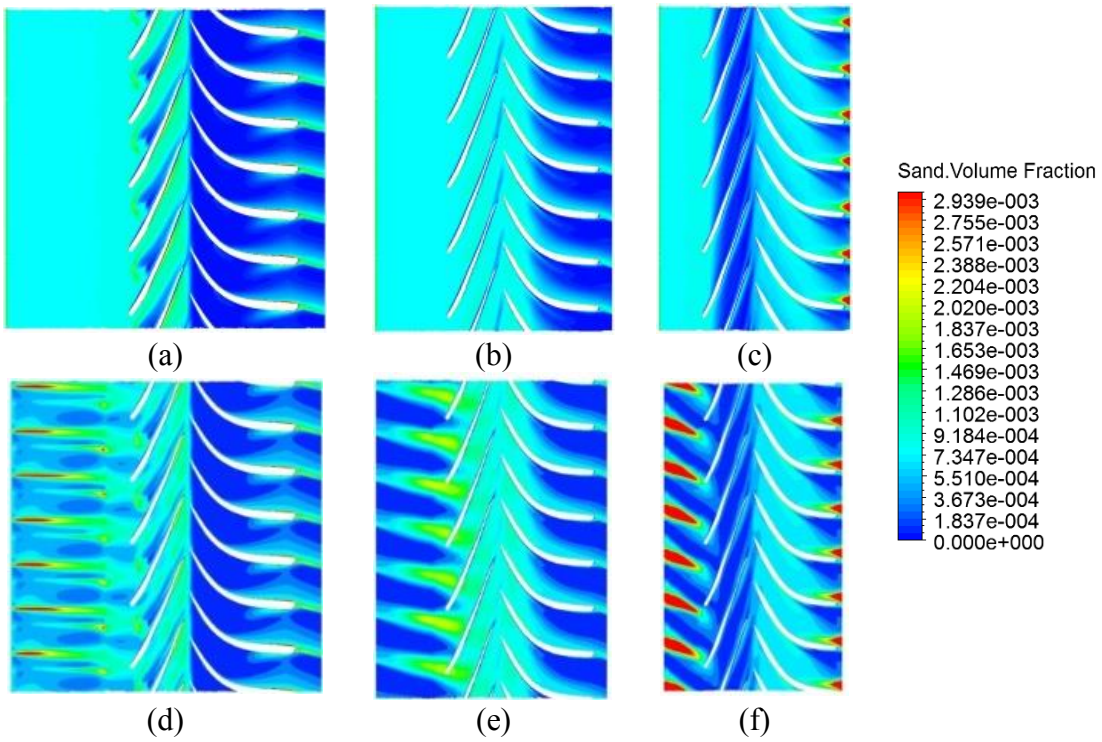

Figure 4-42: Sand concentration for (a) the 1st Stage – Span: 0.1, (b) 1st Stage – Span: 0.5, (c) 1st Stage – Span: 0.9, (d) 2nd Stage – Span: 0.1, (e) 2nd Stage – Span: 0.5, and (f) 2nd Stage – Span: 0.9

4.3.2. Erosion Modeling

A new empirical-numerical model to predict the erosion rate on the ESP pump in terms of the key parameters was obtained iteratively by comparing the erosion factor with the erosion rate measured from experimental results (Equation (4.16)),

$$EF = (\alpha_s)^{0.08} \left(\frac{V_s}{V_{s_0}}\right)^{0.07} \left(\frac{k_w}{k_{w_0}}\right)^{1.25} \tag{4.16}$$

Using the results computed from erosion factor, erosion rate is obtained employing the measured erosion depth from experimental results. The curved-fit plot for the erosion factor and experimental erosion rate is shown in Figure 4-43.

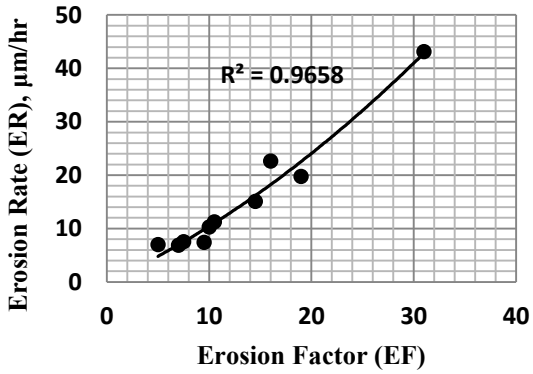

Figure 4-43: Erosion rate for the computed erosion factor values

In Equation (4.17), the polynomial which corresponds to Figure 4-43 is given,

$$ER\ (\mu m/hr) = A.EF^2 + B.EF \quad (4.17)$$

A= 0.0163, B=0.8774

The computed erosion rate for two stages of the pump using Equations (4.16) and (4.17) are shown in Figure 4-44 and Figure 4-45.

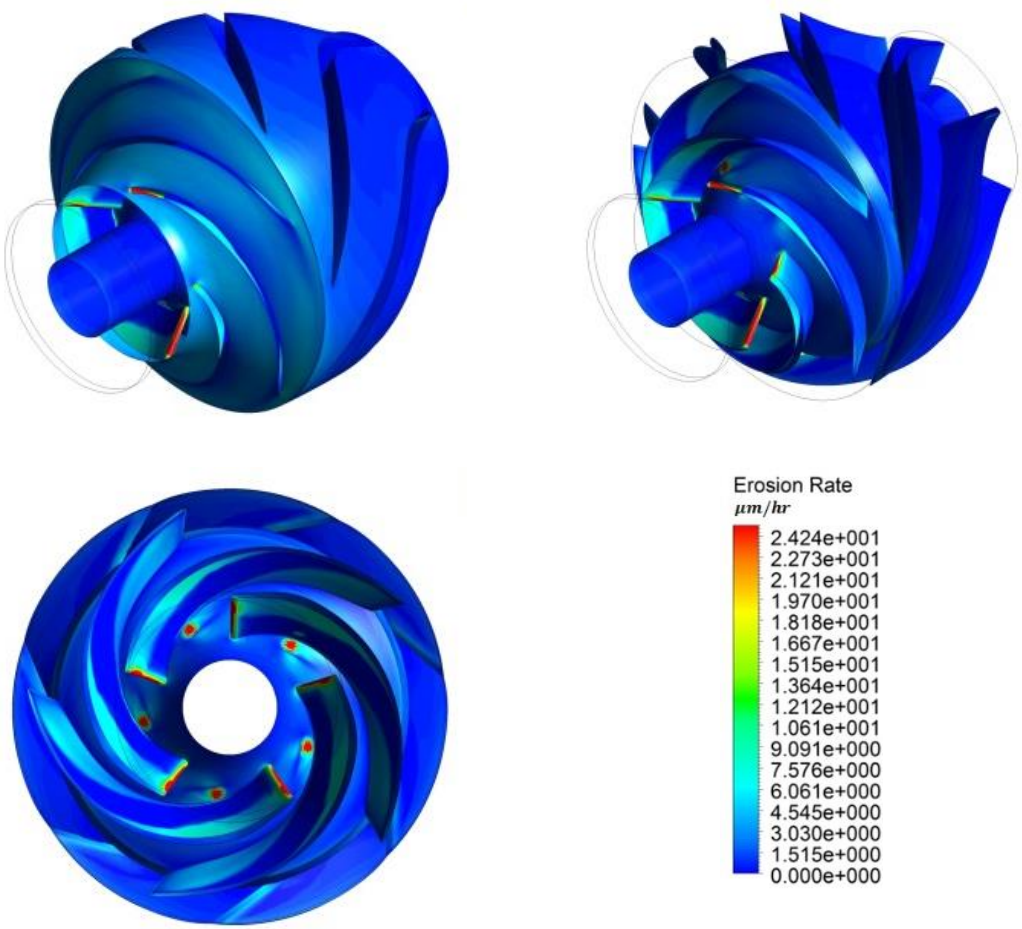

Figure 4-44: Computed erosion rate on 1st stage from diffenrent views

According to Figure 4-46, for the first stage on the leading edge of the impeller maximum erosion occurs near to the shroud whereas in the second stage, it occurs near to the hub. At these locations, the erosion rate on the first stage is higher in comparison with the second stage. However, the erosion around the balance holes on the suction side of the impeller blade and hub is higher in the second stage than the first stage. Similarly, the erosion rate on the hub close to the leading edge is higher in the second stage than the first

stage. These results presented in Figure 4-46, represents a good agreement between experimental results and computational results.

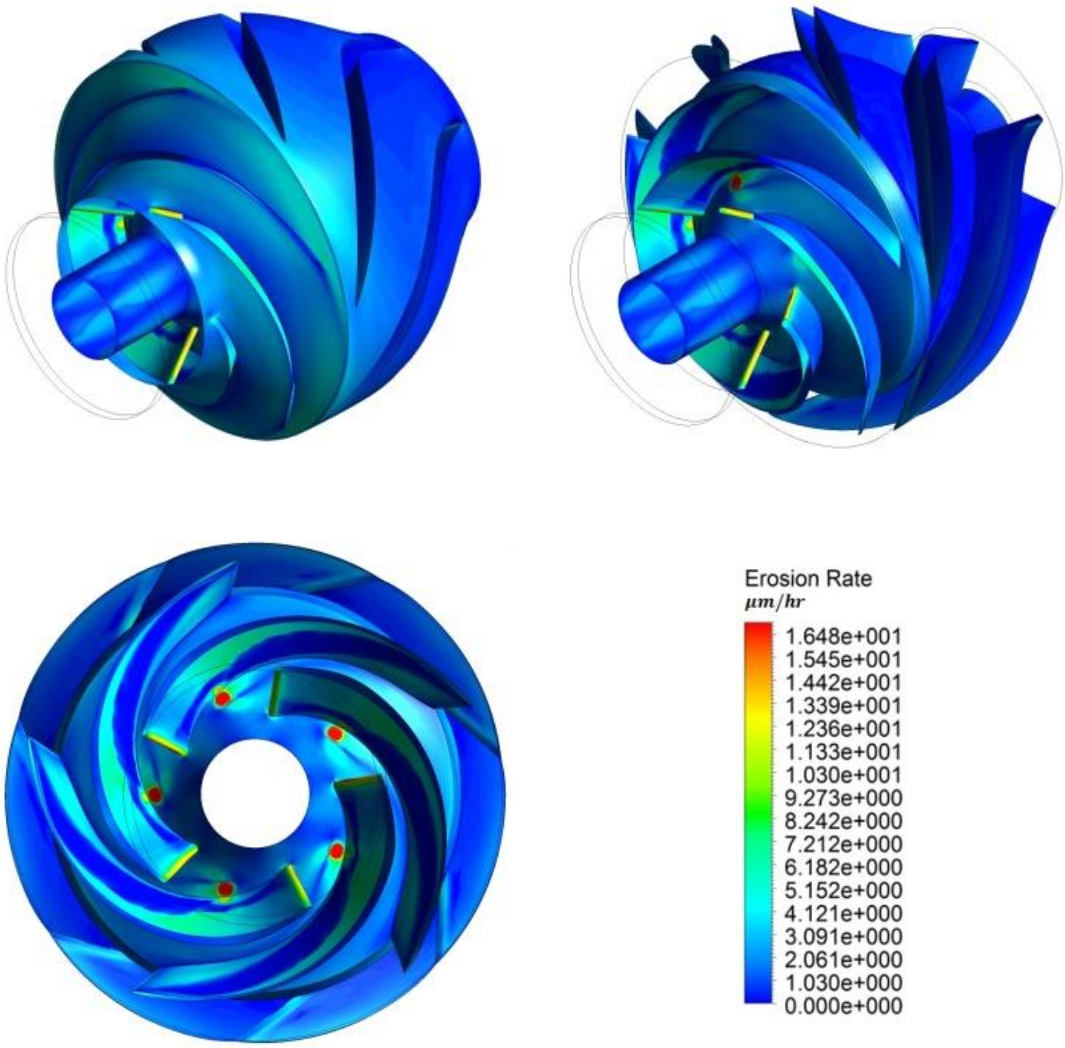

Figure 4-45: Computed erosion rate on 2nd stage from diffenrent views

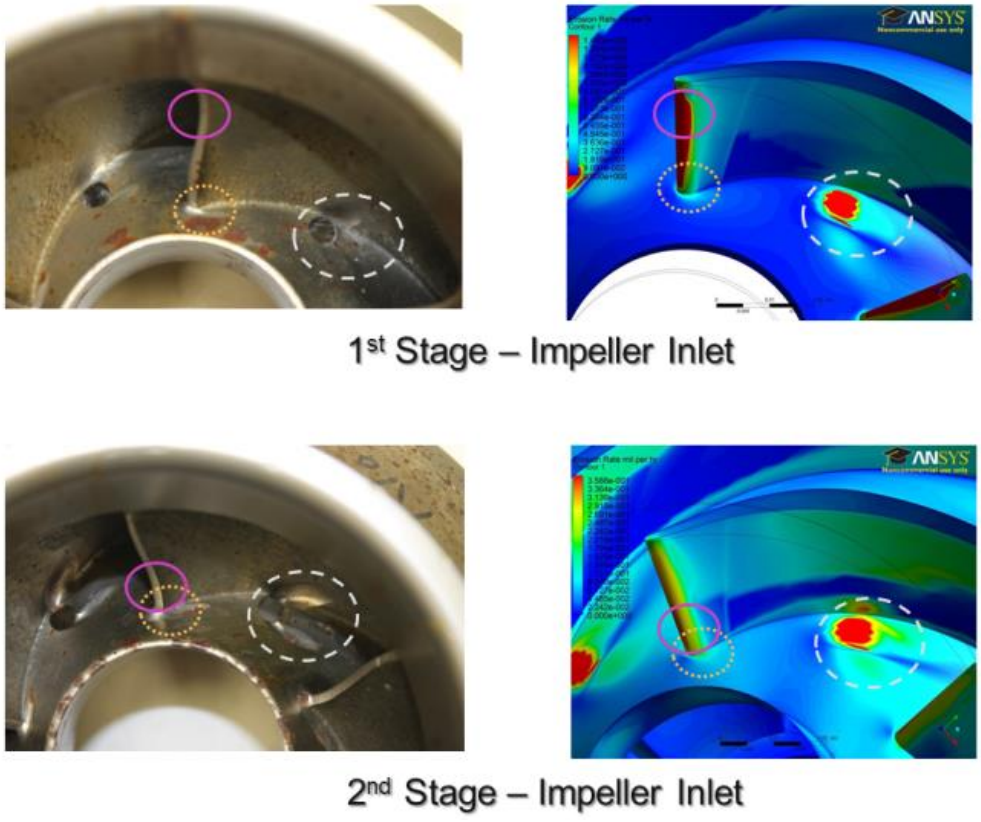

Figure 4-46: Comparison between the computed erosion rates with the eroded locations in the first and second impellers

The comparison of the results shown in Figure 4-46 represents the dominant effect of turbulence kinetic energy on the erosion rate. Similarly, in Equation (4.16) due to the higher power of the term associated with the turbulence kinetic energy the dominant effect of this parameter is clear. In fact, at the location with higher turbulence kinetic energy, noticeable erosion on the pump parts was obtained. Therefore, turbulence kinetic energy is a good indicator to qualitatively predict the location of erosion occurrence in pumps.

4.4. Recommended MVP and Regular ESP Stages Arrangement in Oil Fields

MVP stages are essentially employed and installed in series at the inlet of multistage ESP stages to provide turbulence and as the result homogenous flow condition for the regular ESP stages in order to increase their gas handling capacity. ESP pumps with non-homogenous two-phase inlet conditions suffer from surging and gas lock. To find the proper and efficient arrangement of MVP and ESP stages, some parameters are needed to be considered,

- Flow homogeneity and its degradation in downstream ESP stages

- Erosion in MVP and ESP stages

Employing at least two stages of the MVP pump can provide relatively homogenous flow condition according to the discussions given in sections 4.2.2, 4.1.4 and 4.3. Therefore, to increase the gas handling capacity of ESPs at least two stages of the MVP-ESP pump is required to be installed at the inlet of ESPs. However, the relatively homogenous flow provided by MVP stages degradates in the downstream ESP stages. Therefore, to maintain the flow homogeneity in multistage system, MVP stages can be placed intermittently within the ESP stages. According to the preferred operating conditions, the number of ESP stages can vary. It means for higher gas volume fractions, a lower number of stages between MVP stages need to be placed.

On the other hand, the MVP stages are more sensitive to erosion than regular ESP pumps. According to the discussion given in section 4.4.2 turbulence is the main cause of erosion in ESP pumps. In MVP pumps, higher turbulence is generated which plays an important role in homogenizing the flow, therefore more erosion can be observed in these pumps specifically on their first stages.

As a result, for long life operation of multistage MVP and ESP pumps, more than two stages of MVP is recommended to be used at inlet of ESPs for long life efficient performance.

5. CONCLUSION AND RECOMMENDATIONS

In this study, experimental study on the flow behavior in a MVP-G470 pump and computational study on the erosion process in an ESP-WJE1000 pump were carried out. Entire MVP pump performance for different operating conditions was performed for a mixture of water and air. Detail study of a stage performance was done on the first and second stage of the pump using conductivity and pressure measurements accompanied by high speed visualization.

Overall MVP pump performance demonstrated the functionality of inlet pressure and rotating speed on the pump performance with the dominant effect of rotating speed.
Stage by stage head analysis in MVP pump demonstrated very slight increase in head ratio across the third stage in higher inlet pressures and rotating speeds. For a given stage inlet GVF, a correlation was found to obtain the stage head ratio for the third stage and other downstream stages.

Utilizing ERT system on the two stages of the MVP-ESP pump, the flow behavior in diffuser sections of the pump were studied. By conductivity measurement technique, two effective regions with high influence on the two-phase performance of the pump were identified. The locations of the regions with high slip velocity and recirculation zone were determined to be at the inlet of diffuser ($x/L_s = 4/9$) and 7/9th of the stage length. According to the pressure distribution measurements in these two locations a common pressure drop in both the stages was observed. The existence of the recirculation zone was

verified by high speed photography technique in this region. Bubble size and velocity in this location for a specific operating condition was obtained. Also, the concentration distribution and the behavior of both these regions were studied for different operating conditions of the pump.

To study the erosion process on an ESP-WJE1000 pump, CFD simulations on the first and second stages of pump were performed. The key parameters affecting the erosion process on the main flow path of the pump including the balance holes were considered. Two-phase flow numerical simulation was conducted using Eulerian - Granular scheme in ANSYS-Fluent. An empirical-numerical model to predict erosion rate on the centrifugal pumps in terms of the turbulence kinetic energy, local sand volume fraction and near wall relative sand velocity was introduced. The results were correlated and validated with the eroded surfaces of the ESP pump after being eroded in 129 hours of operation.

In this study, the performance of the MVP pump was studied in detail. Since, this pump typically is installed in series with conventional ESP pumps, the combined performance of these two stages is recommended to be studied in detail.

In this investigation, the initial stage was found to play mainly the role of homogenizer with low performance in pumping in comparison with other two stages. The performance of the first stage and second stage was correlated to the performance of the third stage. The correlation found in this study is recommended to be improved specifically for the first stage by including the other contributing physics in the first stage performance. One

parameter affecting the deviation in correlation was predicted to be large recirculation zones within the first stage which needs to be validated.

Also, since, the erosion rate was observed to rise by the introduction of air into the pump, a three phase study on the erosion process within the ESP stages is recommended. Since, erosion occurs in the first stage was found to be higher in ESP pumps, in the case of installing intermittent MVP stages within ESP stages, erosion study in these MVP stages is required to be compared to the erosion rate in first stages.

REFERENCES

Ahmed, W. H. and B. I. Ismail (2008). "Innovative Techniques for Two-Phase Flow Measurements." Recent Patents on Electrical & Electronic Engineering (Formerly Recent Patents on Electrical Engineering) **1**(1): 1-13.

Barrios, L. (2007). Visualization and Modeling of Multiphase Performance Inside An ESP, PhD Dissertation, University of Tulsa, Tulsa, Okla.

Bitter, J. (1963). "A Study of Erosion Phenomena Part I." Wear **6**(1): 5-21.

Butler, J. E. (1998). Tomographic Imaging for the Visualization of Multiphase Flows, PhD Dissertation, University of Texas at Austin, Austin, Texas.

Cirilo, R. (1998). Air-Water Flow Through Electric Submersible Pumps, PhD Dissertation, University of Tulsa, Department of Petroleum Engineering, Tulsa, Okla.

Cody, G., D. Goldfarb, G. Storch Jr and A. Norris (1996). "Particle Granular Temperature in Gas Fluidized Beds." Powder Technology **87**(3): 211-232.

Da Silva, M. J. (2007). "A Novel Needle Probe Based on High-Speed Complex Permittivity Measurements for Investigation of Dynamic Fluid Flows." IEEE Transactions on Instrumentation and Measurement **56**(4): 1249.

Dickin, F. (1996). "Electrical Resistance Tomography for Process Applications." Measurement Science and Technology **7**(3): 247.

Ding, J. and R. W. Lyczkowski (1992). "Three-Dimensional Kinetic Theory Modeling of Hydrodynamics and Erosion in Fluidized Beds." Powder Technology **73**(2): 127-138.

Duran, J. (2003). Pressure Effects on Esp Stages Air-Water Performance, PhD Dissertation, University of Tulsa, Tulsa, Okla.

Dyakowski, T. (2005). "Dual-Modality Probe for Characterization of Heterogeneous Mixtures." IEEE Sensors Journal **5**(2): 134.

Estevan, V. (2002). A Phenomenological Analysis about Centrifugal Pump in Two-Phas Flow Operation. Campinas: Faculdade De Engenharia Mecanica, PhD Dissertation, Universidade Estadual De Campinas, Brazil.

Finnie, I. (1960). "Erosion of Surfaces by Solid Particles." Wear **3**(2): 87-103.

Fujie, H., & Yamanouchi, A. (1985). "A Study on Performance of Centrifugal Pumps Driven in Two-Phase Flow." Nuclear Engineering And Design, 85(3), 345-352.

Furuya, O. (1985). "An Analytical Model for Prediction of Two Phase (Non-Condensable) Flow Pump Performance." ASME Journal of Fluids Engineering **107**: 139-147.

Gamboa, J. (2009). Prediction of The Transition in Two-Phase Performance of An Electrical Submersible Pump, Proquest.

Gülich, J. F. (2008). Centrifugal Pumps, Springer.

Hench, J. E. (1972). "Two-Dimensional Diffuser Performance with Subsonic, Two-Phase, Air–Water Flow." Journal of Basic Engineering **94**(1): 105.

Kim, J. H. (1983). "Prespective of Two Phase Flow Pump Modeling for Nuclear Reactor Safety Analysis." Presented at Cavitation and Multiphase Flow Forum of ASME Conference.

Kirkland, K. (2013). Design and Fabrication of A Vertical Pump Multiphase Flow Loop, Master Thesis, Texas A&M University, Texas.

Lea, J. (1982). "Effect of Gaseous Fluids on Submersible Pump Performance." Journal of Petroleum Technology **34**(12): 2922.

Lyczkowski, R. and J. Bouillard (2002). "State-of-the-Art Review of Erosion Modeling In Fluid/Solids Systems." Progress In Energy and Combustion Science **28**(6): 543-602.

Mikielewicz, J. (1978). "A Method for Correlating the Characteristics of Centrifugal Pumps In Two-Phase Flow." Journal of Fluids Engineering **100**(4): 395.

Mitsukiyo, M. and M. Kiyoshi (1974a). "Effects of Entrained Air on The Performance of A Centrifugal Pump : 1st Report, Performance and Flow Conditions." Bulletin of JSME **17**(110): 1047-1055.

Mitsukiyo, M. and M. Kiyoshi (1974b). "Effects of Entrained Air On The Performance of Centrifugal Pumps : 2nd Report, Effects of Number of Blades." Bulletin of JSME **17**(112): 1286-1295.

Mitsukiyo, M. and M. Kiyoshi (1976). "Effects of Running Clearance of Semi-Open Impeller Pumps Under Air Admitting Conditions." Bulletin of JSME **19**(136): 1141-1148.

Munholand, L. (2005). "Comparison of Four Conductive Needle Probe Designs for Determination of Bubble Velocity and Local Gas Holdup." Review of Scientific Instruments **76**(9): 095101.

Ogawa, S., A. Umemura and N. Oshima (1980). "On The Equations of Fully Fluidized Granular Materials." Zeitschrift Für Angewandte Mathematik Und Physik ZAMP **31**(4): 483-493.

Patel, B. R. and P. W. Runstadler (1978). Investigations Into the Two-Phase Behavior of Centrifugal Pumps. ASME Symposium on Poliphase Flow In Turbomachinery. San Fracisco, USA.

Pessoa, R. and M. Prado (2001). Experimental Investigation of Two-Phase Flow Performance of Electrical Submersible Pump Stages. SPE Annual Technical Conference and Exhibition, Society of Petroleum Engineers.

Pessoa, R. E. A. (1999). Tapered Pump Experimental Tests with Light and Heavy Oil In PDV INTEVEP Field Laboratory. 1999 SPE ESP Workshop. Texas.

Poullikkas, A. (2003). "Effects of Two-Phase Liquid-Gas Flow on The Performance of Nuclear Reactor Cooling Pumps." Progress In Nuclear Energy **42**(1): 3.

Rasmy Marsis, E. (2012). CFD Simulation And Experimental Testing of Multiphase Flow Inside The MVP Electrical Submersible Pump, PhD Dissertation, Texas A&M University, Texas.

Romero, M. (1999). An Evaluation of An Electric Submersible Pumping System for High GOR Wells, PhD Dissertation, University of Tulsa, Tulsa, Okla.

Runstadler Jr, P. and F. Dolan (1978). Two-Phase Flow Pump Data for A Scale Model NSSS Pump. ASME Symposium on Polyphase Flow In Tubomachinery, San Fransisco.

Runstadler, P. (1976). "Review and Analysis of State-of-the-Art of Multiphase Pump Technology." Electric Power Research Institute, Palo Alto, California, Rep. NP-159.

Sachdeva, R. (1988). Two-Phase Flow Through Electric Submersible Pumps, PhD Dissertation, University of Tulsa, Tulsa, Okla.

Schleicher (2008). "Local Void and Temperature Measurements for Transient Multiphase Flows." IEEE Transactions on Instrumentattion and Measurement **57**(2).

Sekoguchi, K., Takada, S., and Kanemori, Y. (1984). "Study of Air-Water Two-Phase Centrifugal Pump By Means of Electric Resistivity Probe Technique for Void Fraction Measurement; First Report, Measurement of Void Fraction Distribution In A Radial Impeller." Bulletin of JSME **27**(227): 227-213, 931-938.

Tarpley, B. A. (1984). "Head Loss Due To Gas In Submersible Pump Applications." Texas Tech. University Report for Amoco Production Research, Tulsa, Okla.

Tavoularis, S. (2005). Measurement In Fluid Mechanics, Cambridge University Press.

Uga, T. (1972). "Determination of Bubble-Size Distribution In A BWR." Nuclear Engineering and Design **22**(2): 252.

Wallis, G. B. (1969). "One-Dimensional Two-Phase Flow." New York: McGraw-Hill.

Winks, R. (1977). "One-Third-Scale Air-Water Pump Program: Test Program and Pump Performance." Babcock and Wilcox Co., Lynchburg, Va.(USA). Nuclear Power Generation Div.

Zakem, S. (1980). Analysis of Gas Accumulation and Slip Velocity In A Rotating Impeller. ASME Cavitation and Polyphase Flow Forum: 32-34.

Zegley, R. D. (1977). "First-Quadrant Two-Phase Flow In Centrifugal Pumps." Massachusetts Inst of Tech Cambridge Dept of Electrical Engineering.

Zhong, Y. And K. Minemura (1996). "Measurement of Erosion Due to Particle Impingement and Numerical Prediction of Wear In Pump Casing." Wear **199**(1): 36-44.

Zhou, D. (2010). "Simple Model of Electric Submersible Pump In Gassy Well." Journal of Petroleum Science & Engineering **70**(3-4): 204.

APPENDIX A

Water Turbine Flow Meter

Turbine Incorporated WM0600X6includes a magnetic pickup that puts out a 30mV to 3V sine wave signal. Accuracy in clean clear water is ±1%.

Turbine P/N	Repair Kit P/N	End Connection	Bore	GPM	BPD	MWP	K-Factor
WM0600x6	WK0600x6	6" x 6"	6"	250.0 - 2,500.0	8,571 - 85,710	3,700	6.31

APPENDIX B

Air Turbine Flow Meter

Model No	Maximum Linear Range(ACFM)	Nominal K-Factor (p-ACF)	Operating Pressure(psi)	Length mm (inch)	Approx Weight kg (lb)	End Connection MNPT (inch)	K-Factor
FTB-938	8 to 130	430	2000	111 (4.38)	3.5 (8)	1.5	402.399

APPENDIX C

ERT Sensor Design Recommended by ITS Co.

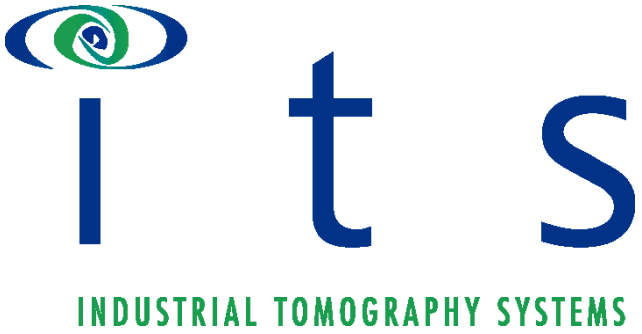

ERT Sensor Design Guidelines

Industrial Tomography Systems Ltd.

Speakers House

39 Deansgate

Manchester

M3 2BA

Tel. + 44 161 832 9297

Fax + 44 161 839 5195

Email sales.support@itoms.com

Web www.itoms.com

These drawings are for illustration only and are NOT to scale.

Electrical Resistance Tomography

The ITS P2+ ERT system typically operates with 16-electrode sensors. The electrodes must be in contact with the process fluid i.e. they must be on the inside wall of the process vessel.

Electrode Arrangement

The recommended electrode material for the majority of applications is 316L stainless steel. Electrode thickness should be minimised to eliminate disturbance to flow or the electrode should be mounted flush to the internal pipe wall. Stainless steel sheet of 1 mm thickness is widely available and is a suitable material.

The following electrode size is suitable for a 2 inch diameter acrylic column.

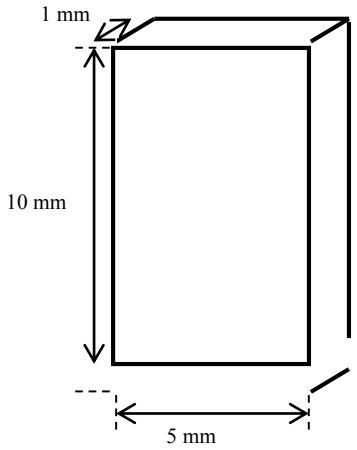

Sixteen 5 x 10 x 1 mm electrodes in each plane

Figure C-1 Electrode face dimensions

A method of attaching and sealing the electrodes suitable for vessels operating at low pressure is shown in figure C-2.

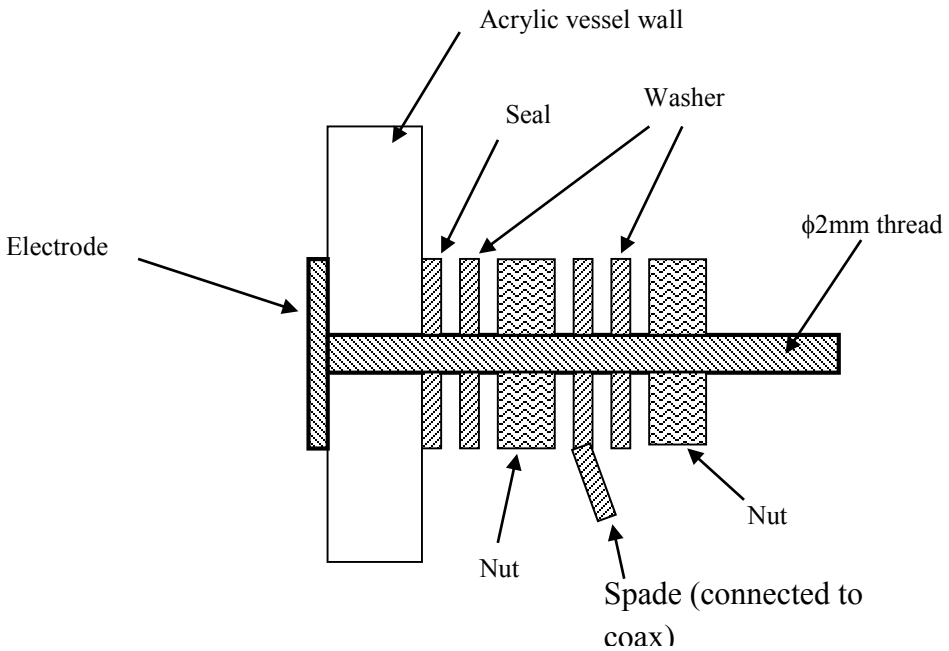

Figure C-2 Electrode fixing arrangement for low-pressure sensors

In order to fit the electrode flush with the vessel wall, a recess with dimensions to take the electrode should be machined on the inside wall of the pipe. The electrode face can be rolled prior to spot welding the threaded stud to let it take up the curvature of the pipe.

Photographs of an electrode for a low pressure sensor are shown in Figure C-3. A threaded stud has been spot welded to the back of the electrode face to provide a method of fastening to the vessel.

Figure C-3 Electrode for low pressure sensor

Figure C-4 shows a photograph of an electrode which incorporates an oring on the electrode stud. This design is suitable for sensors operating at moderate pressures.

Figure C-4 Electrode for moderate pressure sensor

A ground electrode is required. If there are 2 sensor planes then it should be positioned mid-way between the planes. For a single sensor plane it is recommend that the ground electrode is positioned 1 pipe diameter away from the measurement electrodes. The ground electrode can be the same dimensions as the measurement electrode.

Photographs of an acrylic vessel fitted with four electrode planes are shown in Figure C-5.

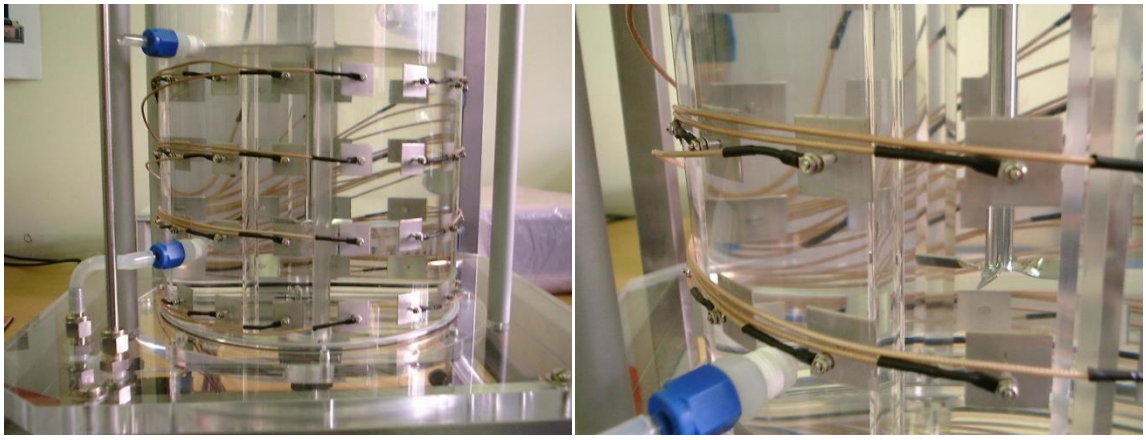

Figure C-5 Photograph of mixing vessel fitted with ERT sensors

1.2 Cable Assembly

The ERT electrodes (16 measurement + 1 ground) are connected to the ITS P2+ using Lemo connectors. B Series - Keyed Standard. www.lemo.co.uk

1.2.1. Electrode Connection

The coaxial cable screen should be cut back a few centimetres from the end of the cable. The coaxial cable core should be exposed and connected to a solder tag as shown in Figure 1-6. The cable and solder tag should be covered in heat shrink as shown in Figure C-5. It is recommended that an adhesive lined heat shrink is used to provide additional mechanical strength for this connection such as 6 mm adhesive lined heat shrink (RS stock no. 157-3795).

Figure C-6 Solder tag

Recommended dimensions for rectangle shape electrode for circular pattern of 16 electrodes around a pipe with different inner diameters are given in Table C.1.

Table C.1: Dimension of electrodes in a 16 circular pattern of electrodes around a pipe

	Electrode Size	
Pipe Dia., in	width, in	length, in
1.41	0.137795	0.590551
6	0.590551	0.787402
8.75	0.787402	0.787402

As a rule of thumb recommended by IT'S THE minimum distance between electrodes should follow the following equation,

$$\text{Minimum ditsnace between electrodes} = \frac{\text{Perimeter of vessel}}{2 \times \text{number of electrodes}} \quad \text{(C.1)}$$

APPENDIX D

Entire Pump Performance

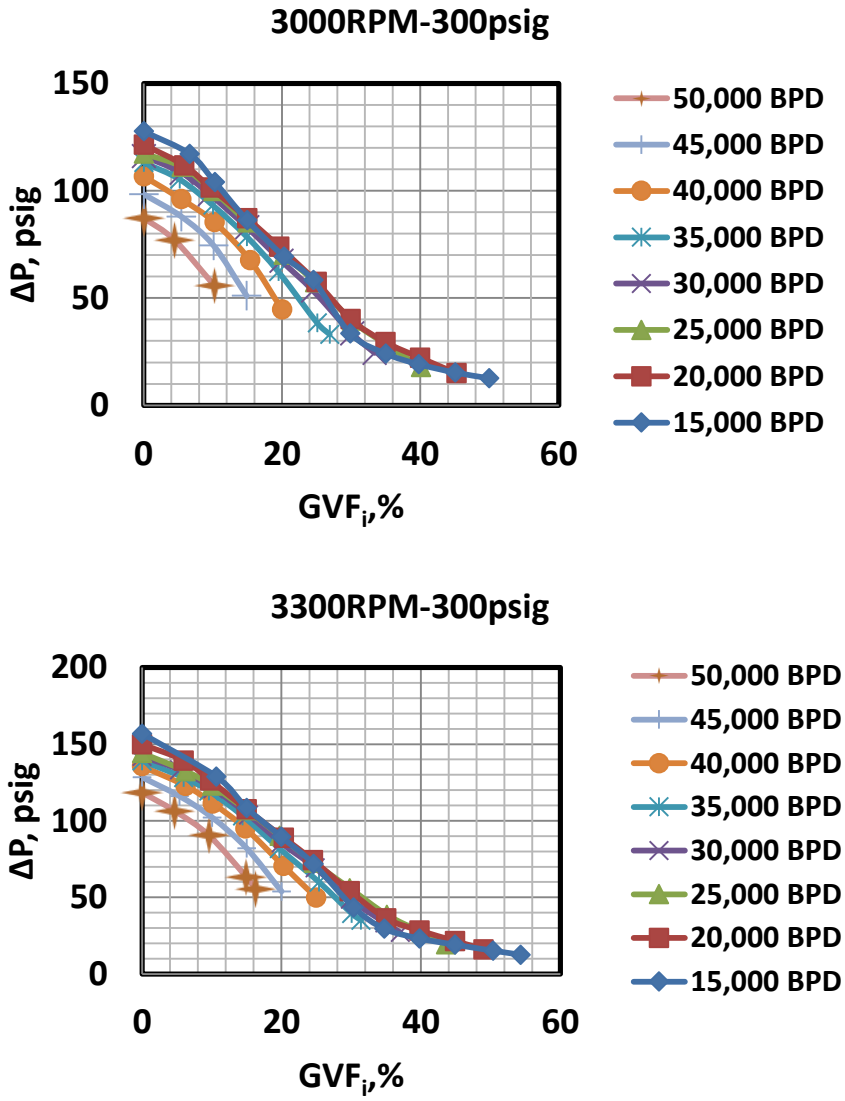

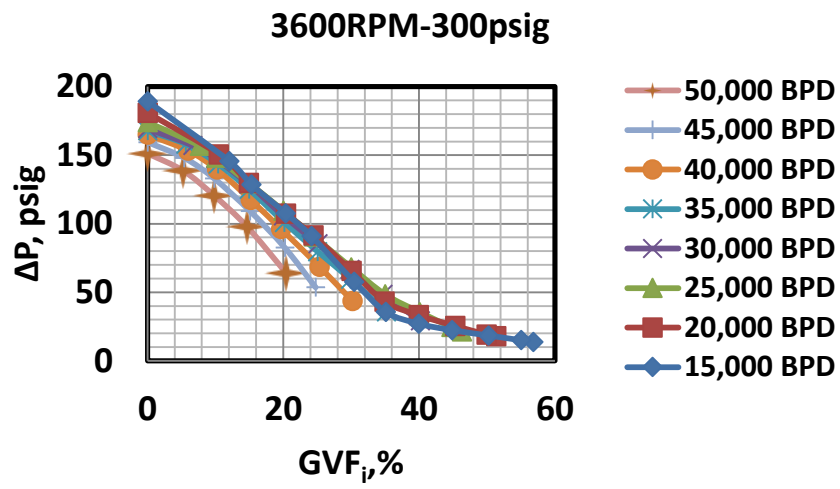
3600RPM-300psig
ΔP, psig
200
150
100
50
0
0
20
40
60
GVF$_i$,%
50,000 BPD
45,000 BPD
40,000 BPD
35,000 BPD
30,000 BPD
25,000 BPD
20,000 BPD
15,000 BPD

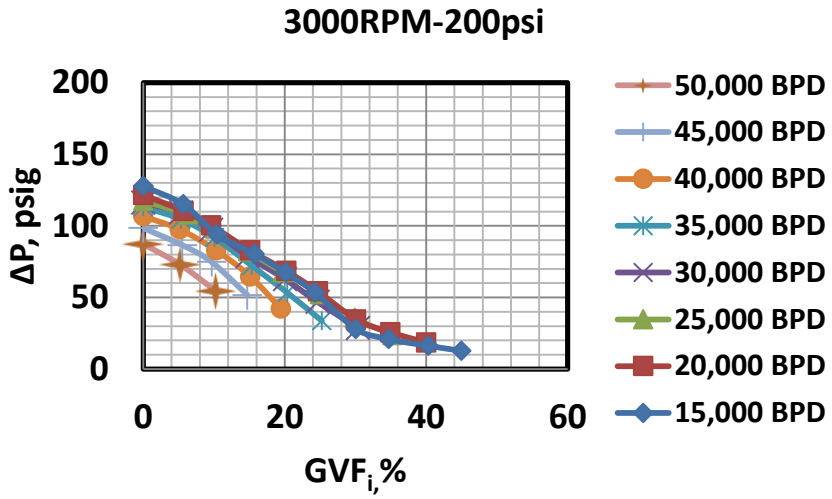
3000RPM-200psi
ΔP, psig
200
150
100
50
0
0
20
40
60
GVF$_i$,%
50,000 BPD
45,000 BPD
40,000 BPD
35,000 BPD
30,000 BPD
25,000 BPD
20,000 BPD
15,000 BPD

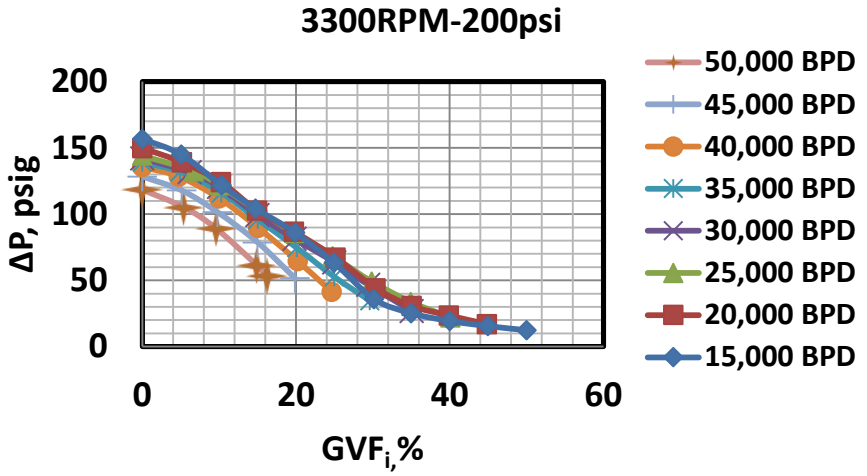
3300RPM-200psi
ΔP, psig
200
150
100
50
0
0
20
40
60
GVF$_i$,%
50,000 BPD
45,000 BPD
40,000 BPD
35,000 BPD
30,000 BPD
25,000 BPD
20,000 BPD
15,000 BPD

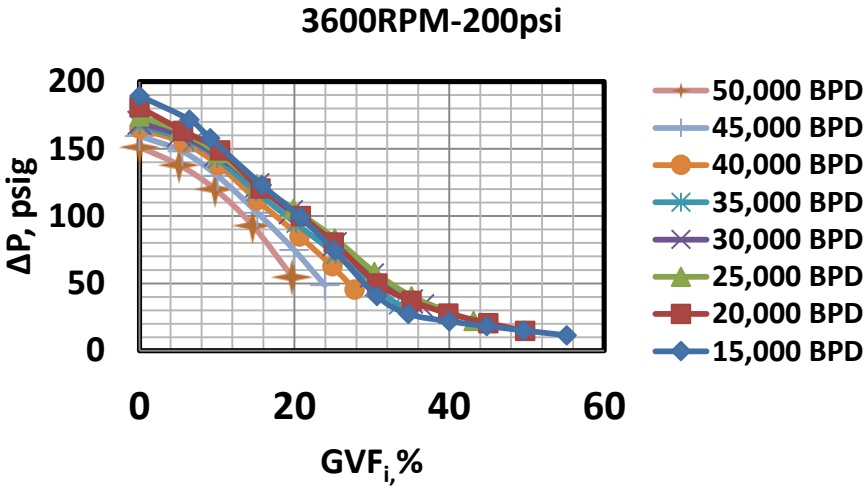
3600RPM-200psi
ΔP, psig
200
150
100
50
0
0
20
40
60
GVF$_i$,%
50,000 BPD
45,000 BPD
40,000 BPD
35,000 BPD
30,000 BPD
25,000 BPD
20,000 BPD
15,000 BPD

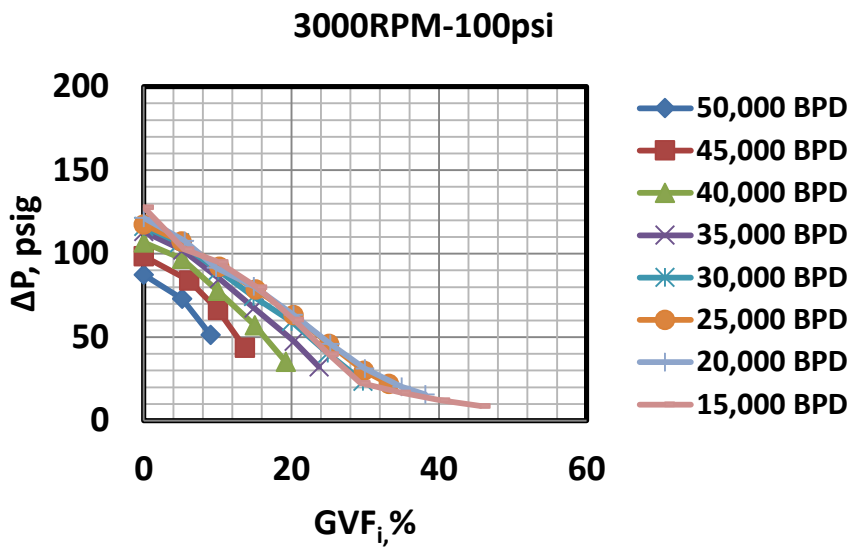
3000RPM-100psi
200
150
100
50
0
ΔP, psig
0
20
40
60
GVF$_i$,%
50,000 BPD
45,000 BPD
40,000 BPD
35,000 BPD
30,000 BPD
25,000 BPD
20,000 BPD
15,000 BPD

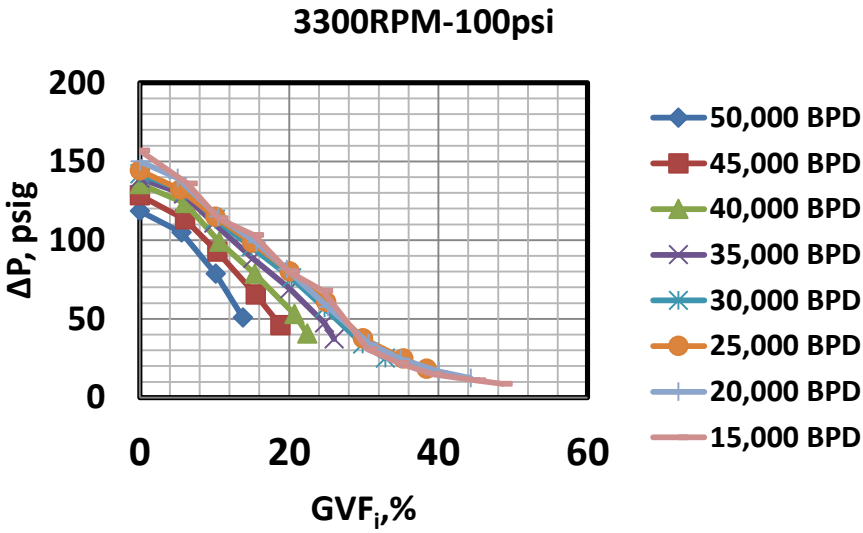
3300RPM-100psi
200
150
100
50
0
ΔP, psig
0
20
40
60
GVF$_i$,%
50,000 BPD
45,000 BPD
40,000 BPD
35,000 BPD
30,000 BPD
25,000 BPD
20,000 BPD
15,000 BPD

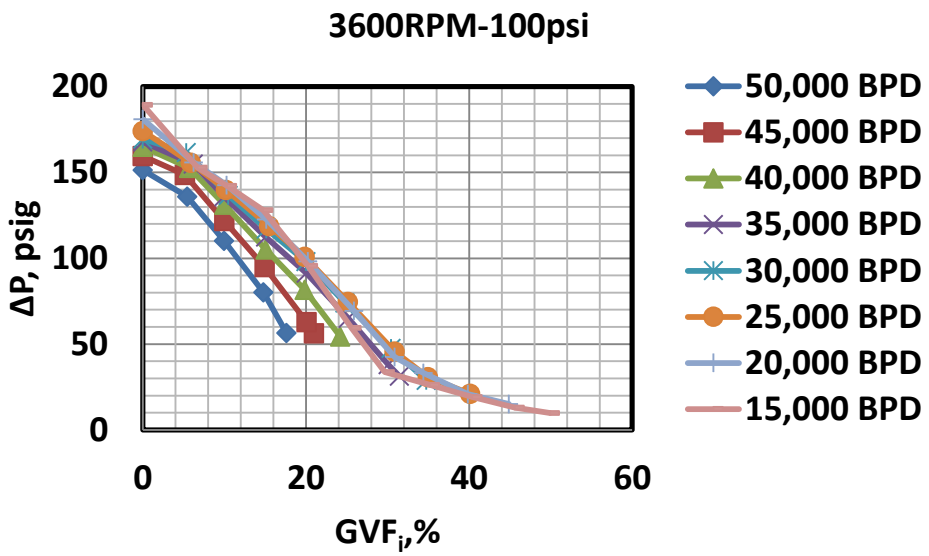
3600RPM-100psi
200
150
100
50
0
ΔP, psig
0
20
40
60
GVF$_i$,%
50,000 BPD
45,000 BPD
40,000 BPD
35,000 BPD
30,000 BPD
25,000 BPD
20,000 BPD
15,000 BPD